Multimaterial Rectifying Device Fibers

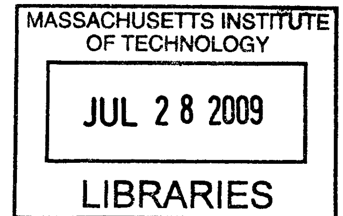
ARCHIVES
MASSACHUSETTS INSTITUTE OF TECHNOLOGY
JUL 28 2009
LIBRARIES

by

Nicholas D. Orf

B.S. Materials Science and Engineering
University of Illinois at Urbana-Champaign, 2003

Submitted to the Department of Materials Science and Engineering
In Partial Fulfillment of the Requirements for the Degree of

Doctor of Philosophy in Materials Science and Engineering
at the
Massachusetts Institute of Technology

June 2009

©2009 Massachusetts Institute of Technology
all rights reserved

Signature of Author .....
Department of Materials Science and Engineering
May 13, 2009

Certified by..
Yoel Fink
Associate Professor of Materials Science
Thesis Supervisor

Accepted by...
Christine Ortiz
Associate Professor of Materials Science
Chair, Departmental Committee on Graduate Students

Multimaterial Rectifying Device Fibers

by

Nicholas D. Orf

Submitted to the Department of Materials Science and Engineering
on May 13, 2009 in Partial Fulfillment of the Requirements for the Degree of
Doctor of Philosophy in Materials Science and Engineering

ABSTRACT

Electronic and optoelectronic device processing is commonly thought to be incompatible with much simpler thermal drawing techniques used in optical fiber production. The incorporation of metals, polymer insulators, and chalcogenide semiconductors into structured fibers has reversed this paradigm and made it possible to realize optoelectronic device functionalities at fiber optic length scales and cost. In spite of the surprising robustness of this processing technique, the electronic performance and complexity of these optoelectronic fiber devices has been constrained by the small set of materials compatible with the fabrication method and the disordered nature of the semiconductor. Specifically, the high density of defects inherent to the amorphous chalcogenide semiconductors precludes the ability to create spatially extended internal electric fields necessary to create more sophisticated devices such as diodes and transistors. In this work, the design, fabrication, and characterization of the first fiber-integrated diode is described. The relevant optical, thermal, and electronic properties of candidate materials compatible with the thermal fiber drawing process are described and measured. Phase changing semiconductors are incorporated into the fiber having both amorphous properties amenable to thermal drawing and crystalline properties ideal for electronic devices. Combinations of metals and semiconductors that form both blocking and non-blocking contacts are identified and combined to form the first diode device that is compatible with the thermal drawing process. Techniques are developed to reduce the dimensions of the resulting devices by an order-of-magnitude compared to all previous multimaterial device fibers. A series of measurements of both compositional and potential spatial variation are used to determine that compound formation at specific metal semiconductor interfaces control the rectifying behavior of the fiber integrated rectifying junction. This work demonstrates the ability to synthesize compounds during fiber drawing to create complex electronic structures and combine them to form basic building blocks of circuits into arbitrary long fiber, paving the way to increasingly complex electronic structures and truly intelligent fibers and fabrics.

Thesis Supervisor: Yoel Fink
Title: Associate Professor of Materials Science

To Diane

Acknowledgments

Many thanks go first to my advisor Professor Yoel Fink. His deep insights and enthusiasm were helpful and greatly encouraging during the many ups and downs of a PhD program. I would also like to thank the members of thesis committee Profs. Marc Baldo and Francesco Stellacci. I found my discussions with both to be interesting and valuable. Prof. Baldo deserves additional thanks for allowing me to use the Omicron UHV surface analysis system and helping with the interpretation of the measurement results from that system. I consider the experiments performed with this system to be among the most important of the entire thesis.

I would also like to thank past and present members of my research group including Dr. Ayman Abouraddy, Dr. Mehmet Bayindir, Noemie Chocat, Dr. Sylvain Danto, Daosheng Deng, Dr. Shunji Egusa, Dr. Ken Kuriki, Dr. Peter Rakich, Zach Ruff, Dr. Ofer Shapira, Dana Shemuly, Dr. Fabien Sorin, Sasha Stolyarov, and Dr. Zheng Wang. All of which have been helpful in the more day-to-day, but equally important, aspects of research. My many conversations with Ayman, Sylvain, Ofer, and Fabien were especially important over the course of this work and truly shaped the scientist I am today. I would like to thank Kaveh Milaninia, Priya Jadhav, and Vanessa Wood for help in figuring out how to run and maintain the many aspects of a very complex UHV system, and all of the members of the Baldo and Bulovic groups for teaching me how to characterize devices. Kaveh Milaninia and Dr. Dan Wesolowski are both good friends and excellent experimentalists, and they were both very helpful throughout the years as classmates and as people who knew how to build anything I wanted. Mark Belanger taught me everything I know about machining, and these new skills have directly resulted in the ability to greatly increase the device density within the fiber and greatly expand the structures that can be built into preforms.

My parents, Dave and Martha, deserve special thanks for their loving support and encouragement from birth. Finally, I want to thank my beautiful wife and best friend, Diane, whose love, patience and support over these last years mean so much to me and whom I love dearly.

Contents

1. Introduction and Background.....11

1.1 Introduction.....11

1.2 Multimaterial Device Fibers.....12

1.3 Multimaterial Device Fiber Fabrication.....14

1.4 Other Methods of Fabricating Device Fibers.....22

1.5 Conclusions.....26

1.6 References.....27

2. Materials Selection and Characterization: Metals.....29

2.1 Introduction.....29

2.2 The Work Function.....31

2.3 Measurement of Work Function.....37

2.4 Work Function Measurements in Low Temperature Alloys.....44

2.4.1 Experimental.....44

2.4.2 Results and Discussion.....45

2.5 Conclusions.....51

2.6 References.....52

3. Materials Selection and Characterization: Insulators and Semiconductors.....57

3.1 Introduction.....57

3.2 Insulators.....58

3.3 Semiconductors.....60

3.3.1 Amorphous Chalcogenide Semiconductors.....60

3.3.2 Crystalline Chalcogenide Semiconductors.....63

3.3.2.1 Thermal Properties of c-Se.....64

3.3.2.2 Electrical Properties of c-Se.....66

3.3.2.3 Band Structure of c-Se.....73

3.4 Conclusions.....74

3.5 References.....75

4. Fabrication of Multimaterial Rectifying Device Fibers....77

4.1 Motivation....77

4.2 Post-Drawing Annealing....78

4.3 Materials Selection and Rectifying Device Fiber Fabrication....81

4.4 Conclusions....88

4.5 References....89

5. Multimaterial Rectifying Device Fiber Characterization....91

5.1 Introduction....91

5.2 Electrical characterization....91

5.2.1 Background....91

5.2.2 Experimental....97

5.2.3 Results and Discussion....98

5.3 Band Diagram construction....107

5.3.1 Background....107

5.3.2 Experimental....112

5.3.3 Results and Discussion....113

5.4 Photodiode characterization....117

5.4.1 Background....117

5.4.2 Experimental....119

5.4.3 Results and Discussion....120

5.5 Conclusions....122

5.6 References....123

6. Suggested Future Work and Conclusions....125

6.1 Introduction....125

6.2 Materials Considerations....125

6.3 Building New Devices and Circuits in Multimaterial Fibers....131

6.4 Conclusions....137

6.5 References....138

Chapter 1: Introduction and Background

1.1 Introduction

When the word 'fiber' comes to mind one may first think of fibers that make up the fabrics and clothes that we wear from day to day. Another may think of long silica optical fibers that pass information across the ends of the earth, making up the fabric of our modern digital lifestyle. Each of these types of fibers have been engineered over time, thousands of years in the case of woven fibers and less than a hundred in the case of optical fibers, to perform their job exceedingly well. But they are only composed of one material and only perform one function. What if multiple materials could be incorporated into a fiber? How would the fiber functionality change? What could be done that has never been done, or even thought of, before? There has recently emerged a class of fibers composed of multiple, entirely different materials— materials with wholly different optical properties, thermal properties, and electrical properties. These new fibers have been shown to transmit,[1] and even reflect,[2] light at wavelengths never before possible with traditional optical fibers. They can function as fiber lasers[3] that emit radiation from the azimuthal direction, unlike any other fiber laser before in which laser emission only comes from the edges in the fiber axis direction. These new fibers can detect light[4,5] and heat[6] and determine from which direction the radiation come from. They can even be woven into fabrics that can function as lenses and large-area detectors, too big to be practical for conventional microprocessor manufacturing techniques. In this thesis I will describe my contribution to this new class of multimaterial fibers, the design, fabrication, and characterization of rectifying junction device fibers. The introduction of non-ohmic junctions into these devices is expected to have profound impact on the functionality and

performance in fiber based devices. And the fabrication techniques I have developed are pushing the size of individual elements within these fiber devices more than an order-of-magnitude below what was previously possible.

The organization of this thesis is as follows. The first chapter will give a general introduction to the challenges of multimaterial fiber device fabrication and the types of fibers that have been previously developed. Additionally, other methods of fiber device fabrication beginning to appear in the scientific literature will be surveyed and compared. The second and third chapters will characterize the relevant materials properties of insulators, semiconductors and metals necessary for the fabrication of new multimaterial rectifying device fibers. The fabrication and characterization of such devices is discussed in chapters 4 and 5, respectively. Suggested future work and final conclusions will be given in chapter 6.

1.2 Multimaterial Device Fibers

Detailed studies of the challenges in materials identification and fiber fabrication are laid out in theses by Dr. Shandon Hart,[7] who first developed the multilayer photonic bandgap fiber, and Dr. Fabien Sorin,[8] who first incorporated metal into the fibers creating metal-semiconductor photodetecting devices. This section will define the challenges of fabricating fibers composed of multiple, very different materials and sets of materials that fit these stringent requirements. Emphasis will be given on fabrication, especially in the chalcogenide glasses.

The difficulty in finding different materials with similar thermal fiber processing characteristics, good adhesion, and very different optical or electrical properties was

thought to be insurmountable. This line of thinking was summed up by Russell and Knight, two leaders in the field of microstructured optical fibers, who said that, "…fibers are limited by the small refractive index contrasts attainable between core and cladding materials (which need to be thermally compatible)".[9] After surveying a wide range of amorphous materials used in optical fibers, Dr. Hart found two families of materials that do all of these things quite well. Inorganic chalcogenide glasses have high refractive indices in the range of 2.2 and 3.5 as well as the ability to modulate the softening temperature from approximately 100° to 500°C through alloying. Amorphous thermoplastic polymers have low indices of refraction and, through a variety of compositions and grades, may have softening temperatures anywhere between less than 0°C to upwards of 250°C. The fiber processing regimes of arsenic triselenide, As_2Se_3, and arsenic trisulfide, As_2S_3, match that of the engineering thermoplastics polyethersulfone, PES, and polyetherimide, PEI, particularly well. Dr. Hart developed novel techniques to fabricate multilayered structured fibers out of these two classes of materials. Further theoretical and experimental work showed that the high surface energy and non-wetting behavior of the materials combination would suggest the multilayer structure is not thermodynamically stable. However, the high viscosity of the materials during drawing can delay the onset of capillary breakup to time periods much longer than the fiber drawing time. Furthermore, using the Ralyeigh-Tomotika model, Dr. Hart was able to create a materials selection map for predicting the ultimate attainable feature size in the multilayer fiber drawing system. More recently, Daosheng Deng further refined Dr. Hart's viscosity model, and, along with this author, was able to experimentally show how the ultimate attainable length scale does vary with viscosity by drawing multilayer

structures of As_2Se_3 and PES and another pair consisting of polyether sulfone (PSU) and glassy selenium, whose viscosity is approximately five orders-of-magnitude smaller than that of As_2Se_3 during fiber drawing.[10] Perhaps the most exciting part of this work is the discovery that the structured layers of the low viscosity material breaks up not into droplets, but extended filaments that may, in principle, extend the entire length of the fiber. The result is the ability to make extremely long nanofilaments or nanowires of chalcogenide glasses like As_2Se_3 or glassy or crystalline Se.

The theoretical work by Deng and Hart would suggest that the low viscosity of liquid metals leads to capillary breakup of layered structures at time scales much shorter than thermal fiber drawing. Drs. Fabien Sorin and Mehmet Bayindir were able to show that large amounts of metal could in fact be incorporated into performs and fibers if the shape of the metallic elements was not that thin films but rather near equilibrium rectangular shapes. By combining the metallic electrodes with the insulating polymer and photoconductive chalcogenide glasses, one-dimension, distributed photodetectors extending the entire length of the fiber may be fabricated.[4] As light impinges on these optoelectronic fibers, electron-hole pairs are excited in the chalcogenide semiconductor, decreasing the series resistance between the metal electrodes. When the electrodes are connected to an external circuit, voltage may be applied to the semiconductor and current through the system is monitored. The change in resistance that occurs when light impinges on the fiber is then easily observed as a change in current.

1.3 Multimaterial Device Fiber Fabrication

The first step in fiber processing is the fabrication of the chalcogenide semiconductor. These are fabricated by the well-known melt quenching method.[11] High

purity elements including germanium, selenium, tellurium, and arsenic, among others, are introduced into quartz ampoule in the appropriate weights inside a glove box. A valve is attached to the open end of the ampoule so that the elements are not exposed to the atmosphere upon removal from the glove box. The ampoule is then attached to a vacuum and evacuated. Although the elements are high purity and stored under inert atmosphere often additional purification steps are necessary. Oxides of selenium and arsenic may be removed by heating under vacuum for 1-2 hours at 250°C. A cold trap is attached to the vacuum line to prevent volatile oxides and contaminates from reaching the pump. Arsenic in particular should be heated until its color changes from a dull grey to a shiny metallic color. Upon purification, the ampoule is sealed with a propane-oxygen torch. The sealed ampoule and elements are then slowly heated to 600-800°C. The heating rate must be slow to allow time for any vapors that form to equilibrate with the solid phase. Ampoules may explode if the vapor pressure reaches too high of a level. Typical heating rates are in the 2-4°C/min. The ampoule is then allowed to homogenize at elevated temperature for at least 12 hours. After this time the rocking mechanism of the custom furnace is switched on so that the entire furnace and ampoule are rotated about a point to further agitate the melt to ensure complete homogenization. Finally the melt is quenched in water and then annealed for 1-2 hours at a temperature slightly below its glass transition to reduce residual stresses from the fast quench. The glass is allowed to slowly cool to room temperature and then may be removed from the ampoule. Using this method, large rods of chalcogenide glass having diameters of 6-12 mm and lengths of more than 160mm may be consistently and easily fabricated. Figure 1.1 shows a picture of the glass fabrication system and two large rods of glass fabricated with this method.

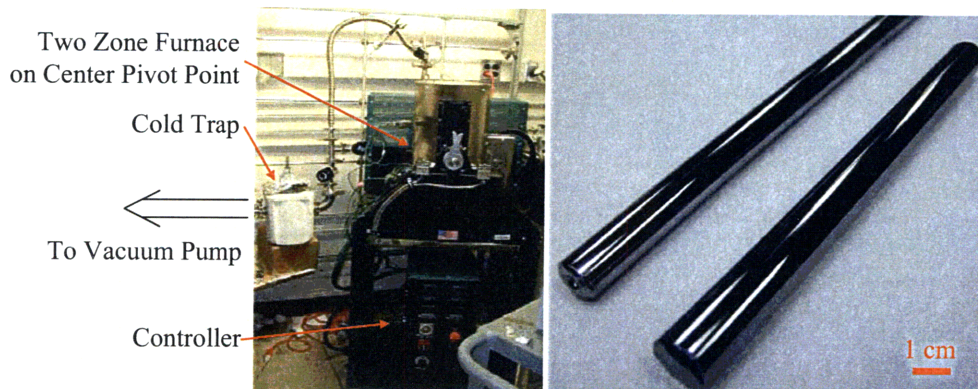

Fig. 1.1. Chalcogenide glass fabrication equipment and bulk rods produced by the melt-quench method.

There are two principle ways of incorporating the chalcogenide glass into perform, typically resulting in two separate classes of fiber called thin-film or multilayer and solid core fibers.[12] The fabrication steps for both methods are summarized in figure 1.2. In one method, thin films of chalcogenide glass are thermally evaporated from bulk pieces unto polymer substrates (a). This polymer/chalcogenide bilayer may be rolled around a mandrel to form an alternating structure of high and low index of refraction (b). Thin films of chalcogenide glasses may also be contacted by metal electrodes using the same method as in part (c) where either a glass rod or thin film of the semiconductor glass is inserted into a polymer tube fabricated to precisely match the outer diameter of the rod. The tube is composed of the same polymer that will be used throughout the preform. Metal electrodes having dimensions of the slots are inserted into the tube so that they touch the semiconductor. In early device fibers, the slots were cut out of the tube free-handed with a Dremel ® tool. This process is time consuming and even though a skilled practitioner could make reasonably rectangular slots, each space is inevitably variable in size. This means that each individual electrode must be custom cut to fit the

slot. Increasingly, the slots are cut out with an endmill. This allows one to use the same drill bit for each cut, resulting in a consistent, standardized electrode size. Metal electrodes having the same size as the slot may be made or commercially procured and are easily fitted into the polymer slots with little additional fitting. Standardizing the electrode and slot saves time and increases repeatability of the fiber draw process substantially. Several additional layers of cleaned, dry polymer are wrapped around the structure (either multilayer or device) in order to provide mechanical support and robustness (d). These layers are termed the 'cladding'. Finally the structure is heated under vacuum at a temperature slightly above the glass transition of the polymer until the roll fuses into a single solid structure. The preform is now complete. It will be thermally drawn (e) into tens to hundreds of meters of fiber. When the process is performed correctly, the initial perform structure (f) is accurately replicated and scaled into the fiber (g).

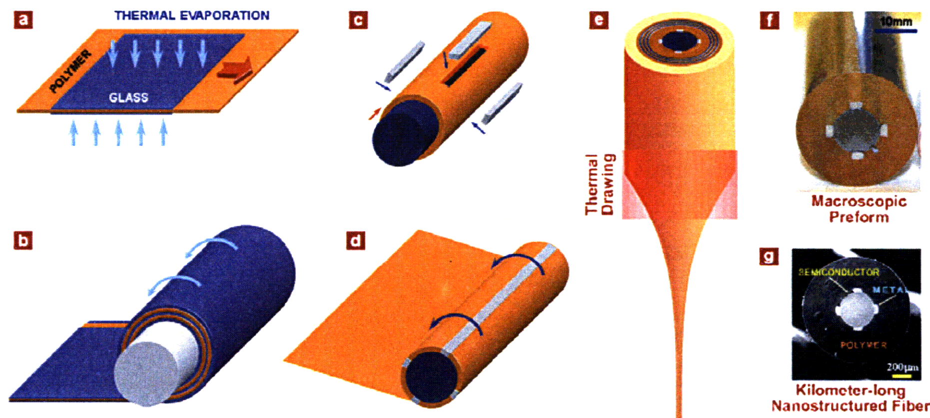

Fig. 1.2. Steps in fiber fabrication described in text (after reference 12).

The preform is drawn into tens to hundreds of meters of fiber in an optical draw tower. The draw tower (shown schematically in 1.3a and pictured in figure 1.3b) consists

principally of a downfeed mechanism that controllably inserts the preform into a three zone furnace that heats it until it is soft and a motorized capstan that pulls the resulting fiber out of the furnace. The furnace upper zone preheats the preform structure to near the polymer glass transition. The middle zone, the warmest of the furnace, is set high enough for the preform to reach a viscosity on the order of 10^5 Poise during the time it is in this zone. At this viscosity the materials will flow very slowly over extended times or more quickly when stress is provided. The capstan at the bottom of the tower provides this stress by controllably pulling the resulting fiber into the bottom zone, set at a low temperature to begin cooling the fiber, and out of the furnace. In steady state, the diameter of the fiber is thus controlled by the rate the preform is fed into the furnace and the rate at which fiber is pulled out. The fiber drawing process is monitored by laser micrometers and a tension meter and controlled by the furnace temperature and capstan drawing speed. The desired outer diameter is set by the experimental goals. In multilayer fibers, the photonic stopband is set by the individual layer size, and thus by the fiber diameter. The outer diameter of device fibers is typically not experimentally critical. Fibers 1 mm in diameter are typically convenient. The best fibers are drawn at as high stress as possible, determined by dividing the tension force by the circumferential area of the fiber. Unfortunately, the ultimate attainable stress before fiber failure is not known. Empirical rules are developed for each type of fiber to give a general rule. Stresses more than 1MPa are typically attainable.

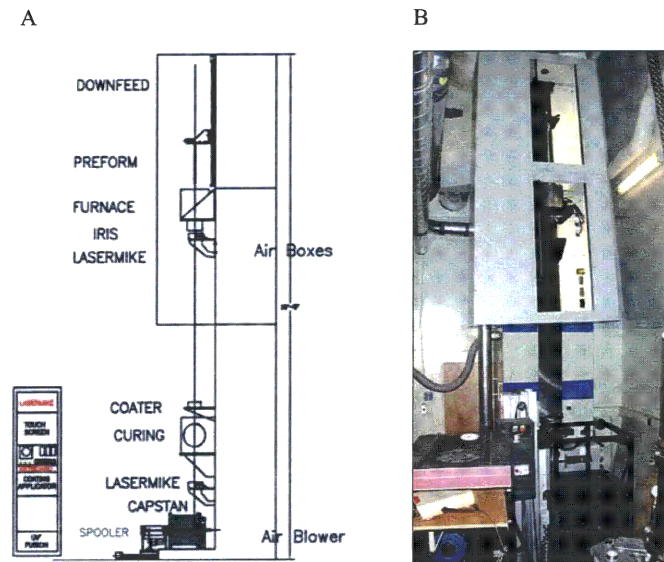

Fig. 1.3 (a) Schematic diagram and (b) photograph of optical draw tower used to fabricate multimaterial device fibers.

The interplay between furnace temperature and draw speed on fiber diameter and stress is shown in figure 1.4 where data from a typical device fiber draw is shown. As the first fiber is drawn from the beginning of the preform, the viscosity and stress is low. The temperature is then sharply dropped until the stress begins to stabilize (meters 1-5). As the draw progresses, the metal electrodes approach the mid zone and begin to absorb heat. The temperature must be increased to maintain the stress (meters 5-12). When the metal reaches the drawing zone, a large increase in diameter is observed, resulting in a sharp drop in stress (meter 13). The stress must be again raised to desired levels by increasing the fiber draw speed and dropping the mid zone temperature. After this transient, steady state is reached and the stress and diameter remain nearly constant for the remainder of the draw (meter 15 to the end). Only slight modifications to draw speed and furnace temperature are needed as more preform leaves the furnace as fiber and less heat is necessary to maintain the draw.

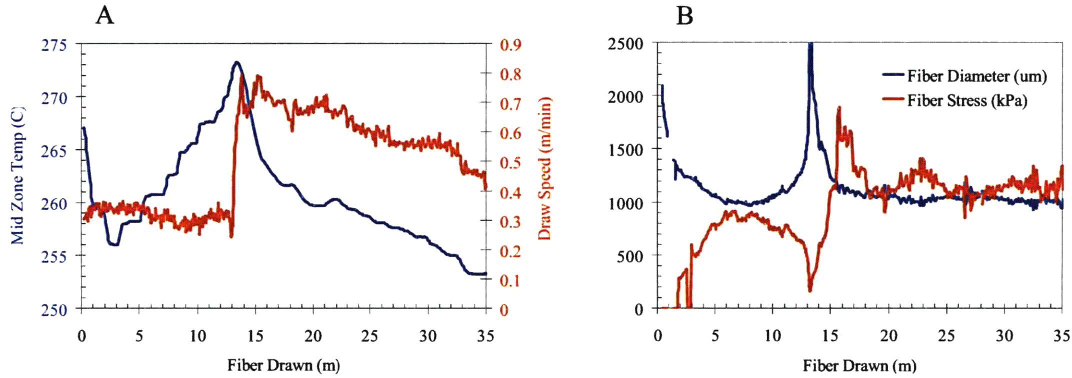

Fig. 1.4. Profile of a typical device fiber draw. (A) Furnace temperature and draw speed are set during fiber drawing to control (B) the fiber diameter and stress.

Using these methods a variety of composite multimaterial fibers have been developed and are summarized in figure 1.5.[12] In (a) and (b), alternating layers of high and low refractive index form a Bragg mirror with a photonic stopband that can be scaled to efficiently reflect light of any wavelength from the mid-IR all the way to the UV regime by simply changing the layer thicknesses. This stopband may line a hollow fiber core to guide and transmit light through the fiber or it may be wrapped around the outside of the fiber to reflect externally incident light. Figs. 1.5 (f) and (g) demonstrate the ability to guide or reflect light of different wavelengths. In particular, the white LED of (f) is separated into a series of colors by fibers that transmit one specific wavelength and allowing the other wavelengths to leak out. The multilayer Bragg mirror may also be combined with a gain medium as in part (c) to create a novel fiber laser.[3] All previous fiber lasers consisted of long fiber sections doped with a gain medium and polished fiber ends that functioned as the mirror. Spontaneous emission from the gain medium is reflected by the mirrors, causing amplified emission and finally laser emission at the fiber ends. In this new fiber laser, the Bragg mirror both guides the pump light along the axial direction and functions as a resonator cavity in the *radial* direction. The end result is that

laser emission comes from the surface of the fiber in the direction perpendicular to the pump light. The laser emission pattern is another unique aspect of the surface emitting fiber laser. When using a gain medium such as organic dyes, the laser emission pattern follows the dipole emission characteristics of the molecule and also behaves dipole-like. Furthermore the spatial orientation of the dipole depends on the polarization of the pump light. Thus the direction of laser emission may be rotated by simply rotation the polarization of the pump. Parts (d) and (e) represent the incorporation of metals into the fibers and there connection to the chalcogenide semiconductor to form photo- or thermal-detecting devices. The semiconductor may be either the form of a thin film (d) or in the form of a bulk rod (e). In either case, the devices can function as individual extended detectors or are incorporated into fabrics and arrays of fibers interfaced with software to determine the exact location of the point of excitation, creating exciting opportunities in large area detection and even lens-less imaging systems.

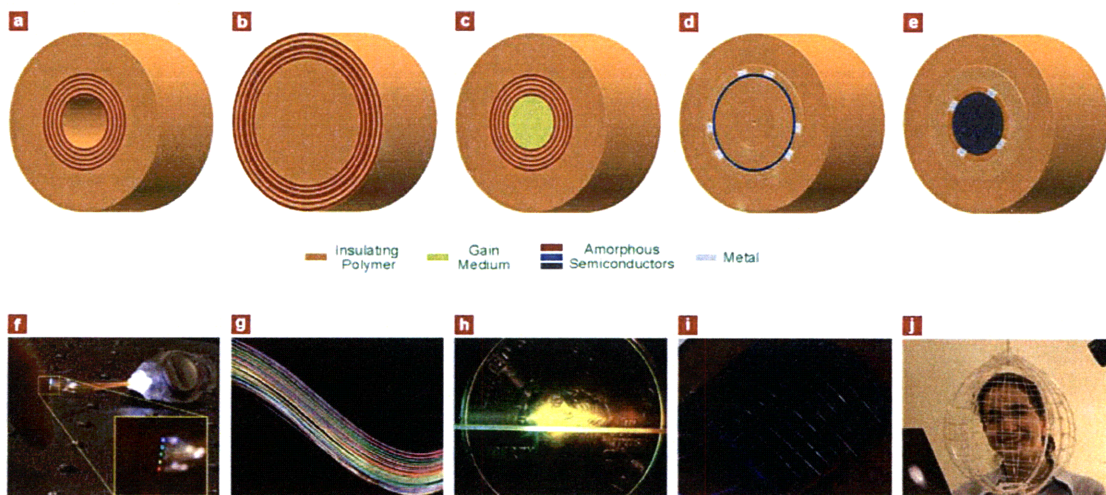

Fig. 1.5. (top row) schematic diagrams of (a) optical transmission fibers, (b) optical reflection fibers, (c) surface emitting fiber laser, (d) thin-film photodetecting fiber, (e) solid core photodetecting fiber. (bottom row) Experimental demonstrations of the above devices.

1.4 Other Methods of Fabricating Device Fibers

Other groups are developing different methods of fabricating device fibers. Some are transferring planar designs onto 3D substrates. Others are taking materials from these planar designs and creating novel device geometries. Often devices are composed of organic semiconductors, but traditional inorganic crystalline semiconductors are being increasingly integrated into high temperature optical fibers for both electronic devices and new optical properties. Rather than build multiple materials and complex geometries into performs and thermally drawing down to fiber, most of these techniques use pre-drawn optical fibers as substrates for post-processing. A major advantage of these techniques is the ability to incorporate common or ideal semiconductor and metal materials into fiber devices that are not necessarily compatible with fiber drawing methods. However, most of these post processing techniques are intrinsically small scale, making them unsuitable for creating extended devices over a few centimeters.

O'Connor et al have transferred standard organic light emitting diode[13] (OLED) and organic photovoltaic[14] (OPV) device designs to three dimensional substrates by thermally evaporating the materials onto rotating silica optical fibers. Devices are divided into 1 mm segments by patterning of the top cathode. Light either originates from or impinges on the semiconductor structure from around the fiber surface, meaning that the cathode layer must be optically thin. The fiber devices perform nearly as well as their planar counterparts and demonstrate unique features of angle-independent performance, as the fiber device may be thought of as a continuum of many small devices, each being normal to the fiber surface at their location. Although this technique utilizes proven device geometries, the transparency requirement of the top electrode should significantly

increase the series resistance of the fiber device. Thus single devices cannot extend over long lengths.

Recently the company Konarka has demonstrated the ability to dip-coat organic semiconductors onto conductive metallic wires and combine them with metal electrodes to form extended lengths of ~3% efficient photovoltaics. The key to achieving this efficiency is the use of conductive counter electrodes so that large surface areas can be used for charge generation and the series resistance of the electrodes do not reduce the over all efficiency.[15]

Liu et al have taken a similar approach.[16,17] Starting with silica fiber substrates, conductive indium tin oxide (ITO) is deposited by a sol-gel process, after which the combination of organic semiconductors poly(3,4-ethylenedioxythiophene)-poly(styrene sulfonate) and poly(3-hexylthiophene/1-(3-methoxycarbonyl)-propyl-1-phenyl-(6,6)C61 (P3HT:PCBM) are dip coated. Finally LiF and aluminum electrodes were thermally evaporated onto the fiber to complete the device. In contrast to the photovoltaic fiber devices fabricated by O'Connor, incident light is coupled into the silica core where some amount leaks into the device 'cladding' layers. This novel design is advantageous because a common problem with photovoltaic devices is the (often) competing desires of having optically long devices to efficiently absorb as much incident radiation as possible and electrically short devices to maximize charge separation and extraction. This device geometry effectively allows one to create thin devices ideal for efficient charge separation and charge extraction while having enough material to maximally absorb the incident photons. Typical devices are a few centimeters long, but there is little reason they may not extend over much larger lengths. The dip coating technique may be easily

modified to roll-to-roll manufacture, and the outer electrodes may be made as thick as necessary to support current flow as it does not interfere with light incident on the structure. These electrodes need not be vacuum deposited, either. There are many methods of solution depositing metal films.

Other groups are beginning to integrate semiconductors and metals inside of microstructured optical fibers (MOFs). This may be achieved by building the material directly into the preform and then thermally drawing the composite down to fiber. Using this method copper microwires have been directly incorporated into MOFs[18] and high quality silica-clad silicon fibers have been produced.[19] Semiconductors and metals may also be incorporated into the air holes of MOFs fibers with post-processing techniques. Silver films have been deposited around the cores of air holes by chemical bath deposition.[20] Plugs of germanium have been inserted into air holes by vacuum sucking the molten semiconductor.[21] Both the perform-based fabrication and post-drawing techniques have thus far only been used to modify the optical properties of the fibers. With the exception of the stack and draw methods used to fabricate the copper and silicon core fibers, it is difficult to envision how multiple different materials may be incorporated into the fibers in any way that enables the formation of extended and uniform interfaces of metals and semiconductors.

One method that may hold promise for incorporating multiple materials and electronic devices has been advanced by Sazio et al., who use high pressure CVD to deposit semiconductors and metals inside the core of previously drawn MOFs.[22] Using this method silicon, germanium, and gold were deposited in precise locations. As a demonstration of the potential utility of this method, a silicon field-effect transistor was

fabricated by depositing metal electrodes on either end of an 11mm segment of fiber. Gate electrodes were deposited on top of the silica fiber, which functioned as the dielectric. A definite field effect was observed, as the current between source and drain depended on the gate voltage. The design is not scalable, however, because increasing the length of the fiber segment increases the distance between source and drain, therefore decreasing device performance. This work has recently been expanded to create long single crystal silicon nanowires[23] and pn junctions by controlling the carrier concentration and type in both silicon and germanium.[24]

There has been some work on fiber-based transistors, in addition to diodes and photodetectors. The two reported methods fashion the transistors out of multiple fibers in a fabric. In one method, oriented metal wires are coated with a dielectric and then the active semiconductor (pentacene).[25] Mask fibers are then aligned 90 degrees to the gate wires, and source and drain contact pads are evaporated in the un-masked spaces. Conducting wires are then woven through the gate wires and contacted to the source and drain pads. In this fashion, large grids of transistors may be fabricated simultaneously, suggesting that complex logic functions may be easily built out of chains of the transistors. The devices perform satisfactorily, with observed semiconductor mobilities on the order of 1 $cm^2V^{-1}s^{-1}$, similar to standard planar pentacene transistors. However, substantial gate leakage currents are observed. Electrochemical transistors have been integrated into conducting fabrics in a similar fashion.[26] Modulation in source drain current occurs by oxidation or reduction of conducting polymer channels in these devices. Standard textile fibers were dipcoated with the conducting polymer PEDOT. Transistors were created by depositing electrolyte solutions at the junction of two crossed

fibers. When a voltage is applied between the two fibers, the PEDOT on one of the coated fibers may be reduced / oxidized to the non-conducting state while the other fiber is oxidized / reduced to a more conductive state. In this way either filament may act as a gate or source and drain depending on the polarity of the applied voltage. Using this technique, fabrics of PEDOT coated fibers have been fabricated and turned into logic arrays capable of performing multiple junctions. The fabrication of transistors out of fiber arrays is an exciting step towards the vision of large area computing, however the ability to create transistors and logic elements out of single fibers remains missing.

1.5 Conclusions

Several techniques used to fabricate fiber-based electronic devices are reviewed. Each method has advantages and disadvantages and may find application in different areas in the future. One chief advantage of the multimaterial fiber drawing technique is the ability to build multiple devices and functionalities into a single structured fiber. The next chapters will review the relevant thermal and electronic properties of materials compatible with the multimaterial fiber drawing technique. Extra emphasis will be given to the properties that will be most important to the formation of a rectifying junction within the fiber. For example, the work function of the metal electrodes will be extensively studied in chapter 2, and the electronic properties of both amorphous and crystalline semiconductors will be discussed in chapter 3. These new materials and properties will be important to the fabrication and characterization of the newly developed rectifying fibers described in later chapters.

1.6 References

[1] Temelkuran, B., Hart, S. D., Benoit, G., Joannopoulos, J. D. & Fink, Y. Wavelength-Scalable Hollow Optical Fibres with Large Photonic Bandgaps for CO_2 Laser Transmission. *Nature* **420**, 650-653, (2002).

[2] Hart, S. D. *et al.* External Reflection from Omnidirectional Dielectric Mirror Fibers. *Science* **296**, 510-513 (2002).

[3] Shapira, O. *et al.* Surface-Emitting Fiber Lasers. *Optics Express* **14**, 3929-3935 (2006).

[4] Bayindir, M. *et al.* Metal-Insulator-Semiconductor Optoelectronic Fibres. *Nature* **431**, 826-829, (2004).

[5] Sorin, F. *et al.* Multimaterial Photodetecting Fibers: a Geometric and Structural Study. *Advanced Materials* **19**, 3872-+ (2007).

[6] Bayindir, M., Abouraddy, A. F., Arnold, J., Joannopoulos, J. D. & Fink, Y. Thermal-Sensing Fiber Devices by Multimaterial Codrawing. *Advanced Materials* **18**, 845 (2006).

[7] Hart, S. D. *Multilayer Composite Photonic Bandgap Fibers* Ph. D. thesis, Massachusetts Institute of Technology, (2004).

[8] Sorin, F. *Multimaterial Multifunctional Fiber Devices* Ph. D. thesis, Massachusetts Institute of Technology, (2007).

[9] Knight, J. C. & Russell, P. S. Applied Optics: New ways to Guide Light. *Science* **296**, 276-277 (2002).

[10] Deng, D. S. *et al.* In-Fiber Semiconductor Filament Arrays. *Nano Letters* **8**, 4265-4269 (2008).

[11] King, W. A., Clare, A. G. & Lacourse, W. C. Laboratory Preparation of Highly Pure As_2Se_3 Glass. *Journal of Non-Crystalline Solids* **181**, 231-237 (1995).

[12] Abouraddy, A. F. *et al.* Towards Multimaterial Multifunctional Fibres that See, Hear, Sense and Communicate. *Nature Materials* **6**, 336-347 (2007).

[13] O'Connor, B., An, K. H., Zhao, Y., Pipe, K. P. & Shtein, M. Fiber Shaped Organic Light Emitting Device. *Advanced Materials* **19**, 3897-3900 (2007).

[14] O'Connor, B., Pipe, K. P. & Shtein, M. Fiber Based Organic Photovoltaic Devices. *Applied Physics Letters* **92**, 193306 (2008).

15 Lee, M. R., Eckert, R. D., Forberich, K., Dennler, G. & Brabec, C. J. ,Gaudiana, R.A. Solar Power Wires Based On Organic Photovoltaic Materials. *Science* (2009).

16 Liu, J. W., Namboothiry, M. A. G. & Carroll, D. L. Fiber-Based Architectures For Organic Photovoltaics. *Applied Physics Letters* **90**, 063501 (2007).

17 Liu, J. W., Namboothiry, M. A. G. & Carroll, D. L. Optical Geometries for Fiber-based Organic Photovoltaics. *Applied Physics Letters* **90**, 133515 (2007).

18 Hou, J. *et al.* Metallic Mode Confinement in Microstructured Fibers. *Optics Express* **16**, 5983-5990 (2008).

19 Ballato, J. *et al.* Silicon Optical Fiber. *Optics Express* **16**, 18675-18683 (2008).

20 Zhang, X., Wang, R., Cox, F. M., Kuhlmey, B. T. & Large, M. C. J. Selective Coating of Holes in Microstructured Optical Fiber and its Application to In-Fiber Absorptive Polarizers. *Optics Express* **15**, 16270-16278 (2007).

21 Tyagi, H. K., Schmidt, M. A., Sempere, L. P. & Russell, P. S. J. Optical Properties of Photonic Crystal Fiber with Integral Micron-Sized Ge Wire. *Optics Express* **16**, 17227-17236 (2008).

22 Sazio, P. J. A. *et al.* Microstructured Optical Fibers as High-Pressure Microfluidic Reactors. *Science* **311**, 1583-1586 (2006).

23 Jackson, B. R., Sazio, P. J. A. & Badding, J. V. Single-Crystal Semiconductor Wires Integrated into Microstructured Optical Fibers. *Advanced Materials* **20**, 1135 (2008).

24 He, R., Krishnamurthy, M., Sazio, P., Gopalan, V. & Badding, J. in *MRS Fall Meeting* (Boston, MA, 2008).

25 Lee, J. B. & Subramanian, V. Weave Patterned Organic Transistors on Fiber for E-Textiles. *IEEE Transactions on Electron Devices* **52**, 269-275 (2005).

26 Hamedi, M., Forchheimer, R. & Inganas, O. Towards Woven Logic from Organic Electronic Fibres. *Nature Materials* **6**, 357-362 (2007).

Chapter 2: Materials Selection and Characterization: Metals

2.1 Introduction

Previous multimaterial device fibers utilized metal electrodes merely as electrical conduits for contacting the semiconductor to the outside world. Hence only the metal's melting temperature was important. As the electronic structure of new fiber devices becomes increasingly complex, it is expected that other electronic properties of the metal, such as the work function, will be increasingly important as well. The work function is an important parameter in electronic device design because, to first order, the potential barrier that forms when two materials are joined is equal to the difference in the materials' work functions. How the work function changes as a function of composition is an interesting question with implications in several areas including catalysis and microelectronics where certain electronic properties are desired but must be balanced with other concerns such as stability and processability. A similar problem exists in the low-temperature processing of multimaterial device fibers.[1]

A range of different metal work functions may be required to fabricate devices with specific properties but the number of materials compatible with the fabrication technique is determined by the processing temperatures of the other fiber component materials. The choice of electrode material is constrained by several factors. First and foremost, the metal must be liquid during the thermal drawing process. This requirement sets an upper limit on the melting temperature of the electrode to be several tens of degrees (typically 30-40°) less than the thermal drawing temperature to ensure the electrode is in fact liquid. Experience has shown that a lower limit on electrode melting temperature exists, as well. If the electrode melts during perform consolidation before

the polymer layers begin to fuse, the metal will flow through gaps and voids in the preform as well as between polymer film layers until the layers fuse, resulting in poor electrode confinement. The temperature of fusion/consolidation and thermal drawing is largely determined by composition of the polymer that makes up most of the preform, which can range from 200°C to upwards of 320°C. Thus the ideal melting temperature of electrode material lies between ~140°C and 300°C, depending on the choice of polymer. If the electrode materials were limited to only elemental metals the possible choices would be indium (T_m = 157°C), tin (T_m = 232°C), and bismuth (T_m = 271°C), but metal alloys may also be used. Many metal alloys are available with melting temperatures within this range. Depending on the exact composition, alloys have solidus and liquidus transitions but may also have single melting temperatures (eutectic alloys). Alloys with incongruent melting transitions (those with liquidus and solidus temperatures) have been found to be inferior to metal alloys with a single melting transition, i.e. pure metals or eutectic compositions, in terms of thermal drawing. This is thought to be the case because for temperatures between the liquidus and solidus, these off-eutectic alloys consist of both liquid and solid phases. The solid phases do not flow well and cause bottlenecks in the neck down region of the preform during thermal processing. This problem can be avoided in principle by selecting off-eutectic compositions with liquidus temperatures sufficiently below the thermal drawing temperature that they are in fact completely liquid during fiber drawing. The use of off-eutectic alloys has not been thoroughly explored to date as there has not been a need to select metal electrode composition based on anything other than melting temperature. Given these processing parameters, several metals and eutectic alloys have melting temperatures within the

correct processing regime and may be of interest for electronic devices. These alloys include $Sn_{57}Bi_{43}$ (T_m = 138°C), In (T_m = 157°C), $Sn_{74}Pb_{26}$ (T_m = 183°C), $Sn_{85}Zn_{15}$ (T_m = 199°C), $Sn_{6.2}Au_{93.8}$ (T_m = 217°C), $Sn_{96}Ag_4$ (T_m = 221°C), Sn (T_m = 232°C), $Sn_{63.6}Ag_{26.9}Sb_{9.5}$ (T_m = 233°C), $Cd_{73.4}Zn_{26.6}$ (T_m = 266°C), Bi (T_m = 271°C), $Sn_{29.4}Au_{70.6}$ (T_m = 280°C).

2.2 The Work Function

The work function of a material is defined as the minimum energy necessary to remove an electron from the material to a location independent of position in vacuum. There is no general model for relating a material's work function to other intrinsic properties, although many researchers have tried to find such a correlation. Perhaps the simpliest relationship was found by Gordy and Thomas who saw that an element's work function is roughly linearly related to its electronegativity, X. The relationship between X and work function can be seen in figure 2.1 and can be described by the equation[2]

$$\phi = 2.227X + 0.34eV . \quad (2.1)$$

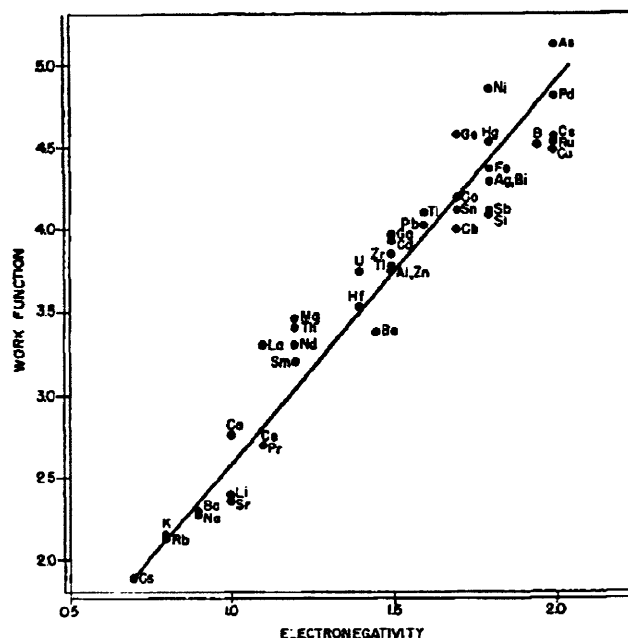

Fig. 2.1. Work function of the elements plotted with their electronegativity (after Ref. 2)

Simple metals such as the alkalis fit this trend well, but transition elements with their more localized d-electrons may deviate noticeably from the trend. Others have tried to extend the relationship between work function and electronegativity to compounds, typically using some sort of mixing rule with additional terms to account for deviations, with various degrees of success.

Yamamoto and coworkers compared the work function of several binary compounds (primarily consisting of transition metal borides, oxides, carbides, and nitrides) with the electronegativity of their constituent elements.[3] No relation was found between the arithmetic and geometric averages of the component element electronegativity and work function. The authors found the strongest correlation between the compound work function and the X of the least electronegative constituent and proposed the relationship

$$\phi_{AB} = \phi_A + \frac{1.41}{d_A}\left(\frac{2\phi_A - \phi_B - 0.34}{\phi_A + \phi_B - 0.68}\right), \quad (2.2)$$

where the second term is essentially a minor correction based on a simple mixing rule (d_A is the covalent bond length). A qualitative fit does exist between the work function predicted by equation 2.2 and experiment .[3]

Nethercot found a strong relationship between the work function of simple octet binary compounds and the geometric mean of the constituent electronegativities.[4] He proposed the relation in terms of the threshold energy for photoemission (the valence band maximum in semiconductors and insulators) with an additional term of one-half the band gap accounting for the Fermi energy being in the middle of the band gap in an intrinsic material.

$$E_T = 2.86(X_A X_B)^{1/2} + E_g/2 \quad (2.3)$$

The relationship fits with experiment surprisingly well. This may be due to the fact that the bonding in compounds studied by Nethercot (III-V, II-IV, and I-VII compounds) are governed by the s- and p-shells while the effects of d-shell electrons must be considered in transition metal compounds studied by Yamamoto.

Gelatt and Ehrenreich studied the relationship between composition and work function in disordered substitutional transition metal alloys theoretically.[5] This problem is more complicated than the one considered by Nethercot because the effect of d-shell electrons must included in any calculation in addition to the valence band (s- and p-shells) electrons, and the charge transfer between the d-shell and valence band electrons of the constituent elements must be considered separately. When the charge transfer is small, the alloy should be disordered. They predicted that the alloy work function was

governed by a simple mixing rule plus an additional term that includes the densities of states at the Fermi level (ρ) and arrived at the equation:

$$\phi_{AB} = x\phi_A + (1-x)\phi_B + x(1-x)\left(\frac{(\phi_A-\phi_B)(\rho_A-\rho_B)}{x\rho_A+(1-x)\rho_B}\right) \quad (2.4)$$

For the Ag-Au system the above equation suggests the work function of the alloy will be slightly depressed from the simple mixing value (e.g. the work function of the 50:50 alloy is less than the average of the two work functions). Fain and McDavid measured the work function of several AgAu alloys and found that work function depression occurred, the magnitude of which was much larger than predicted by Gelatt and Ehrenrich.[6]

Malov and coworkers have studied the change in work function with temperature and composition for a wide range of alloys in addition to attempting to correlate work function with phase behavior including In-Bi, In-Pb,[7] Bi-Cd, Bi-Sb, Sn-Pb, [8] Cu-Sb, Cu-In, Cu-Cd,[9] Cd-Zn-Sb,[10] Sb alloys containing Sn, In, Zn,[11] and sodium alloys.[12] They also found that the alloy work function was typically less than the value a simple mixing rule would suggest.

Thus several workers have shown that the work function of an alloy is heavily weighted by the smallest work function element instead of an average of the two constituent elements. Gelatt and Ehrenrich were careful to point out that their theoretical framework applied only for disordered transition metal alloys where the charge transfer between elements was small. As the charge transfer increases ordering and compound formation should be expected. One may then reasonably consider whether electrons more tightly held by ordered compounds will be more difficult to remove from the material, thus resulting in an increased work function. Li and coworkers measured the work function of several intermetallic compounds in the Ni-Al, Ni-Fe, and Ni-Ti systems

while considering their brittleness.[13] Surprisingly, the work functions of these intermetallics were found to be much closer to that of the large work function element, and in some cases, larger than either of the constituents. The authors suggest that work function measurements may provide insight into engineering the brittleness of alloys for high temperature applications.

The ability to modulate work function while maintaining or enhancing other properties is of great practical interest in several fields. Field emitters with specific voltage thresholds and emission currents are important in vacuum microelectronics. Organic light-emitting diode (OLED) performance has been found to be strongly dependent on the work function of the cathode, but low work function materials are often oxidize rapidly in air, degrading device performance. The next generations of silicon microelectronics may require polysilicon gates be replaced with metals, so there is a distinct need for metals with specific work functions and processing characteristics.

Low threshold voltage and high electron emission current are ideal characteristics of field emitters in vacuum microelectronics. As electron emission is a surface phenomenon, thin coatings on emitter materials may have a dramatic influence on the emission properties. For example, Alkalis metals have low work functions and are known to increase electron current density while lowering threshold field for emission.[14] Coverage of slightly less than a monolayer of electropositive material achieves the benefit of reduced work function at the surface as well as creating a dipole between the substrate and coating that further assists electron escape.[15] The copper-lithium alloy system has been investigated for this purpose as well as cesium coatings on tungsten tips.[15] Electron emission from tungsten cathodes can be improved by coating with noble

metals such as osmium, iridium, and rhenium. Thomas and Gibson measured the composition dependence on work function in Ir-W and Re-W alloys.[16] The effect of Hf and Ti coatings on tungsten emitters were investigated by Szczudlo and coworkers.[17]

Low work function metals are also of interest to OLED performance as barriers to electron injection into devices can limit performance. Magnesium-silver alloys are commonly used as OLED cathodes. Low work function metals like magnesium are unstable in air, thus limiting their usefulness. Upwards of ~10% of silver ($\Phi = 4.6$ eV) may be alloyed with magnesium without significantly changing its work function ($\Phi = 3.5$ eV) while improving the air stability.[18]

Miniaturization in the microelectronics industry is also prompting research in the compositional dependence of alloy work functions. Several problems are developing as oxide layers in MOSFETs decrease, including boron dopant penetration and poly-silicon gate depletion. The use of metals as gate materials can fix these problems. The work function of the gate should be in a narrow range for optimal device performance ($\Phi = 4$-4.2 eV and 5-5.2 eV for NMOSFETs and PMOSFETs, respectively), and thus metal alloys that must be designed to must be designed to have specific work functions in these regimes and also able withstand silicon device processing temperatures.[19] The compositional dependence of work function in the Ta-Pt, Ta-Ti,[19] Ni-Ti,[20] Al-Ni, Ni-Ta,[21] Mo-Ta,[22] Ru-Ta,[23] Pt-Ru[24] alloy systems have been investigated for this purpose. In each of these cases the composite work function was weighted towards the low work function element.

The work function of alloys is also of interest in the field of catalysis where changing the composition of the catalyst surface may modulate the catalytic activity and

surface work function.[25] To this end, Sachtler and co-workers studied the work function of several alloy systems including Cu-Ni, [26,27] Au-Pt,[28] Pt-Ru,[29] and Ag-Pd.[30] The authors also developed a technique they coined 'surface titration' to study the surface composition of alloy films. In this technique one of the two elements of a binary system readily reacts a gas such as carbon monoxide, while the other does not. The change in the work function measurement with the addition of the gas can therefore be related to the composition of the reacting (or adsorbing) element at the surface. Furthermore, the change in signal over time can be related to the diffusion of elements to and from the surface.[29,30]

2.3 Measurement of Work Function

There are several methods of measuring work function. Two of the most common methods are the Kelvin Probe method and photoemission spectroscopy. Although both techniques can be used to measure the work function of a material, fundamental differences in the methods should be kept in mind when interpreting measurement data. This point is especially pertinent when the material surface in question has multiple regions with different work functions (termed "patches"), as is the case in any polycrystalline material.[31] Alloy compositions having more than one phase present introduce even more work function patches.

The Kelvin probe method is named after Lord Kelvin who first discovered that a potential develops when two (conducting) materials are brought very close to each other and then into contact. As two materials come close together, electrons from the lower work function material will tend to flow through an external circuit connecting the

materials to the higher work function material. Equal and opposite surface charges develop on the materials resulting in what is essentially a capacitor. This potential difference between the two plates is equal to the difference in work function of the materials and is called the contact potential. Thus if the work function of one of the materials is known, the other may be calculated. In practice, a probe head (typically made of gold or stainless steel) with a well known work function and size is connected electrically to an unknown sample and sinusoidally vibrated close to its surface creating a variable capacitance, or equivalently, an alternating current. This current may be measured as a voltage drop across a resistor or other circuit element. An additional backing voltage is applied and tuned until the current in the circuit (or voltage across the circuit element) disappears. At this point, the applied voltage exactly cancels the contact potential difference between the sample and probe. Thus, the work function of the sample may be calculated if the probe head work function is known.[32] Mathematically, the capacitance between the probe head and the sample is

$$C = \frac{Q}{V} = \frac{\varepsilon A}{h}, \quad (2.5)$$

where ε is the dielectric constant of the dielectric between the sample and probe, h is the distance between the probe and sample, and A is the area of the probe head. The probe/sample spacing may be varied sinusoidally with time

$$h = h_0 + h_1 \sin(\omega t), \quad (2.6)$$

where h_0 is the average sample/probe spacing and h_1 is the probe oscillator amplitude. The time averaged change in surface charge on the sample/probe capacitor may be written as

$$I_{circuit} = \frac{dQ}{dt} = -(V_{contact} + V_{backing})\frac{\varepsilon A}{h^2}\frac{dh}{dt} = -(V_{contact} + V_{backing})\frac{\varepsilon A}{h_0^{\ 2}}h_1\omega\cos(\omega t) \quad (2.7)$$

and it is seen that the current through the circuit vanishes when $V_{backing} = V_{contact}$. With proper circuit design the contact potential difference may be determined very precisely. The accuracy of the measured sample work function therefore depends on how well known the probe work function is. For this reason polycrystalline gold, with a nominal work function of 5.1 eV and which is relatively inert under normal conditions, is used as the probe head. Even though the gold may not oxidize, even non-reactive gases may adsorb onto gold surfaces and alter the apparent work function by as much as 0.4 eV.[33] Because the capacitance between the sample and probe is proportional to the probe head's area, the measured work function is an area weighted average of the work function patches underneath the probe. Figure 2.2 depicts the situation schematically.

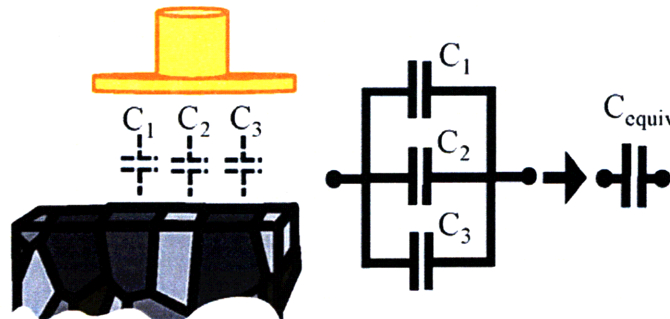

Fig. 2.2. Schematic diagram of Kelvin probe measurement. Each patch (different colored grains) has its own work function and contact potential difference with the gold probe head. The measured contact potential difference is the area weighted average of individual CPDs.

Photoemission spectroscopy is based on the photoelectric effect first discovered in 1887 by Heinrich Hertz. Einstein won the 1921 Nobel Prize for his 1905 explanation of the phenomenon with quantized energy states.[31] The photoelectric effect describes the process of electron emission from a material when photons of sufficient energy are

incident on the sample. When photons impinge on the material, electrons are excited to higher energy states from their ground level (this is the same principle that causes carrier excitation from the valence to conduction band in semiconductors used in photoconductors or solar cells). If the photon energy is larger than the energy needed to completely remove the electron from the material, electrons will be ejected from the sample. This minimum energy is the work function.

The simplest photoemission spectrometer consists of three components: the photon source, sample, and energy analyzer. The ideal photon source has high intensity and a narrow linewidth. The helium I line has a photon energy of 21.2 eV and is the most common photon source used in ultraviolet photoemission spectroscopy (UPS). X-ray photoelectron spectroscopy (XPS) typically uses 1486.6 eV photons from an Al k-α source. The incident photons strike the sample and excite electrons to elevated states. As these electrons travel through the sample they may lose energy through collisions with other electrons or scatterers. If excited electrons with enough kinetic energy reach the surface of the material they may be ejected from the sample. The process of photoemission and detection by the energy analyzer is summarized in figure 2.3. The energy of the ejected electrons is equal to the incident energy (photon energy) minus the binding energy and work function

$$E'_{kinetic} = h\upsilon - B.E. - \phi_{sample}. \quad (2.8)$$

Electrons are ejected from the sample with different energies and enter into the analyzer where they are retarded by an amount, R, determined by the lens voltages. They then pass through a band-pass filter that only allows electrons of a given energy through before striking a photomultiplier and photodetector. The total kinetic energy of the electrons

collected by the energy analyzer is thus the sum of the retarding energy, pass energy, and detector work function,

$$E_{kinetic} = R+P+\Phi_{detector} \,. \quad (2.9)$$

The retarding and pass energies are set but the exact work function of the detector is unknown and must be determined through calibration. Electrons ejected from the Fermi level of the system have zero binding energy so their final kinetic energy is simply equal to the incident photon energy. Thus at high energies the point where photon intensity goes to zero (the high-energy cut-off) occurs at a kinetic energy of hv (as seen by the electron) or a binding energy of zero (as seen by the sample). This can be seen in region 1 of figure 2.3. Calibration is done in software by setting the detector work function such that the high energy cut-off occurs at exactly hv. Thus the intensity of photoelectrons reaching the photodetector for different retarding voltages can be constructed and related to the number of electrons in the sample with a particular binding energy and is called the energy distribution curve (EDC), which is closely related to the sample joint density-of-states. A material's valence band density-of-states can be mapped with this method because discrete energy states associated with atomic binding energies will appear as peaks in the EDC (region 2 in figure 2.3). The sample work function can be seen from the low-energy cut-off of the EDC. At this point, excitation by the incident energy, hv, does not impart enough additional energy for deeply bound electrons to overcome the binding energy and work function barriers necessary for electron emission. Thus the intensity of electron emission goes to zero (region 3 in figure 2.3). This may be seen mathematically by noting that, relative to the Fermi level of the system, the total kinetic energy of

electrons striking the detector (as seen by the detector) is equal to the incident energy minus the binding energy of the emitted electron,

$$E_k = h\nu - B.E.. \quad (2.10)$$

Equations 2.8 and 2.9 may be combined to see that

$$E_k' = E_k - \phi_{sample}. \quad (2.11)$$

Thus at the low energy cut-off when the kinetic energy of electrons leaving the sample, E_k', goes to zero, the measured kinetic energy at the detector, E_k, equals the sample work function, Φ_{sample}.

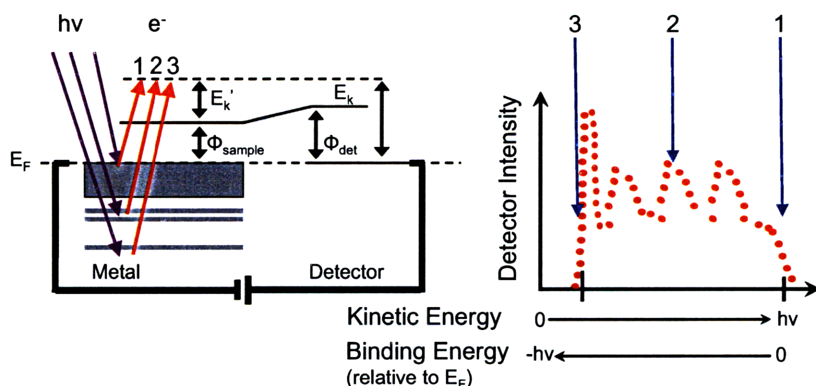

Fig. 2.3. Description of the photoemission spectroscopy process. Electrons residing at the sample Fermi level (region 1) have zero binding energy and the maximal kinetic energy seen by the detector. Electrons emanating from discrete energy states within the can be seen as peaks in the EDC (region 2). Emitted electrons must have energy greater than the sample work function, thus the low energy cut-off is equal to the minimum energy necessary to escape the sample, the work function (region 3).

The work function measured by UPS is heavily weighted by the lowest work function patch. This is most easily seen graphically in figure 2.4. In a photoemission study, the probe beam has a large area and floods the surface. Each patch emits its own EDC. The observed energy of the Fermi level and bound states (regions 1 and 2 in figure

2.3) do not change because they are fixed by the incident photon energy and atomic binding, respectively. The secondary electron cut-off (region 3), i.e. the work function, is variable and depends on the surface. The low energy emission spectra from each patch will be different and the observed UPS spectrum is a convolution of these. However, as the signal from the lowest work function patch will overwhelm that of the other patches, only the onset of this low work function patch is visible. Thus the work function observed in UPS measurements is heavily weighted by the lowest work function region of the sample.

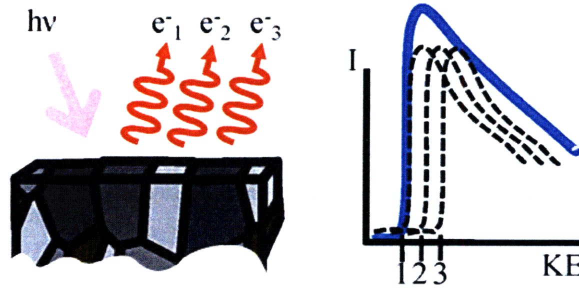

Fig. 2.4. Schematic diagram of secondary photoelectron emission from polycrystalline material. Each work function patch emits its own spectrum of secondary electrons at low kinetic energy. The observed onset of secondary emission is dominated by the lowest work function patch, which overwhelms the signal from other patches.

The photoemission process for semiconductors is similar to the one described for metals with the only difference being that there are few electron states in the semiconductor bandgap where the work function resides. While the high energy cut-off must still occur at an energy equal to the incident photon energy, the actual high-energy cut-off of substantial emission occurs only at the top of the valence band. Hence the distance between the valence band and Fermi level in a semiconductor is equal to the binding energy at which electron emission starts in the EDC, and the location of both E_F and E_v relative to the vacuum can be determined for semiconductors.

Photoemission studies are done in ultra high vacuum for two reasons. First, the measurement is extremely surface sensitive. Because electron energies typically range from a few eV (UPS) to ~1500 eV (XPS), the escape depth of electrons is on the order of 4 to 40 angstroms.[31] Even incomplete monolayers of contaminates or adsorbates can significantly change the EDC. Thus the vacuum level must be kept on the order of 10^{-9} Torr to prevent contaminates or residual gases from sticking to the sample surface. Samples are typically also sputter cleaned with Ar+ and/or heated to clean the surface before the measurement. A second reason the vacuum level must be kept so high is to increase the electron mean free path. Collisions between the ejected electrons and gases must be minimized so that enough electrons reach the detector to be counted.

2.4 Work Function Measurements of Low Temperature Alloys

2.4.1 Experimental

The work function of seven alloys was measured by the scanning Kelvin probe technique and ultraviolet photoemission spectroscopy.[34] For contact potential measurements, samples were cleaned before loading into inert atmosphere where additional fresh, oxide-free surface was exposed. The measurements were performed with a KP Technology SKP5050 Scanning Kelvin Probe equipped with a 2-mm diameter polycrystalline gold-coated probe head (nominal work function taken to be 5.1 eV)[35] in inert (nitrogen) atmosphere to limit oxidation or gas adsorption that may cause changes in either the sample or probe head work function. The sample to tip spacing was held constant (within 1 micron) both during each scan and between samples to minimize stray capacitance errors.[32] Approximately 400 measurements were made over a scanned area

of between 6 and 13 mm in each dimension. Measurement uncertainty was taken to be the standard deviation in work function over the entire scanned area.

The same samples used in SKP were used in the UPS measurements, performed with an Omicron Multiprobe system. Samples were sputter-cleaned with an in-situ argon ion gun immediately prior to measurement. The photon source was a He I (21.2 eV) plasma. Samples were reverse biased to sharpen the onset of secondary electron emission as well as eliminate tertiary electrons from the spectrometer. The UV spot size was approximately $1cm^2$. Measurement uncertainty was taken to be the half width of the high kinetic energy Fermi-edge cut-off (i.e. zero binding energy). The surface composition as a function of argon ion sputtering time was measured in a separate Kratos Axis Ultra XPS system, while the bulk composition was confirmed by measuring the melting temperature of portions of the alloy with DSC.

2.4.2 Results and Discussion

Alloy work functions measured by the two methods are summarized in table 2.2. Representative line scans of the SKP measured work function are shown in figure 2.5. The photoemission onset measured by UPS is given in figure 2.6. Two observations may be made immediately. First, the same trend in work function exists with both techniques. Four alloys, Sn, $Sn_{96}Ag_4$, $Sn_{57}Bi_{43}$, and $Sn_{74}Pb_{26}$, have nearly the same work function, within experimental error. $Sn_{85}Zn_{15}$ has a notably lower work function than the other alloys, and the gold-tin alloys have the largest work functions of all. Secondly, there is a systematic offset of about 0.3 eV between the UPS and Kelvin Probe methods. XPS revealed no contamination other than a superficial layer of carbon and oxygen, expected from atmospheric exposure during sample transfer and which disappeared with ion

sputtering. Even though differences in sputtering yield between phases could introduce large variations in composition,[36] the surface composition after sputtering was found to be close to the bulk levels in most cases. The most notable departure from this trend is the $Sn_{42}Bi_{58}$ alloy, which was found to be significantly bismuth deficient. The alloys with the greatest discrepancies between bulk and measured surface composition generally correspond to those with the greatest difference in sputtering efficiency.[36] DSC scans show a single sharp melting temperature for each alloy (figure 2.7) near the nominal bulk value. This confirms that the bulk composition is eutectic because any off-eutectic composition will undergo an extended melting transition between solidus and liquidus temperatures. The measured melting transition occurs at temperatures close to and slightly above their nominal value. This is expected as it is well documented that temperature transitions measured by DSC are dependent on the heating rate.

Table 2.2. Work functions of tin alloys measured with SKP and UPS along with melting temperature. Estimated error is given in parentheses.

Bulk Composition (wt%)	Measured Composition (wt%)	Φ(SKP) (eV)	Φ (UPS) (eV)	$T_{melting}$ (°C)
$Sn_{91}Zn_9$	$Sn_{93.5}Zn_{6.5}$	4.17 (0.003)	3.92 (0.20)	199
$Sn_{42}Bi_{58}$	$Sn_{70}Bi_{30}$	4.44 (0.02)	4.16 (0.35)	138
Sn_{100}	Sn_{100}	4.47 (0.008)	4.14 (0.19)	232
$Sn_{96.5}Ag_{3.5}$	$Sn_{97.2}Ag_{2.8}$	4.46 (0.006)	4.13 (0.19)	221
$Sn_{63}Pb_{37}$	$Sn_{73}Pb_{27}$	4.52 (0.020)	4.16 (0.23)	180
$Sn_{90}Au_{10}$	$Sn_{88.3}Au_{11.7}$	4.58 (0.016)	4.28 (0.20)	217
$Sn_{20}Au_{80}$	$Sn_{11.7}Au_{88.3}$	4.84 (0.014)	4.59 (0.19)	280

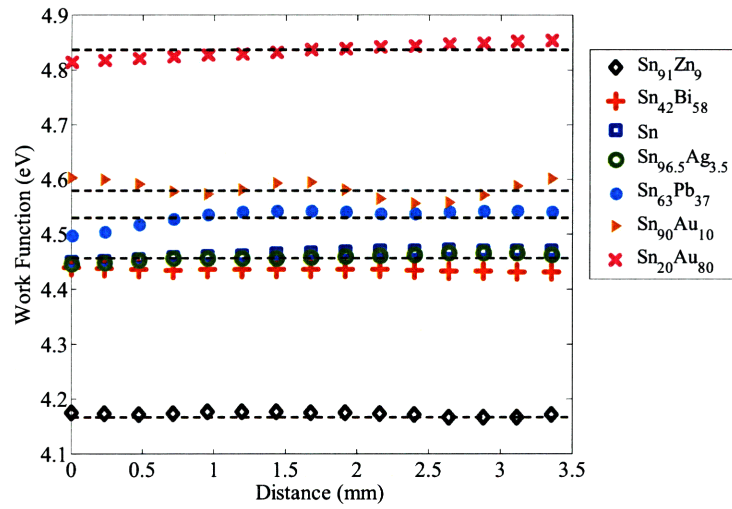

Fig. 2.5. SKP line scans of work function for seven tin alloys.

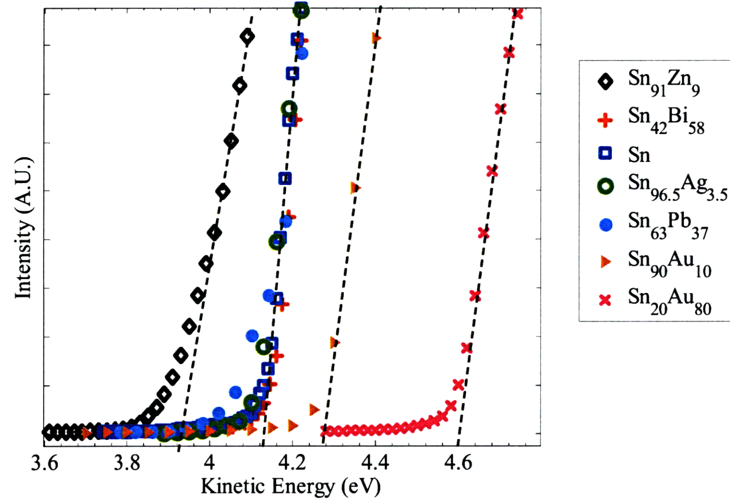

Fig. 2.5. Onset of photoemission for seven tin alloys.

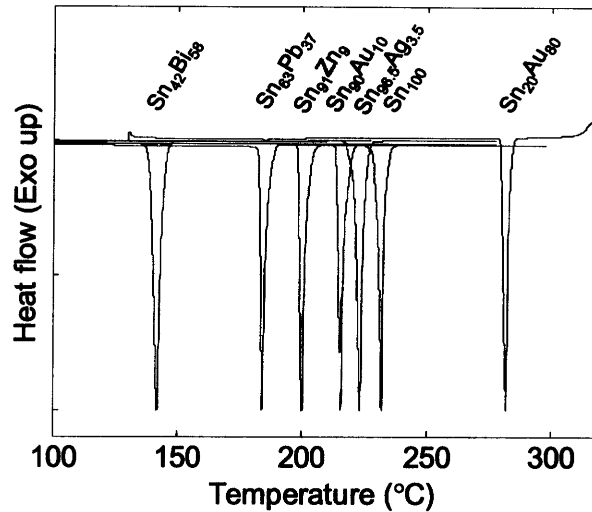

Fig. 2.5 Melting transition of seven eutectic alloys measured by DSC.

The apparent discrepancies between the KP and UPS measurements may have several causes. The Kelvin probe method can be very precise but measures only the difference in work function between sample and tip. Thus unaccounted for deviations in the probe head work function would introduce a constant shift in the measured work function value. Although the KP measurements were done under inert atmosphere and the tip is also expected to resist oxidation, adsorption of even inert gases may cause shifts in the sample work function. The work function of gold has been observed to shift up to 0.4 eV under different atmospheres.[33] More likely, however, is that the difference in work function measured by the two methods is due to the methods themselves. The KP method essentially measures a capacitance per area. Thus the KP determined work function is an area weighted average of all work function patches underneath the probe head. Photoemission spectroscopy is much more sensitive to the lowest work function patch, as the lowest kinetic energy electrons originate from this area. The work function of different facets of crystals is known to differ. Thus the surface of a polycrystalline sample

would be expected to have patches of several different work functions. The addition of entirely separate crystalline phases, as is the case in these eutectic alloys, add even more possibilities. Indeed the difference in work function by the two methods is not surprising. A similar offset has been observed in KP and UPS work function measurements of indium-tin-oxide.[37] Perhaps the most commonly cited value for the work function of polycrystalline tin is 4.42 eV, measured by contact potential difference.[35] The work function of tin has also been measured to be 4.18 eV using the Fowler photoelectric method.[38] Thus both our results for the work function of tin (4.47 eV and 4.14 eV, measured by KP and UPS, respectively) are consistent with the literature.

Although the work function is a surface pheonomen, the alloy valence bands were measured by UPS to give some insight into the total alloy character. For example, the similarity of the Sn, $Sn_{96}Ag_4$, $Sn_{57}Bi_{43}$, and $Sn_{74}Pb_{26}$ valence bands shown in figure 2.8 suggest they are dominated by a single tin phase. Their work functions differ by no more than 30 meV from UPS and 100 meV from KP.

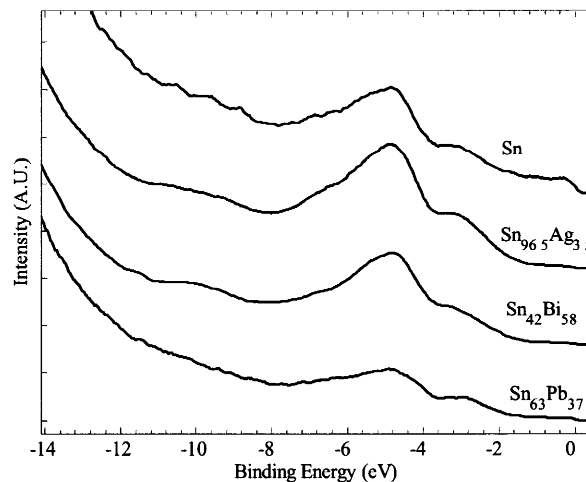

Fig. 2.8. Valence band of Sn, $Sn_{96}Ag_4$, $Sn_{57}Bi_{43}$, and $Sn_{74}Pb_{26}$. The alloys' Fermi levels are taken to be the zero of binding energy.

The $Sn_{85}Zn_{15}$ alloy's valence band shows zinc-like character, having discrete binding energy states at approximately 4.8 and 11 eV (figure 2.9). The work function of the alloy is also noticeably smaller than that of tin (4.12 and 3.92 eV, by KP and UPS, respectively). Thus zinc, with its low work function of 3.6 eV,[35] makes a substantial contribution to the overall electronic character of the alloy even though it is only 15 at% of the alloy.

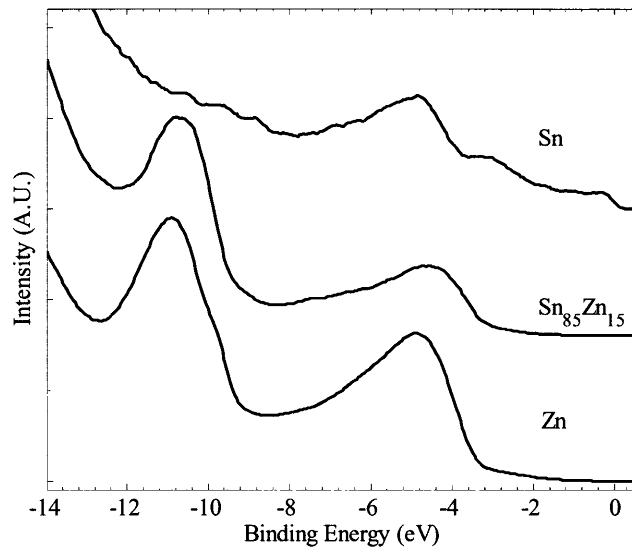

Fig. 2.9. Valence band of Sn, $Sn_{85}Zn_{15}$, and Zn determined by UPS.

The valence bands of the gold-tin eutectic alloys ($Sn_{90}Au_{10}$ and $Sn_{20}Au_{80}$) are given in figure 2.10 and unique in that they show definite gold character despite the fact that tin has a much lower work function. One may tentatively assign some alloy phases to the peaks by comparing with a previous study by Friedman, et al. who looked at the electronic structure of several alloys in the tin-gold system, including the ordered AuSn and $AuSn_4$. For example, the peaks in the $Sn_{90}Au_{10}$ sample, a composite of pure tin and

$AuSn_4$, at -6.8 and -5.3 eV match Friedman's data for $AuSn_4$. So the alloy does show some intermetallic character. The valence band peaks of the $Sn_{20}Au_{80}$ alloy at -6.3 and -4.5 eV cannot be assigned to AuSn, however.

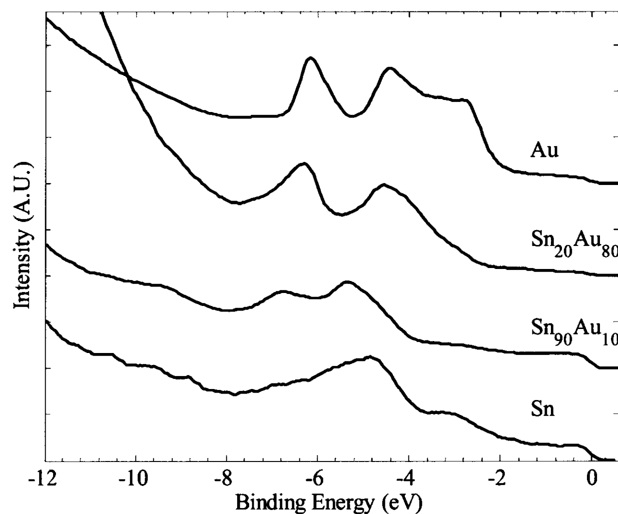

Fig. 2.10. Valence band of Sn, $Sn_{93.8}Au_{6.2}$, $Sn_{29.4}Au_{70.6}$, and Au measured by UPS.

2.5 Conclusions

The work function is an important property of materials in many technological applications. The ability to engineer materials with specific work functions and other properties, such as processing temperature is highly desired. The work function of several tin alloys was measured by the Kelvin technique and ultraviolet photoemission spectroscopy in order to determine their potential utility in rectifying multimaterial fiber devices. The results between the two methods agree quite well, although there is a constant offset between of about 300 meV. This difference may be due to surface cleanliness, preparation, or composition variations. Some difference is expected between the two techniques is expected because they fundamentally measure two different things. The Kelvin probe technique is a capacitive method that measures an area-weighted

average work function, while UPS is most sensitive to low work function regions of the sample. The measurements show that the work function of tin can be shifted by 600 meV by alloying with specific elements while maintaining a single melting transition, necessary for compatibility with multimaterial fiber drawing. Comparison of the alloys' valence band structure also gives insight into the nature of the chemical bonding within the alloy. Knowledge of the work function of alloys compatible with the fiber drawing process is expected to enable more electronically complicated structures to be built into future fibers.

2.6 References

1. Abouraddy, A. F. *et al.* Towards Multimaterial Multifunctional Fibres that See, Hear, Sense and Communicate. *Nature Materials* **6**, 336-347 (2007).

2. Gordy, W. & Thomas, W. J. O. Electronegativies of the Elements. *Journal of Chemical Physics* **24**, 439-444 (1956).

3. Yamamoto, S., Susa, K. & Kawabe, U. Work Functions of Binary Compounds. *Journal of Chemical Physics* **60**, 4076-4080 (1974).

4. Nethercot, A. H. Prediction of Fermi Energies and Photoelectric Thresholds Based on Electronegativity Concepts. *Physical Review Letters* **33**, 1088-1091 (1974).

5. Gelatt, C. D. & Ehrenrei.H. Charge-Transfer in Alloys - AgAu. *Physical Review B* **10**, 398-415 (1974).

6. Fain, S. C. & McDavid, J. M. Work-Function Variation With Alloy Composition - Ag-Au. *Physical Review B* **9**, 5099-5107 (1974).

7. Korolkov, V. A., Malov, Y. I. & Markov, A. A. Electron Work Function of Indium-Bismuth and Indium-Lead Binary System Alloys. *Fizika Metallov I Metallovedenie* **40**, 1312-1314 (1975).

8. Korolkov, V. A., Malov, Y. I. & Markov, A. A. Electron Work function of Alloys in Binary-Systems Bismuth-Antimony, Cadmium-Bismuth, and Tin-Lead. *Soviet Electrochemistry* **12**, 570-571 (1976).

[9] Malov, Y. I., Korolkov, V. A. & Markov, A. A. Electron Work Functions of Binary-Alloys of Copper-Antimony, Copper-Indium, and Copper-Cadmium Systems. *Soviet Electrochemistry* **13**, 1061-1063 (1977).

[10] Malov, Y. I., Markov, A. A. & Korolkov, V. A. Electron Work Function of Alloys of Cadmium-Zinc-Antimony System. *Zhurnal Fizicheskoi Khimii* **51**, 1510-1512 (1977).

[11] Malov, Y. I., Markov, A. A. & Korolkov, V. A. Electronic Work Functions of Antimony Alloys with Tin, Indium, and Zinc. *Soviet Electrochemistry* **12**, 1580-1582 (1976).

[12] Onishchenko, A. V., Malov, Y. I. & Lazareva, V. I. Electron Work Function of Binary Metallic Alloys with Sodium. *Fizika Metallov I Metallovedenie* **51**, 659-661 (1981).

[13] Li, W., Wang, Y., Cai, M. & Wang, C. W. An electronic criterion for the intrinsic embrittlement of structural intermetallic compounds. *Journal of Applied Physics* **98** 083503 (2005).

[14] Auciello, O. *et al.* Review of Synthesis of Low-Work Function Cu-Li Alloy Coatings and Characterization of the Field Emission Properties for Application to Field Emission Devices. *Journal of Vacuum Science & Technology B* **19**, 877-883 (2001).

[15] Macaulay, J. M., Brodie, I., Spindt, C. A. & Holland, C. E. Cesiated Thin-Film Field-Emission Microcathode Arrays. *Applied Physics Letters* **61**, 997-999 (1992).

[16] Thomas, R. E. & Gibson, J. W. Work Function Variation Versus Alloy Concentration for Dispenser Cathodes. *Applied Surface Science* **29**, 49-66 (1987).

[17] Szczudlo, Z., Ciszewski, A. & Losovyj, Y. B. Field Electron Emission Study of Ti and Hf Adsorption Layers on W. *Applied Surface Science* **174**, 138-147 (2001).

[18] Suzuki, H. Fabrication of Electron Injecting Mg:Ag Alloy Electrodes for Organic Light-Emitting Diodes with Radio Frequency Magnetron Sputter Deposition. *Applied Physics Letters* **69**, 1611-1613 (1996).

[19] Tsui, B.-Y. & Huang, C.-F. Wide Range Work Function Modulation of Binary Alloys for MOSFET Application. *IEEE Electron Device Letters* **24**, 153-155 (2003).

[20] Polishchuk, I., Ranade, P., King, T. S. & Hu, C. Dual Work Function Metal Gate CMOS Transistors by Ni-Ti Interdiffusion. *IEEE Electron Device Letters* **23**, 200-202 (2002).

21 Matsukawa, T. *et al.* Work Function Controllability of Metal Gates Made by Interdiffusing Metal Stacks with Low and High Work Functions. *Microelectronic Engineering* **80**, 284-287 (2005).

22 Chen, B., Biswas, N. & Misra, V. Electrical and Physical Analysis of MoTa Alloy for Gate Electrode Applications. *Journal of the Electrochemical Society* **153**, G417-G419 (2006).

23 Zhong, H. *et al.* Properties of Ru-Ta Alloys as Gate Electrodes for NMOS and PMOS Silicon Devices. *International Electron Device Meeting*, 20.25.21-20.25.24 (2001).

24 Todi, R. M., Erickson, M. S., Sundaram, K. B., Barmak, K. & Coffey, K. R. Comparison of the work function of Pt-Ru binary metal alloys extracted from MOS capacitor and Schottky-barrier-diode measurements. *IEEE Transactions on Electron Devices* **54**, 807-813 (2007).

25 Vayenas, C. G., Bebelis, S. & Ladas, S. Dependence of Catalytic Rates on Catalyst Work Function. *Nature* **343**, 625-627 (1990).

26 Sachtler, W. M. H. & Dorgelo, G. J. H. The Surface of Copper-Nickel Alloy Films: I. Work Function and Phase Composition. *Journal of Catalysis* **4**, 654-664 (1965).

27 Sachtler, W. M. H. & , J., R. The Surface of Copper-Nickel Alloy Films: II. Phase Equilibrium and Distribution and Their Implications for Work Function, Chemisorption, and Catalysis. *Journal of Catalysis* **4**, 665-671 (1965).

28 Bouman, R. & Sachtler, W. M. H. Photoelectric Determinatino of the Work Function of Gold-Platnium Alloys. *Journal of Catalysis* **19**, 127-140 (1970).

29 Bouman, R. & Sachtler, W. M. H. Photoelectric Investigation of the Surface Composition of Equilibrated Pt-Ru Alloy Films in Ultrahigh Vacuum and in the Presence of CO. *Journal of Catalysis* **26**, 63-69 (1972).

30 Bouman, R., Lippits, G. J. M. & Sachtler, W. M. H. Photoelectric Investigation of the Surface Composition of Equilibrated Ag-Pd Alloy Films in Ultrahigh Vacuum and in the Presence of CO. *Journal of Catalysis* **25**, 350-361 (1972).

31 Ley, L. & Cardona, M. *Photoemission in Solids I.* (Springer, 1978).

32 Baikie, I. D., Vanderwerf, K. O., Oerbekke, H., Broeze, J. & Vansilfhout, A. Automatic Kelvin Probe Compatible with Ultrahigh Vaccum. *Review of Scientific Instruments* **60**, 930-934 (1989).

33 Hansen, W. N. & Johnson, K. B. Work Function Measurements in Gas Ambient. *Surface Science* **316**, 373-382 (1994).

[34] Orf, N., Baikie, I., Shapira, O. & Fink, Y. Work Function Engineering in Low Temperature Alloys. *Applied Physics Letters* (2009).

[35] Lide, D. R. *CRC Handbook of Chemistry and Physics*. Vol. 89 (CRC Press, 2008).

[36] Seah, M. P., Clifford, C. A., Green, F. M. & Gilmore, I. S. An Accurate Semi-Empirical Equation for Sputtering Yields I: Argon Ions. *Surface and Interface Analysis* **37**, 444-458 (2005).

[37] Kim, J. S. *et al.* Kelvin Probe and Ultraviolet Photoemission Measurements of Indium Tin Oxide Work Function: A Comparison. *Synthetic Metals* **111-112**, 311-314 (2000).

[38] Alchagirov, B. B., Kurshev, O. I., Taova, T. M. & Khokonov, K. B. Electron Work Function in Alloys from the Tin-Lead System. *Technical Physics* **51**, 1624-1626 (2006).

Chapter 3: Materials Selection and Characterization: Insulators and Semiconductors

3.1 Introduction

Numerous criteria go into selecting the correct materials and compositions for a multimaterial device fiber. The perform fabrication and thermal fiber drawing processes are very demanding in a number of respects and the proper choice of materials is very much a goldilocks problem of balances the desires of functionality with the realities of processing, as was alluded to in chapter 2. Certain materials combinations of metals, insulators, and semiconductors are desired to optimize device performance, but these disparate materials must all have overlapping thermal processing temperatures if they are to be combined in a meaningful way. Further complicating the problem, the exact definition of processing temperature changes between materials. For example, the metals described in chapter 2 are crystalline materials with discrete transitions from solid (infinite viscosity) liquid (low viscosity on the order of 10^{-3} Poise) at the melting temperature, T_m. In contrast, amorphous materials which are most often used in thermal fiber drawing undergo a gradual transition from solid to liquid, beginning at the glass transition temperature, T_g, and are typically processed in the viscous state during thermal fiber drawing. The potential incorporation of *non-amorphous* (i.e. crystalline) semiconductors into multimaterial device fibers offers enhanced electrical properties over their amorphous counterparts but also new fabrication challenges.

This chapter will review the pertinent electrical, optical, and thermomechanical properties of semiconducting and insulating materials potentially compatible with the manufacture of multimaterial rectifying device fibers. First the processing temperatures

of different insulating polymers that serve both as a protective cladding and device substrate will be reviewed. Then semiconductors potentially useful for fabrication of rectifying device fiber will be identified and characterized. The thermo-mechanical properties of these semiconductors must be then matched to that of the other components including the polymer cladding and metal electrodes, and the ability to modulate these properties with composition (as typified by the glass transition temperature) will be shown. This information will be combined with information of the melting temperature and work function of the metal alloys measured in chapter 2 to fabricate the desired rectifying device fiber in the next chapter.

3.2 Insulators

Polymers are commonly used in the optical fiber industry. This is due, at least in part, to the fact that they may be engineered to be transparent in specific wavelengths of interest and made completely amorphous. The optical properties of the polymers are important for different applications. But it is the non-crystalline nature of the polymer that makes it compatible with thermal fiber drawing at all. Unlike crystalline materials, amorphous materials exhibit a gradual change in viscosity from the solid to liquid states, beginning at the glass transition temperature. This temperature corresponds to the point at which larger sections of the polymer molecule begin to have enough thermal energy for large scale molecular rearrangement. As the temperature continues to increase the polymer becomes a viscous fluid and deforms under applied stress or over long times. Thermal fiber drawing occurs in this regime. Eventually the temperature increases to the point where the polymer itself flows so easily that it is considered a liquid, although its

viscosity will not be as low as a metal's by virtue of the polymer molecules' extended length and entanglement between chains. The glass transition temperature and optimal fiber drawing temperature (observed for our draw tower) is listed for several high-temperature amorphous thermoplastics in table 3.1. Each of these polymers has been shown to be suitable for fiber drawing and certain multimaterial device fiber applications. Although their optical properties, such as transparency, change somewhat, all are satisfactory for the intended purpose of mechanical support and electrical insulation while allowing incident light to impinge on the device. It is interesting to note that the transparency of these specific polymers tends to increase with decreasing processing temperature.

Table 3.1. Glass transition and fiber drawing temperature for amorphous thermoplastic polymers compatible with multimaterial fiber fabrication.

Polymer	Glass Transition Temperature (°C)	Approximate Fiber Drawing Temperature (°C) (at furnace)
TOPAS 6013 Cyclic Olefin Copolymer (COC)	138	205
LEXAN 104 Polycarbonate (PC)	150	205
UDEL P1700 NT11 Polysulfone (PSU)	180	255
RADEL A Polyethersulfone (PES)	225	290
ULTEM 1000 Polyetherimide (PEI)	225	290
ULTEM XH6050 Polyetherimide (HT-PEI)	240	320

3.3 Semiconductors

3.3.1 Amorphous Chalcogenide Semiconductors

Chalcogenide glasses are a class of inorganic glasses that have mobility gaps in the 1-2 eV range, making them photosensitive and potential candidates for fiber-based electro-optical devices. In fact, these good glass formers, such as the prototypical As_2Se_3, may be thermally processed in a fashion similar to amorphous polymers and have been used in optical fiber processing for several different purposes. Furthermore, they may be modified with a variety of other elements to adjust their optical and thermo-mechanical properties to suit the needs of each application. As an example, a series of glasses in the $As_2(S\text{-}Se\text{-}Te)_3$ family were fabricated to demonstrate how the glass transition temperature (figure 3.1) and absorption edge (figure 3.2) change with composition. The T_g of the glasses was measured by differential scanning calorimetry (DSC), at a 2 degree per minute scan rate from low to high temperature. By convention the glass transition was taken to be the inflection point of the heat flow of the endothermic even. The absorption was calculated from the Beer-Lambert law,

$$I = I_o \exp\left(\frac{-4\pi k}{\lambda} l\right), \quad (3.1)$$

for an arbitrary film thickness (l=200nm in this case), with the imaginary part of the index of refraction, k, was determined by ellipsometry.[1] The figures clearly show that increasing concentration of smaller chalcogens such as sulfur increases the softening temperature and optical band gap (onset of absorption approaches shorter wavelengths).

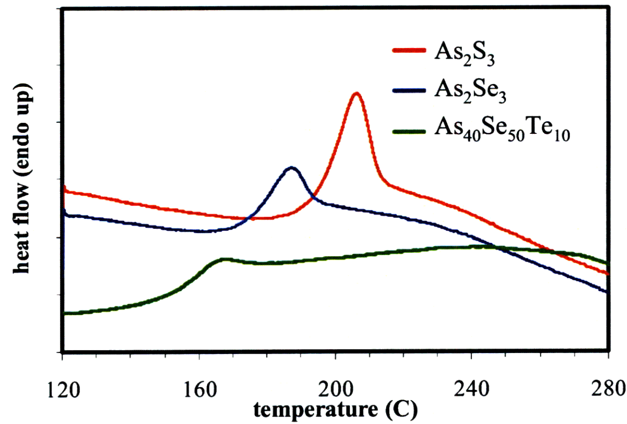

Fig. 3.1. DSC scans for three different chalcogenide glasses demonstrating that softening temperature increases as the average chalcogen size decreases.

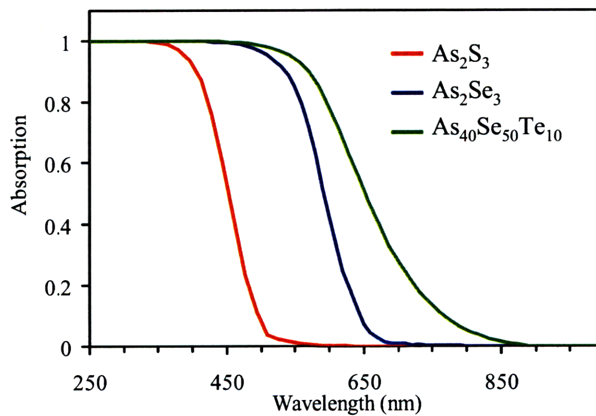

Fig. 3.2. Absorption of light for three chalcogenide glasses as a function of wavelength. As the concentration of larger chalcogen elements increases the absorption edge shifts to short wavelengths, signifying an increase in optical gap size.

The same density of defects that is advantageous in terms of amorphous processing is detrimental to the material's electrical properties, and chalcogenide glasses such as As_2Se_3 may have resistivities upwards of 10^{12} Ωcm. This is not surprising, as the very high concentrations of defects (on the order of 10^{18} cm^{-3}) effectively pin the Fermi level to the center of the optical gap.[2] They cannot be made more conductive by doping because concentration of active dopants must exceed that of the intrinsic defects; and,

because there is no long range network within the glass enforcing a specific coordination number, modifiers introduced into the system tend to not be electronically active, i.e., they do not contribute additional carriers to the system. Adding enough modifier so that the number of electronically active additives compensates the intrinsic defect concentration is not a viable solution because the concentration necessary to achieve this is so large (greater than 1%) that the atomic network is actually being changed so that this is more like alloying than doping. The conductivity can however be controlled by adding modifiers to change the width of the mobility gap. This makes intuitive sense because the defect-filled glasses have their Fermi levels pinned to the center of the bandgap, and the only way to decrease the activation energy for conduction (distance between Fermi level and band edge) short of doping would be to decrease the gap distance. Figure 3.3 demonstrates that the logarithm of conductivity is proportional to the band gap. This confirms the trend observed in figure 3.2 where the addition of smaller chalcogens increases the bandgap and semiconductor resistivity. The relationship between conductivity, σ, and bandgap, E_g, for amorphous chalcogenide glasses is often expressed as

$$\sigma \propto e^{\frac{-E_g}{2k_bT}} \quad .(3.2)$$

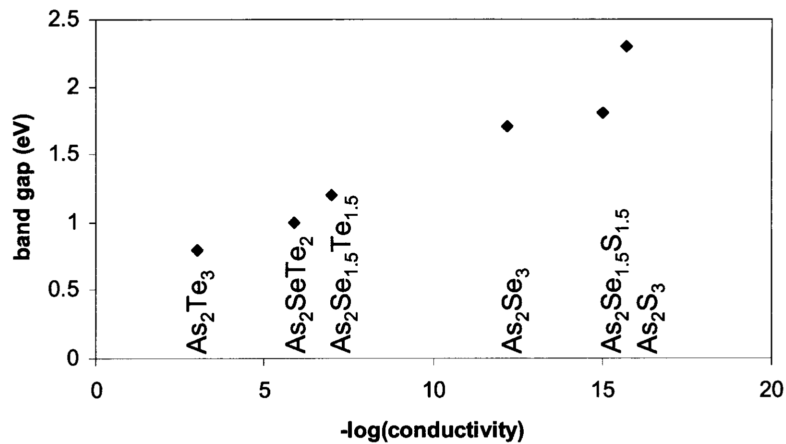

Fig. 3.3. Variation of bandgap and conductivity for the As-(S,Se,Te) family of glasses.

3.3.2 Crystalline Chalcogenide Semiconductors

In addition to inducing large resistivities in amorphous chalcogenide semiconductors, the density of defects is thought to preclude the ability to create meaningful electronic band-bending in electronic devices composed of chalcogenide glasses. Thus it is likely that the number of electronic defects in chalcogenide semiconductors will need to be significantly reduced if they are to be used in multimaterial fiber based rectifying devices. One way to reduce the density of defects is to use crystalline instead of amorphous semiconductors. Large volumes of crystalline materials are not expected to be suitable candidates for fiber drawing because of their discontinuous change in viscosity at the melting temperature, due to their ordered nature. However recognizing that the amorphous state is meta-stable, an amorphous material may be driven to the equilibrium crystalline state with the application of heat and time. How this can be achieved in a fiber fabrication framework will be discussed in the next chapter. For the present discussion we will simply state that this fact creates the

possibility to get the benefit of amorphous processing and crystalline electronic performance and discuss the relevant properties of a family of sulfur-selenium alloys.

3.3.2.1 Thermal Properties of Crystalline Selenium

Elemental selenium is one chalcogenide glass that may be easily converted between the amorphous and crystalline states. The possible use of selenium is also advantageous because there is a wide body of work investigating selenium-based semiconductor devices. Indeed, the first discoveries of semiconductor properties such as photoconductivity and the photovoltaic effect were found in selenium. Selenium is an unstable glass, it may be glassy or crystalline at room temperature and devitrifies readily upon heating. Whereas As_2Se_3-based crystals melt at temperatures upwards of 375°, which is far above the processing temperature of any available polymer, crystalline selenium melts at an experimentally convenient 230°C.[3] Additionally, liquid selenium maintains the same sort of polymer-like chain structure that exists in the solid state resulting in a melt-viscosity of approximately 10^0 Poise, with little temperature dependence.[4,5] Compared to typical liquids, this extra viscosity may be important for maintaining structural integrity throughout fiber processing and drawing.[6] A schematic drawing of the thermo-mechanical properties of metals, amorphous materials, and selenium is given in Figure 3.4.

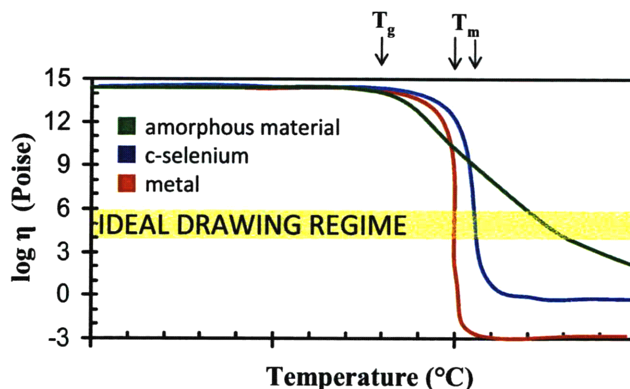

Fig. 3.4. Schematic diagram of viscosity as a function of temperature for elemental selenium and prototypical amorphous and crystalline materials.

The thermomechanical properties of selenium may be modified in the same way as other chalcogenide glasses. However, in contrast to the trends seen in glassy As(S,Se,Te), the addition of sulfur *decreases* the glass transition and melting temperatures, T_m, of selenium compositions. This is readily seen in figure 3.5 which shows DSC scans (heating rate 10°/min) of selenium and three sulfur-selenium alloys. Unlike the higher-temperature, and strong glass forming As_2Se_3-based alloys, additional exothermic thermal events can be seen. These correspond to the crystallization temperature, T_x, of the alloys. Little correlation is seen between T_x and the composition. This may be a measurement artifact or be due to the fact that all compositions are crystallizing into slightly different structures. Each alloy has a different atomic mobility at T_x due to the different glass transition temperatures, and this may play a role as well.

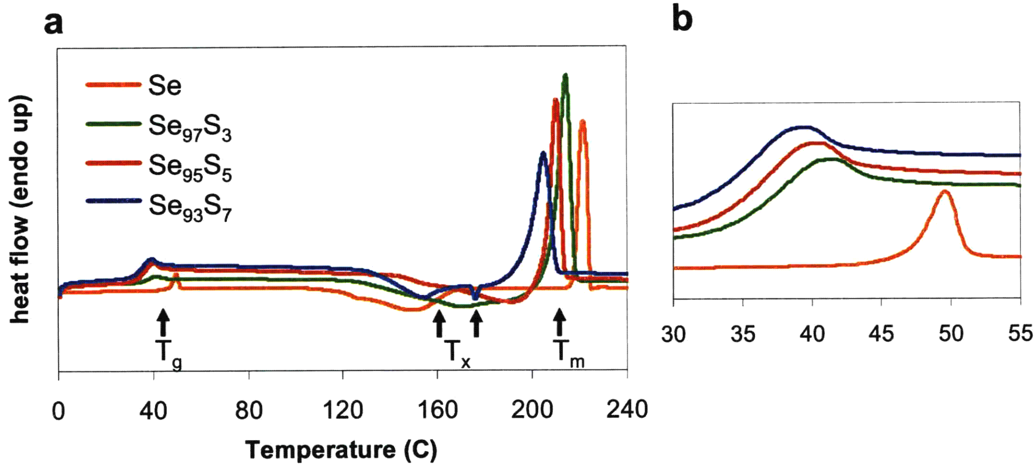

Fig. 3.5. (a) DSC scans of four selenium alloys demonstrating how glass transition and melting temperatures decrease with the addition of sulfur. (b) Magnification of glass transition region in (a).

3.3.2.2 Electrical Properties of Crystalline Selenium

Conductivity, carrier type, concentration, and mobility are important parameters for semiconductor devices and can be limiting factors in performance of high quality devices. They are related to each other by the equation

$$\sigma = nq\mu \text{, (3.3)}$$

where σ is conductivity (inverse of resistivity, Ωcm), n is the carrier concentration (cm^{-3}), μ is the mobility ($cm^2V^{-1}s^{-1}$), and q is the elemental charge. Usually the conductivity is straightforward to measure. The mobility can be slightly more complicated, and the carrier concentration is often determined by first finding the conductivity and mobility and using equation 3.3. The carrier type, concentration, and mobility of several sulfur-selenium alloys were measured by the Hall Effect. Thin-film transistors (TFTs) of one particular alloy, $Se_{97}S_3$, were constructed to verify the mobility and carrier concentration through an additional method.

One straightforward method of determining the mobility, carrier concentration, and carrier type in crystalline semiconductors is via the well-known Hall Effect, named after Edwin Hall who discovered the phenomenon in 1879. Imagine a thin section of material having current flowing in the *x* direction and a transverse electric field in the *z* direction (figure 3.6).

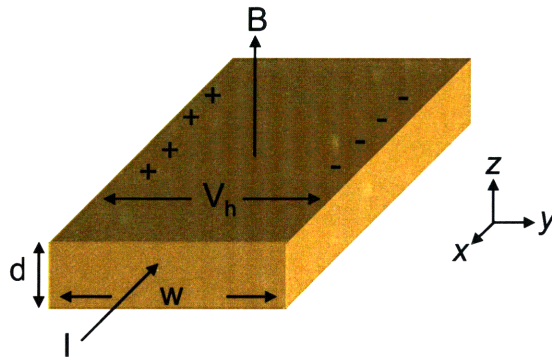

Fig. 3.6. Schematic diagram of Hall Effect measurement.

The force on the charge carriers traveling in the *x*-direction due to B_z is given by the Lorentz relationship:

$$F_y = q\bar{v} \times B_z \, . \, (3.4)$$

Where $\bar{v}$ is the velocity of the charge carrier given by the current equation:

$$I = qnwd\bar{v} \;\; .(3.5)$$

As no current can flow in the *y*-direction, a potential develops to balance the Lorentz force

$$F_y = qE_y = \frac{qV_{hall}}{w} \, .(3.6)$$

At equilibrium these forces balance and

$$V_{hall} = \frac{-B_z I}{ndq} . (3.7)$$

Thus, for a given applied magnetic field and current a transverse voltage can be measured, and the carrier concentration can be determined. The carrier type is also determined by the sign of the induced voltage. The mobility of the carrier can then be simply determined by the relationship:

$$I = nq\mu V .(3.8)$$

Using a Bio-Rad hall probe, the resistivity, mobility, and thus carrier density have been measured for several thin-film polycrystalline selenium sulfur alloys and summarized in table 3.2.

Table 3.2. Hall Effect derived resistivity, mobility and carrier density for 3 sulfur-selenium alloys.

	ρ (x10^5 Ωcm)	μ (cm^2/Vs)	Carrier density (x10^{11} cm^{-3})
Se	1.5	4.2	545.0
$Se_{97}S_3$	3.5	3.0	9.95
$Se_{95}S_5$	4.6	2.97	45.4

Another common method of extracting semiconductor parameters is through characterization of field effect transistors fabricated from the material. In short, a transistor is a three terminal device whereby the current through two terminals (the source and drain in MOSFET terminology) can be modulated by a third (the gate). In field effect devices, this modulation comes by the application of a voltage across a dielectric layer resulting in the build-up of charges on either side of the layer as if it were a capacitor. This change in carrier concentration at the surface of the dielectric layer can form high- (or low-) conductivity channels between the source and drain resulting in

large (or small) currents for a given bias. The physics of the typical field-effect device has been thoroughly studied and are described in greater detail in different references. [7]

A typical silicon MOSFET used in modern microelectronics runs in inversion mode. The source and drain contacts are n (or p) doped, while the channel between them is doped oppositely. In thermal equilibrium, this configuration acts as a back-to-back diode and little current flows between source and drain. When a voltage is applied between the gate and common source, the charging of the capacitor creates an excess of holes or electrons on the dielectric surface. If the gate is biased in such a way to increase the density of channel's majority carriers, it is even more difficult for current to flow between the source and drain. However, if the gate is biased in the opposite direction the density of majority carriers is reduced until, when sufficiently biased, inversion occurs and an excess of minority carriers now exists. At this threshold voltage, V_T, a high conductivity channel spans the distance between the source and drain and currently flows more readily. In this linear regime, the drain-source current is directly proportional to the drain-source voltage, V_{DS}, the carrier concentration, and carrier mobility. As V_{DS} becomes larger than V_{GS}-V_T, a depletion region begins to form around the drain contact and pinches off the high conductivity channel between source and drain. This pinched-off region is not a barrier to carrier flow as one might expect because the field between the source and drain pulls the carriers to the contact. However, the drain-source current is no longer controlled by the drain-source voltage and the device is said to be in saturation. For small V_{DS} (the linear region) the current flow through the transistor can be expressed as

$$I_{DS} = \frac{w}{L}\mu C_{ox}\left(V_G - V_T + \frac{V_D}{2}\right)V_D \ . \ (3.9)$$

While in saturation $V_{DS}^{sat}=V_G-V_T$, and the current follows the form

$$I_{DS}^{sat} = \frac{W}{2L}\mu C_{ox}(V_G - V_T)^2 \; . (3.10)$$

The field effect mobility in the linear regime is typically extracted from the derivative $\partial I_{DS}/\partial V_{GS}$, called the transconductance or g_m. In the linear regime when $V_{DS} << V_{GS}$ and

$$g_m = \frac{\partial I_{DS}}{\partial V_G}|_{V_D} = \frac{W}{L}\mu C_{ox} V_D \; . (3.11)$$

In saturation, the mobility is typically extracted from a plot of $\sqrt{(I_{DS})}$ versus V_{GS} with the help of equation 3.10. Thin-film transistors typically run in accumulation mode, meaning that the high conductivity channel is composed of majority carriers instead of minority carriers. But the basic principles are still the same, and the above equations intended for inversion-mode devices work well in describing a device's behavior.

Thin-film transistors composed of thin layers of $Se_{97}S_3$ (~300nm) contacted by gold source and drain electrodes were fabricated on doped silicon wafers with a 100nm oxide. The channel length and width was 100μm and 2mm, respectively. Figure 3.4 shows the drain-source current as a function of drain-source voltage for several gate voltages.

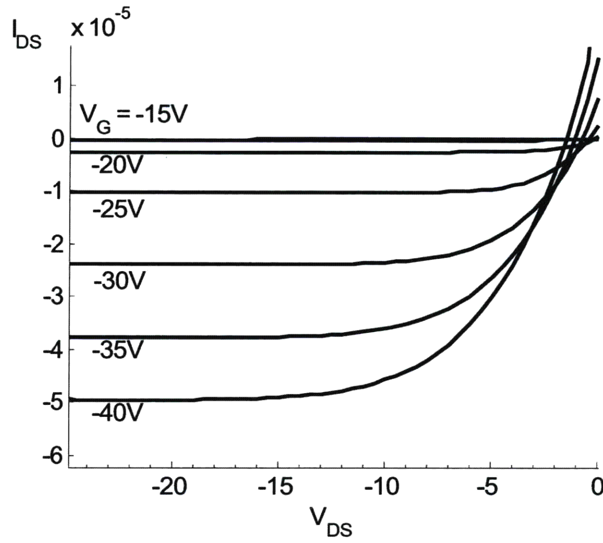

Fig. 3.7. Current-voltage output characteristics for $Se_{97}S_3$ TFT.

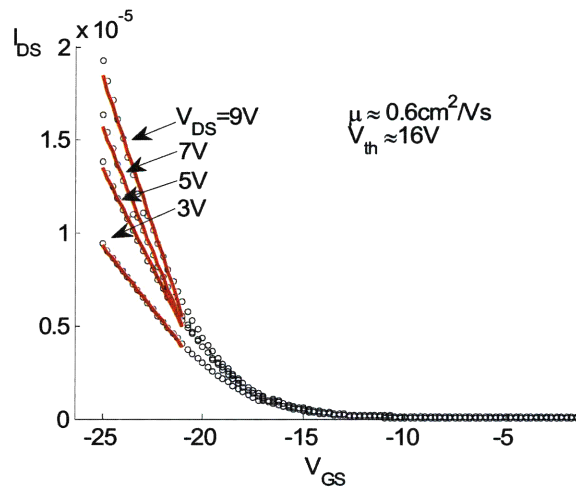

Fig. 3.8. Transfer Characteristics of $Se_{97}S_3$ TFT with extracted mobility and threshold voltage using equation 3.11.

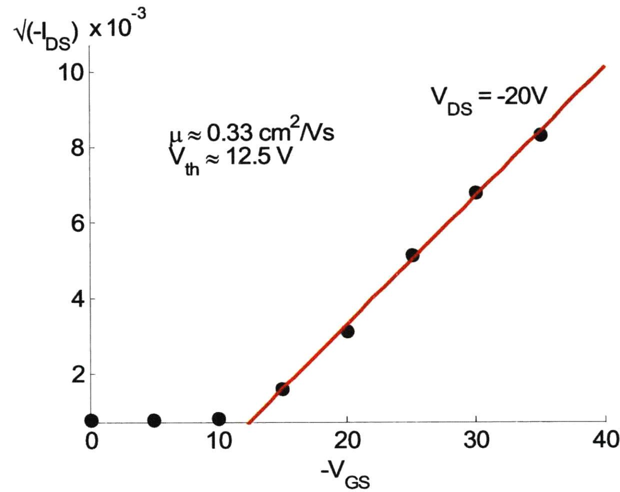

Fig. 3.9. Square root of drain-source current as a function of gate voltage for $Se_{97}S_3$ TFT in saturation with extracted values of mobility and threshold voltage using equation 3.10

Using the equations above, the field effect mobility is found to be 0.6 and 0.33 cm^2/Vs in the linear and saturation regimes, respectively. This is unique because the saturation mobility is typically found to be larger than the linear regime mobility. The I_{DS} vs. V_{DS} transition from negative to positive current between the source and drain does not occur at zero bias as expected, but is in fact a function of gate bias, this is an indication gate leakage through the oxide and may explain the large turn-on voltage. Nevertheless, the measured field effect mobilities are within an order-of-magnitude of the Hall Effect mobility, which is very reasonable. Traps and interfacial defects at the dielectric/semiconductor may be a source of this difference. Indeed the large gate threshold voltage for such a small dielectric layer implies that a significant number of traps must be filled before carrier accumulation occurs.

3.3.2.3 Band structure of crystalline Selenium

As described in section 2.3, ultraviolet photoemission spectroscopy (UPS) can be used to determine the location of both the valence band maximum and Fermi level in semiconductors. Selenium is known to be a p-type semiconductor whos work function is normally found to be approximately 5.9 eV[8,9], while the valence band maximum or ionization potential is cited to be 6.1 eV.[9,10] The valence band maximum and work function was measured for a polycrystalline film of $Se_{97}S_3$ with UPS using the same procedure as in section 2.4. Figure 3.10 shows the photoemission onset (a) and valence band structure (b) of the film. Note that two different conventions are used in labeling the *x*-axis for (a) and (b). Figure 3.10a presents the photoemission as a function of the kinetic energy of the escaping electron, while figure 3.10b presents photoemission as a function of semiconductor binding energy, where the zero in binding energy is defined to be the Fermi level. The two conventions are easily converted between each other by equation 2.10.

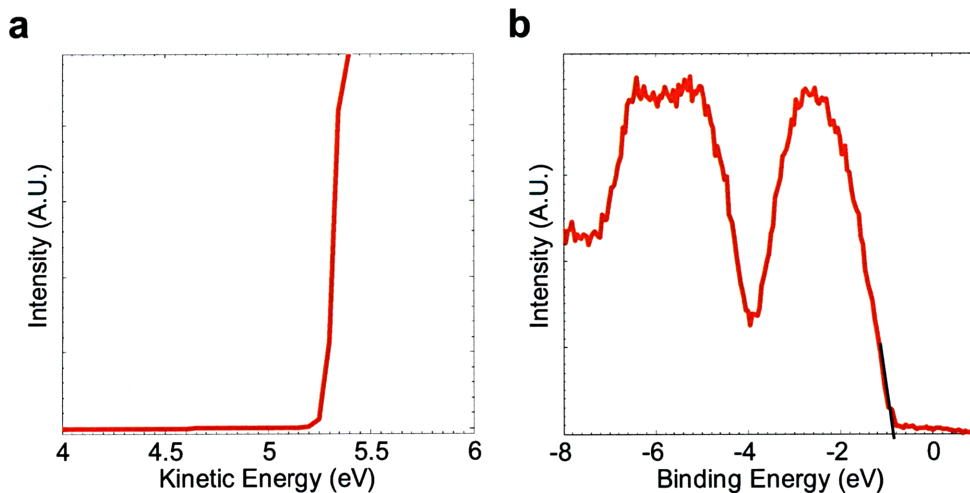

Fig. 3.10. (a) UPS photoemission onset of polycrystalline $Se_{97}S_3$ film. (b) Valence band structure. Black line is extrapolation to zero intensity, which is equivalent to the valence band maximum of the semiconductor.

The onset of photoemission is equal to the work function in semiconductors even though there are very few states at this level. This is because the low energy onset of photoemission is due to secondary electrons scattered and ejected by several inelastic collisions within the semiconductor. Even though there are very few states available within the band gap, electrons can undergo various relaxations before reaching and exiting the surface. Thus these secondary electrons can have any energy greater than the minimum escape energy (the work function) regardless of the density of available equilibrium states within the semiconductor. Figure 3.10 shows that the work function of the $Se_{97}S_3$ film is approximately 5.3 eV, and the difference between the Fermi level and valence band is about 0.9 eV, suggesting that the valence band maximum occurs at about 6.2 eV below the vacuum level. The apparent large discrepancy between the work function presently measured and the literature may be due to differences in composition or different defect densities on the surface. The sputtering process can induce a large number of defects by creating dangling and unsaturated bonds. These defects can cause the Fermi level to actually change from the bulk to the surface. The addition of sulfur or the polycrystalline nature of the film may also be sources of this work function shift.

3.4 Conclusions

Materials selection is a major challenge in the fabrication of multimaterial device fibers, and the difficulty is only expected to grow as new functionalities are incorporated. This chapter reviewed the relevant electronic and thermo-mechanical properties of insulators and semiconductors that will be important in fabricating the rectifying device fibers. Amorphous thermoplastic polymers and chalcogenides have a wide range of

thermal processing regimes and exhibit the continuous change in viscosity with temperature necessary to achieve and maintain high viscosity during fiber drawing. The increased atomic order in crystalline chalcogenides such as selenium have significantly improved electronic properties compared to their amorphous counterparts. In the next chapter, the materials properties data measured for metals (chapter 2), insulators, and semiconductors (chapter 3) will be used to identify materials combinations that may be used in the construction of a multimaterial rectifying device fiber.

3.5 References

1. Benoit, G. & Fink, Y. *Database of Optical Constants*, <http://mit-pbg.mit.edu/Pages/DataBase.html> (2003).

2. Tsiulyanu, D. *Heterostructrures of Chalcogenide Glasses and Their Applications*. Vol. 2 (Elsevier, Inc, 2004).

3. *Alloy Phase Diagrams*. Vol. 3 (ASM International, 1992).

4. Abouelela, A. H., Sharaf, K. A. & Labib, H. H. A. Viscosity of Liquid Selenium and Selenium-Sulfure Mixtures. *Applied Physics a-Materials Science & Processing* **26**, 203-206 (1981).

5. Laugier, A., Chaussemy, G. & Fornazero, J. Viscosity of Glass-Forming Ge-Se Liquid Solutions. *Journal of Non-Crystalline Solids* **23**, 419-429 (1977).

6. Deng, D. S. *et al.* In-Fiber Semiconductor Filament Arrays. *Nano Letters* **8**, 4265-4269 (2008).

7. Sze, S. & Ng, K. *Physics of Semiconductor Devices*. 3rd edn, (Wiley-Interscience, 2006).

8. Lide, D. R. *CRC Handbook of Chemistry and Physics*. Vol. 89 (CRC Press, 2008).

9. Champness, C. H. & Chan, A. Relation Between Barrier Height And Work Function in Contacts to Selenium. *Journal of Applied Physics* **57**, 4823-4825 (1985).

[10] Williams, R. H. & Polanco, J. I. Electronic-Structure of Chalcogenide Solids - Photoemission Study of Ordered and Disordered Selenium and Tellurium. *Journal of Physics C-Solid State Physics* **7**, 2745-2759 (1974).

Chapter 4: Fabrication of Multimaterial Rectifying Device Fibers

4.1 Motivation

Multimaterial composite fibers have made it possible to realize optoelectronic device functionalities at fiber optic length scales and cost. Furthermore, the structured preform-to-fiber fabrication method enables the incorporation of multiple devices into a single fiber and multiple fibers into large area sensors.[1] Devices built to date contain only ohmic metal-semiconductor-metal photoconductor junctions. The inclusion of rectifying junctions into the fibers is highly desirable because it would allow even greater functionality to be introduced into the fiber devices, but the amorphous nature of the chalcogenide semiconductors has made this goal unattainable thus far. Non-crystallinity is necessary during fiber fabrication because the structured preform cross-section is maintained into the fiber during thermal drawing only when the viscosity of the materials is large enough to extend the time-scale of breakup driven by surface tension effects in the fluids to times much longer than that of the actual drawing. Unfortunately, the same disorder that is so helpful to the semiconductors' thermal processing is detrimental to their electronic properties, imparting large resistivities and effectively pinning the Fermi level near mid-gap. Indeed, the defect density within the mobility gap of many chalcogenides has been found to be 10^{18}-10^{19} cm^{-3} eV^{-1}, resulting in a narrow depletion width and ohmic behavior at metal-semiconductor junctions.[2] Therefore an important step in developing rectifying fibers is incorporating crystalline semiconductors (or other lower defect density semiconductors) into fiber. Beyond this, combinations of metals and semiconductors must be identified that may form rectifying junctions and are also compatible with the fiber drawing technique. This chapter will describe how crystalline semiconductors may be built into

fibers,[3] how the best material combinations for creating a rectifying junction were identified, and the tools and techniques that were developed to introduce the right materials combinations in the right geometries to get the best possible device performance.

4.2 Post-drawing thermal annealing

Non-crystallinity is necessary to maintain viscosity during drawing, but it serves no purpose afterward. One may recognize that the amorphous phase is a meta-stable state and that this phase may be used for fabrication as before but then drive it to the equilibrium crystalline state by thermal annealing after drawing. Although all amorphous materials can devitrify, the time to achieve this can be substantial. Thinking of crystallizing glasses in the context of fiber processing is a paradigm shift from traditional fiber processing which strives to use materials that will remain as glassy as possible to reduce the density of crystallites and grain boundaries that can act as scattering sites and reduce the efficiency of light transmission through the fiber. All multimaterial device fibers built to date have also taken a similar approach and made use of stable glasses that would not crystallize during processing or afterwards in any reasonable time.[1]

Glass compositions can be chosen that are just stable enough to withstand the rigors of fiber drawing but can still be thermally annealed into the equilibrium crystalline state within a reasonable time frame. One such glass, based on the traditionally very stable As_2Se_3, is $As_{40}Se_{52}Te_8$. Fibers consisting of solid cores of this glass, tin electrodes, and PES cladding were drawn and annealed for different times and temperatures. The annealing temperature should be as high as possible above the glass transition temperature of the semiconductor so that the molecules have enough thermal energy to begin to rearrange into the equilibrium structure. However, the multimaterial nature of the fiber also sets limits on the annealing temperature as it

must be less than the metal electrode melting temperature and the glass transition of the polymer. This requirement sets a practical temperature limit of about 210 °C for PES fibers. As semiconductor crystallinity increases, one would expect to see a change in resistance. Indeed this is the case, and this change in resistance can be used as a measure of ordering as a function of annealing time. Figure 4.1 shows the resistance of a solid core $As_{40}Se_{52}Te_8$ fiber as a function of annealing time at 210 °C. Amazingly the resistance changes 5 orders of magnitude over the course of 20 days.

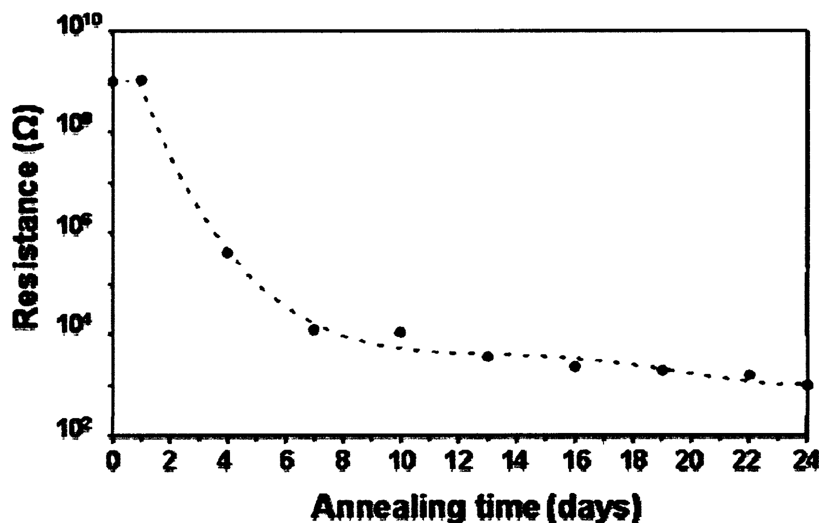

Fig. 4.1. Fiber resistance as a function of annealing time at 210 °C. Dashed lines serve as guides to the eye. (figure courtesy S. Danto).

Although this is strong evidence that a dramatic structural change is occurring, direct confirmation of the semiconductor crystallinity is preferred. Figure 4.2 shows an SEM micrograph of an amorphous fiber cross-section and a powder x-ray diffraction pattern of $As_{40}Se_{52}Te_8$ extracted from a drawn fiber without further processing. The pattern shows diffuse peaks corresponding to an amorphous material with two peaks from residual tin attached to the semiconductor. After extended annealing, x-ray diffraction measurements still show broad peaks characteristic of amorphous materials, but there are also several sharp peaks corresponding to

crystalline As_2Se_3-based phases (figure 4.3b). SEM micrographs (figure 4.3a) also show presence of crystallites originating from interfaces between the semiconductor and metal or insulator. This is to be expected because the activation energy for heterogeneous nucleation at boundaries between materials is much less than that of homogeneous nucleation. The figures also suggest that most current between the electrodes is carried by the crystalline layer. Hence even though a majority of the semiconductor is still amorphous, the resistance only decreases marginally with further annealing after the initial high conductivity path between the electrodes is created.

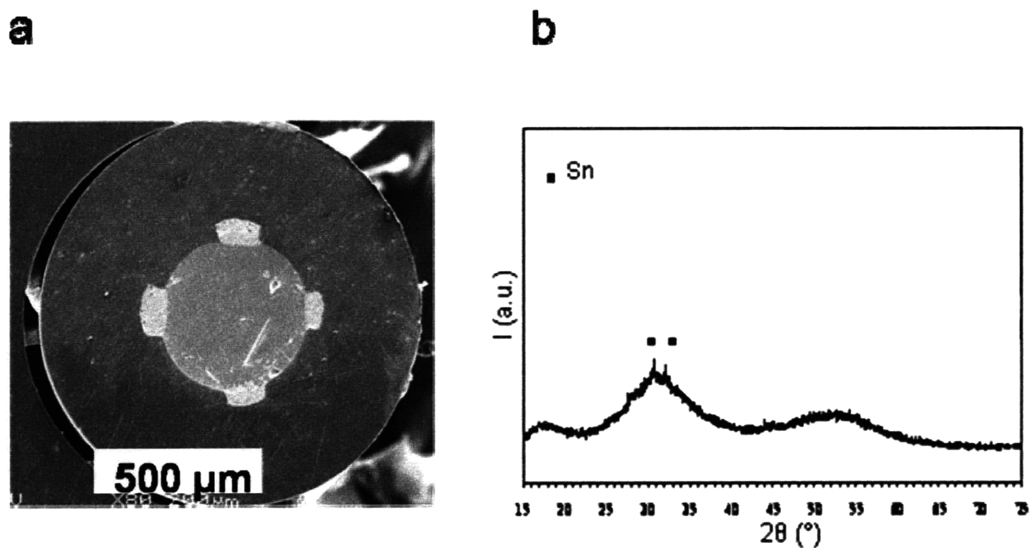

Fig. 4.2. (a) SEM micrograph of fiber after thermal drawing. (b) Powder XRD pattern of amorphous semiconductor core with remnants of attached tin electrodes (figure courtesy S. Danto).

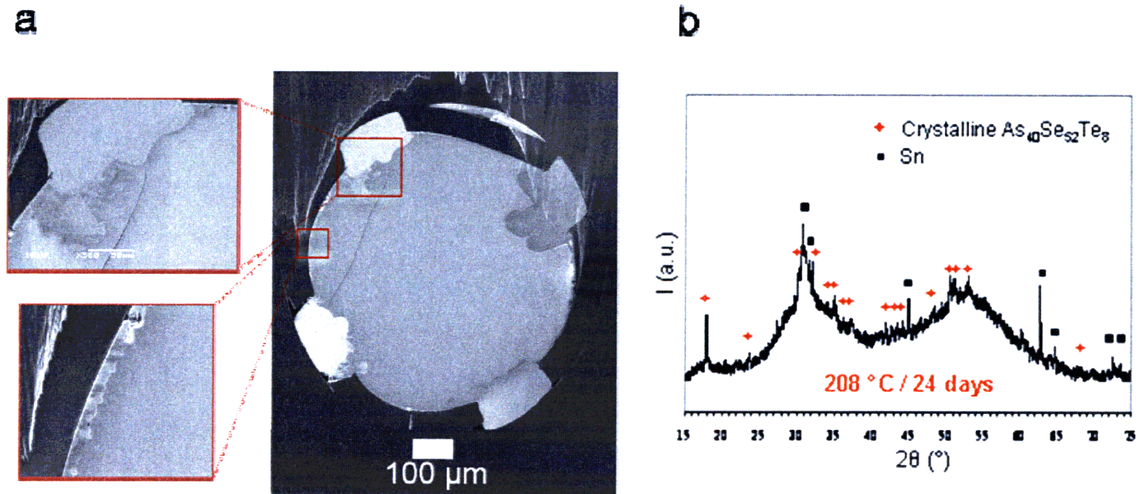

Fig. 4.3. (a) SEM micrograph of fiber after extended thermal annealing. (b) Powder XRD pattern of semiconductor core demonstrating crystalline semiconductor phases (figure courtesy S. Danto).

This method of post-drawing annealing is attractive because it allows one to take advantage of the amorphous phase's thermal processing as well as the crystalline phase's electrical properties. The introduction of crystalline semiconductors into the fiber is an important step in creating diode device fibers, but there is no guarantee that it will result in non-ohmic behavior. Indeed, these first crystalline device fibers also act as photoconductors whose current-voltage characteristics are linear and give no indication of any internal electric fields or barriers to current flow.

4.3 Materials Selection and Rectifying Device Fiber Fabrication

At this point it is worthwhile to evaluate all the materials compatible with the multimaterial fiber fabrication approach and which combinations are likely candidates for forming rectifying junctions. As junction formation is often driven by differences in work function between materials, it makes sense to identify combinations of semiconductors, and

possibly metals, which have large work function differences. Elemental selenium is an ideal semiconductor candidate for many reasons. First, crystalline selenium is a semiconductor with a work function among the highest of all elements (~6 eV).[4,5,6] Selenium may even be considered the first semiconductor in many respects because photoconductivity and the photovoltaic effect were first discovered in selenium.[7] The discovery of the photovoltaic effect was probably directly due to the fact that the work function of selenium is so large that under normal circumstances a rectifying barrier forms between it. Selenium was also the semiconductor of choice for making electronic devices before the advent of silicon processing, so there is a wide body of literature on selenium-based electronic devices. Work today continues in the field even though the semiconductor composition has shifted from pure (or doped) selenium to copper-indium-selenide semiconductors for solar cells. Secondly, all chalcogenide glasses incorporated into multimaterial fibers thus far have been based on the glassy nature of selenium, so it is reasonable to expect that pure selenium may itself be compatible with the fabrication method. The material's melting temperature of ~220 °C[4] is certainly within the realm of composite fiber processing. Finally, selenium is an unstable glass that may be amorphous or crystalline at room temperature and is easily converted between the two. All of these traits make selenium an ideal candidate for the semiconductor material in multimaterial rectifying fiber devices.

Although the stable chalcogenide glasses are based on the chain-like atomic structure and glassy nature of selenium, the element itself readily crystallizes when above its glass transition temperature of about 30 °C. As discussed in section 3.3.2.1, the viscosity of crystalline selenium does not vary quasi-continuously with temperature as it does in amorphous materials. It behaves more like a metal in the sense that it has a discrete melting temperature and an abrupt change in viscosity at that point. The viscosity of liquid selenium is also different than metals, though,

because the chain structure of the molecules create entanglements that impart some viscosity to the melt. Whether or not this viscosity (on the order of 10^0 Poise) is high enough that the structure will be maintained during fiber drawing is another question. Hart developed a model that predicted a film this viscosity but surrounded by a higher viscosity material could indeed be maintained during fiber drawing as long as the film thickness did not drop below a particular level.[8] Deng and this author showed experimentally that this minimum thickness is approximately 100 to 200 nm in the fiber.[9]

The work on the minimum thickness of selenium films as well as the present work on diode devices requires the determination of the optimal selenium alloy and polymer combination. It was found that although PES fiber processing occurred at a sufficiently high temperature to melt selenium, the consolidation temperature was also high enough that films of selenium within PES preforms melted and dewet into droplets during preform consolidation. It was found that the combination of pure selenium and PSU did not work either because although the semiconductor film survived consolidation, it did not melt during drawing. As a result the selenium films were not continuous in the fiber, even though they started that way in the preform. A solution was found by alloying selenium with elements that depressed the melting temperature. Potential alloying candidates included elements commonly used in chalcogenide glass making: arsenic, germanium, sulfur, and tellurium. Arsenic and germanium exhibit three- and four-fold bonding, respectively, and act as cross-linking agents in selenium's chain structure. Their addition would be useful, because they would allow the selenium viscosity to be better controlled. Germanium however is very difficult to thermally evaporate simultaneously with selenium and is generally not preferred for applications involving the evaporation of thin films. Sulfur and tellurium are candidates because they have some solubility in crystalline selenium.

Tellurium is completely soluble in selenium, but the addition of tellurium to selenium increases the alloy melting temperature and is thus not suitable for the present application. The addition of sulfur does depress the alloy melting temperature as desired and small amounts are completely soluble in selenium (up to about 10 at%). In the end it was found that the addition of 2 to 3 at% sulfur depressed the alloy melting temperature just enough that it melted with PSU during fiber drawing. Even though arsenic is also a potential candidate, arsenic is not soluble in crystalline selenium and precipitates out as As_2Se_3, and the amount of arsenic necessary to make a noticeable increase in viscosity was found to be around 15 at%. Thus the addition of 3 at% sulfur was found to be the best way to adapt selenium to fit the PSU processing regime with as little modification as possible.

With a potential combination of semiconductor and insulator identified, a way to create rectifying junction to the selenium must be found. Several test preforms composed of crystalline $Se_{97}S_3$ and contacted by several combinations of metal alloys were made. The selected metals were chosen based on their melting temperature, which as discussed in chapter 1, must be less than the thermal fiber drawing temperature. Indeed, because the $Se_{97}S_3$ alloy was found to be the highest temperature alloy that could be drawn with PSU, the upper limit of metal melting temperature must be close to that of $Se_{97}S_3$, or approximately 215 °C (see figure 3.5). Figure 4.4 shows the current voltage characteristics of these preform-level fiber devices.

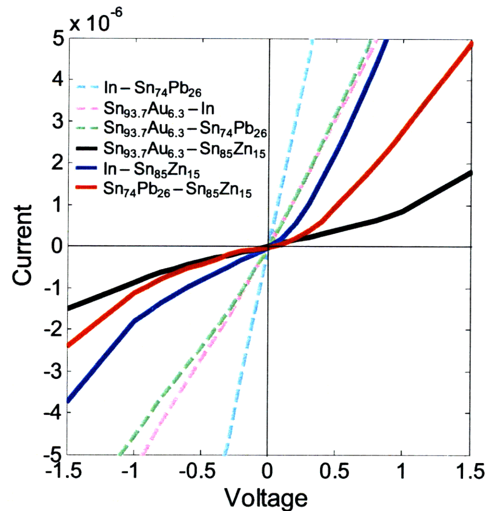

Fig. 4.4. Current-voltage characteristics of metal-$Se_{97}S_3$-metal devices (metal composition given in at%).

Upon inspection of figure 4.4 it is immediately obvious that most combinations of metals result in ohmic behavior despite the large work function difference between the metals (measured in chapter 2 to between approximately 4 and 4.5 eV) and the crystalline selenium (found in chapter 3 to be between 5.3 and 6 eV). In fact only when one of the electrodes is $Sn_{85}Zn_{15}$ (at%) do the devices show any non-linear current-voltage behavior. This result is curious and will be expanded upon later. For now it is sufficient to say diode behavior may be achieved with the combination of $Sn_{85}Zn_{15}$ – $Se_{97}S_3$. Additional fiber draws with different various counter electrodes found that common lead-tin eutectic solder, $Sn_{74}Pb_{26}$ (at %), functioned the best.

Having identified a set of materials that is compatible with the fiber fabrication method and exhibits the desired rectifying behavior, we must now create the fiber structure and optimize it for performance. Figure 4.5 shows the evolution of the diode fiber as new techniques were developed to improve this performance. Initial devices were modeled after thin-film photodetecting fibers developed by Dr. Fabien Sorin.[10] As described in chapter 1 these fibers are constructed by wrapping a semiconductor film around a supporting polymer tube and then

sliding an additional polymer tube having slots cut out for the electrodes on top. More layers of polymer film are wrapped around the semiconductor film and electrodes to form the final protective cladding. The electrodes in these original devices were set 90 degrees from each other, but the large distance between the electrodes results in a large series resistance. The first attempts at reducing this series resistance resulted in the type of fiber shown in 4.5a. In this device, two closely spaced sets of electrodes were built into the electrode tube by cutting spaces into the tube with an endmill. In this original technique, the location of each cut was manually positioned, resulting in non-uniformities between different electrode pairs within a single fiber and different fiber draws. This non-uniformity can be eliminated and the distance between electrode pairs can be slightly decreased if the electrode tube is positioned by an indexing device that rotates the tube at specific angles (fig. 4.5b). Furthermore, positioning the film on top of the electrodes instead of underneath the electrodes increases the amount of light incident on the junction by reducing shadowing by the electrodes. Moving the film from the inside to the outside of the electrodes was found to increase the photocurrent by 3-5 times.

Although the indexer can be used to position the cut locations on the tube very precisely, it was found that decreasing the cut separation below 1-2mm was impractical because the lack of mechanical support caused the remaining tube began to vibrate. These vibrations resulted in the tool cutting jagged lines that did not contain the electrode well but can be eliminated by cutting the electrode spaces directly into the inner support tube. As the electrode thickness is now much smaller than the diameter of the tube, the walls next to the electrode spaces no longer vibrate during cutting and the distance between electrodes can be decreased even further (fig. 4.5c). In fact the electrode spacing can be decreased until the distance between electrodes at their outer diameter is substantially different than their inner diameter (see SEM micrographs in 4.5c). At

this point the spacer walls start to be deformed by the electrodes and the number of short circuits between electrodes increases substantially.

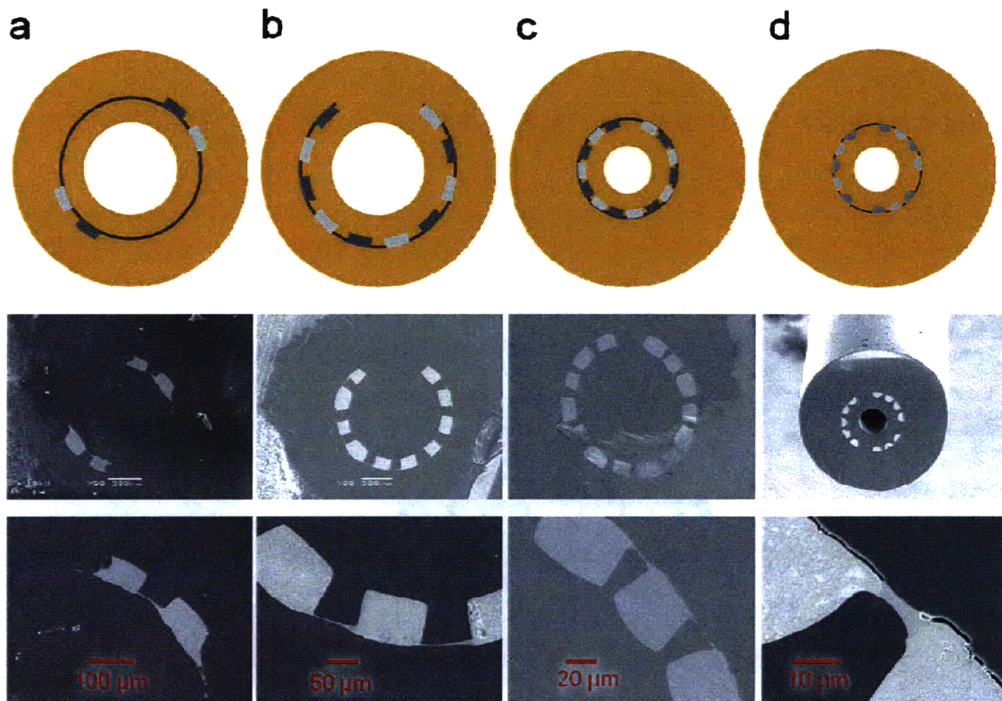

Fig. 4.5. Schematic diagrams and SEM micrographs of evolution of diode device fibers. (a) Initial design based on previous thin-film photodetector fibers. (b) Placing the semiconductor outside of the electrodes reduces shadowing and greatly increases photo-generated current, and the device density can be increased. (c) Device density can be further increased by milling electrode spaces into a thick tube rather than a thin tube. (e) Using semicircular electrodes reduces the stress of metal on thin polymer spacers, increasing yield.

The solution to this problem is to use *semi-circular* electrodes. The curvature of the semi-circular shape ensures that the nearest point between electrodes occurs only at the semiconductor connection. With these techniques the spacing between electrodes can be decreased at the preform level to 0.5mm and drawn down to 10-15 µm in the fiber, more than an order of magnitude smaller than all previous multimaterial fiber devices. Figure 4.6 shows a schematic

diagram of the final preform being drawn into tens of meters of fiber and magnifications of the fiber and an individual electrode pair.

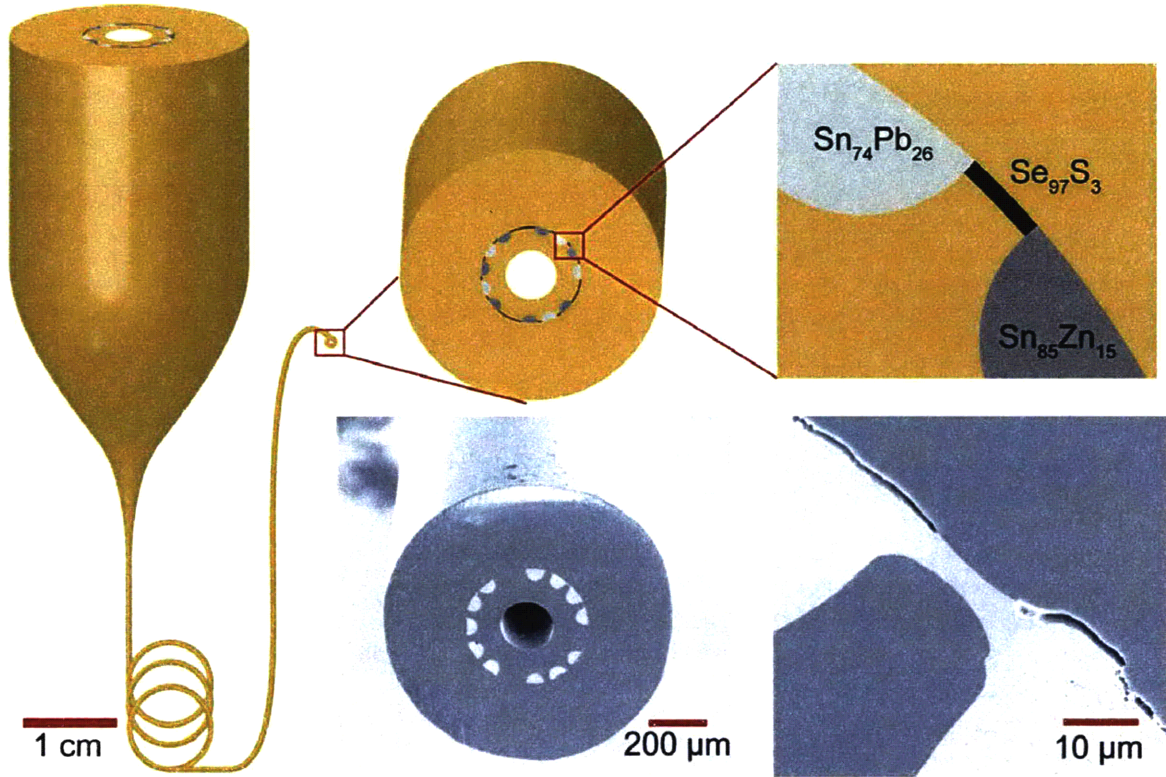

Fig. 4.6. Schematic diagram and SEM micrographs of final design from preform to fiber.

4.4 Conclusions

The methods described in this chapter have been used to create the first arbitrarily long in-fiber diode. A method was developed to introduce crystalline semiconductors into the fiber while still preserving amorphous nature of the semiconductor. Further experiments revealed the optimal combination of metals ($Sn_{85}Zn_{15}$ and $Sn_{74}Pb_{26}$) and semiconductor ($Se_{97}S_3$). The preform fabrication process was refined and the distance between electrodes decreased by an order of magnitude from previous devices. Chapter 5 will characterize the performance of these in-fiber crystalline diodes as well as determine the origin of the rectifying nature of the junction.

4.5 References

[1] Abouraddy, A. F. *et al.* Towards multimaterial multifunctional fibres that see, hear, sense and communicate. *Nature Materials* **6**, 336-347 (2007).

[2] Tsiulyanu, D. in *Semiconducting Chalcogenide Glass III: Applications of Chalcogenide Glasses* Vol. 80 eds Robert Fairman, Boris Ushkov, Robert Kent Williardson, & Eicke Weber) Ch. 2, 144 (Elsevier, 2004).

[3] Danto, S. *in preparation* (2009).

[4] Lide, D. R. *CRC Handbook of Chemistry and Physics*. Vol. 89 (CRC Press, 2008).

[5] Williams, R. H. & Polanco, J. I. Electronic-Structure of Chalcogenide Solids - Photoemission Study of Ordered and Disordered Selenium and Tellurium. *Journal of Physics C-Solid State Physics* **7**, 2745-2759 (1974).

[6] Champness, C. H. & Chan, A. Relation Between Barrier Height And Work Function in Contacts to Selenium. *Journal of Applied Physics* **57**, 4823-4825 (1985).

[7] Nelson, J. *The Physics of Solar Cells*. (Imperial College Press, 2004).

[8] Hart, S. D. *Multilayer Composite Photonic Bandgap Fibers* Ph. D. thesis, Massachusetts Institute of Technology, (2004).

[9] Deng, D. S. *et al.* In-Fiber Semiconductor Filament Arrays. *Nano Letters* **8**, 4265-4269 (2008).

[10] Sorin, F. *et al.* Multimaterial photodetecting fibers: a geometric and structural study. *Advanced Materials* **19**, 3872 (2007).

Chapter 5: Multimaterial Rectifying Device Fiber Characterization

5.1 Introduction

Having developed a method of fabricating diode devices in the fiber, we must now characterize them. This chapter describes the electrical characterization (using standard current-voltage and capacitance-voltage measurement techniques) and metal-semiconductor interface characterization (using energy dispersive spectroscopy and Kelvin force microscopy) of the device used to understand the nature of the device. By combining these techniques the origin of the rectifying behavior can be explained and an electronic band diagram of the system constructed. Finally the applicability of the fiber diode will be measured by several common photodetector metrics such as the responsivity, detectivity, and frequency response.

5.2 Electrical Characterization

5.2.1 Background

Basic analysis of the electronic performance of this new diode device fiber requires some background on the formation of rectifying barriers between metals and p-type semiconductors and the equations that describe their behavior. The analysis presented here is meant to give a cursory introduction to the idealized schottky junction as it relates to the diode characterization in this chapter. The interested reader is referred to other sources for in-depth explanation and analysis of rectifying behaviors.[1]

When two different materials are brought into intimate contact a driving force develops to align their Fermi levels. This force is due to the difference in electronic work

function (the difference between the vacuum and Fermi levels) between the materials which causes mobile electrons to diffuse from the lower work function material (which is relatively electron rich) to the larger work function material and holes to diffuse in the opposite direction. As the mobile carriers diffuse according to their concentration gradient, they leave behind fixed compensating charges such as ionized dopants or metal ions. An electric field develops between the fixed charges on either side of the material boundary that opposes the diffusion-guided flow of carriers. In equilibrium the carrier current due to diffusion is equal and opposite to the carrier flow due to electric field drift and there is zero net current. The Fermi levels of the two materials are aligned and the internal electric field results in a difference in potential between either side of the junction, termed the built-in potential, equal to the magnitude of the materials' work function difference. An approximation is typically made that area around the interface is occupied solely by the ionized fixed charges and all the mobile carriers remain at the edge of this depleted region. This is called the depletion approximation. The Poisson equation gives the relationship between electrostatic potential, ψ, and total charge, qN:

$$\frac{d^2\psi}{dx^2} = -\frac{dF}{dx} = \frac{qN}{\varepsilon}, \quad (5.1)$$

where ε is the dielectric constant and F is the electric field. In the general case of a p-type semiconductor contacted to a lower work function metal, holes flow from the semiconductor to the metal and leave behind fixed negative charges and electrons flow in the opposite direction. Because the carrier density in metals is so much greater than in semiconductors, only an infinitely thin layer of metal becomes depleted of mobile charges while a larger volume of semiconductor will be depleted so that the total number of charges on either side of the interface remains the same. Thus all relevant charge

distributions and band bending occur only on the semiconductor side. Setting the field to zero outside the depletion region, w_d, equation 5.1 can be integrated to give

$$\frac{d\psi}{dx} = -F = \frac{qN}{\varepsilon}(x + w_d). \text{ (5.2)}$$

The maximum electric field then occurs at the semiconductor metal interface ($x = 0$) and is equal to

$$F_{\max} = \frac{qN}{\varepsilon} w_d \text{. (5.3)}$$

The potential variation across the junction is found by integrated the electric field in equation 5.2, giving

$$\psi = \frac{qN}{2\varepsilon}(x + w_d)^2 \text{. (5.4)}$$

The maximum potential is thus

$$\psi = \frac{qN}{2\varepsilon}(w_d)^2 \text{. (5.5)}$$

This is the built-in voltage of the device and is equal to the difference in work function between the two materials (in the absence of interface states and other non-idealities). When an additional potential is applied across the junction ψ is replaced by $\psi_{bi} - V$.

It is often of interest to measure the capacitance of the diode junction. The capacitance per unit area of the junction is

$$C = \frac{\varepsilon}{w_d} = \sqrt{\frac{qN}{2\varepsilon(\psi_{bi} - V)}} \text{. (5.6)}$$

This may also be written as

$$\frac{1}{C^2} = \frac{2\varepsilon(\psi_{bi} - V)}{qN} \text{. (5.7)}$$

Thus the built-in voltage of the junction can be determined by measuring the capacitance as a function of applied voltage, and the extrapolation of a plot of C^{-2} versus V to the *x*-intercept yields ψ_{bi}. The slope of the plot may also be used to determine the number of carriers as a function of depletion width:

$$\frac{d\left(\frac{1}{C^2}\right)}{dV} = -\frac{2\varepsilon}{qN} . \quad (5.8)$$

In practice use of equation 5.8 is greatly complicated by the presence of interface states and traps within the bulk of the semiconductor whose occupation will change as a function of applied voltage. Figure 5.1 summarizes the spatial variation in charge (b), electric field (c), potential (d), and energy (e) after an isolated metal and p-type semiconductor pair (a) are brought into contact (e), remembering that the potential, ψ, equals $-qE$, where E is energy and that the valence and conduction bands must follow the same trend because the bandgap of the semiconductor is fixed.

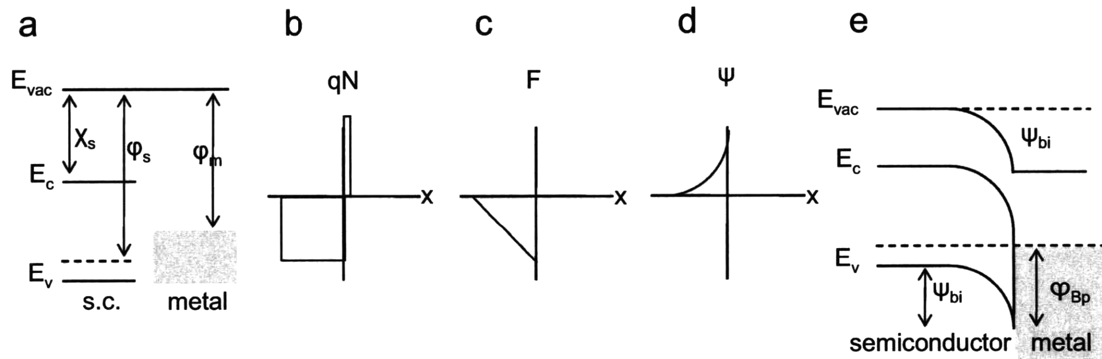

Fig. 5.1. (a) The electronic structure of a p-type semiconductor and metal when they are isolated from each other. When brought into electrical contact, mobile charges flow according to their concentration gradient, but this flow is opposed by an electric field that develops between fixed charges. The resulting charge distribution (b) causes an electric field (c) and potential gradient (d) at the metal-semiconductor interface. The potential change across the junction must be reflected in bending of the vacuum, valence, and conduction bands of the semiconductor.

The current-voltage characteristics can be described by carrier emission over a barrier. At equilibrium the current through the junction is given by the difference between the current flowing over the metal → semiconductor barrier and the current flowing over the semiconductor → metal barrier. It can be seen from geometrical arguments that the minimum energy to overcome the metal-semiconductor barrier, ϕ_{Bp}, in both directions is equal to the difference between the metal work function and the semiconductor valence band maximum, $\Phi_m - (\chi + E_g)$, where χ is the electron affinity or conduction band minimum. This barrier is independent of applied voltage for carriers leaving the metal, but the barrier seen by carriers leaving the semiconductor can be changed by the applied voltage. Using Boltzmann statistics the number of carriers at a given energy is proportional to the energy,

$$N \propto N_0 \exp\left(\frac{-\phi_{barrier}}{kT}\right), \quad (5.9)$$

where N_0 is a constant, k is the Boltzmann constant, T is temperature. The current due to emission over the barrier is related to the carrier velocity, v, and number of carriers, N, by

$$j = qvN. \quad (5.10)$$

Thus the current from metal to semiconductor and vice versa can be written as:[1]

$$j_{m\to s} = A^{**}\exp\left(\frac{-\phi_{Bp}}{kT}\right) \quad (5.11)$$

$$j_{s\to m} = A^{**}\exp\left(\frac{-(\phi_{Bp} - qV)}{kT}\right) \quad (5.12)$$

$$j_{net} = j_{s\to m} - j_{m\to s} = A^{**}\exp\left(\frac{-\phi_{Bp}}{kT}\right)\left[\exp\left(\frac{qV}{kT}\right) - 1\right] \quad (5.13)$$

where A** is called the Richardson constant, which takes into account all the particularities of the situation such as the velocity, the carrier density of states and effective mass. The current equation can be written in the more familiar form by multiplying by the area of the diode to arrive at:

$$I = I_o\left(\exp\left\{\frac{qV}{kT}\right\} - 1\right) \quad (5.14)$$

where I_0 is the diode reverse saturation current. Under most conditions the 1 in 5.14 may be neglected as qV > kT.

When the semiconductor is illuminated with photons having energy greater than its bandgap, absorbed photons may cause electrons to be excited from the valence to conduction band and electron-hole pairs are generated. If these carriers are generated within regions having internal electric fields they will be separated and flow as current if attached to an external load. Current also flows under voltage bias as in any diode. The total current for a given applied load is the superposition of the diode current due to an applied bias, I, and the photo-generated current, termed the short-circuit current, $I_{s.c.}$, because it is equal to the circuit current measured when the load resistance and applied bias are both zero. No current flows when the external load is infinite. The photogenerated carriers are still separated by the internal electric field but accumulate at the edges of the internal electric filed and generate a voltage, called the open-circuit voltage. The open-circuit voltage is ideally equal to the built-in voltage of the semiconductor device but is often less due to non-idealities such as carrier recombination. For small positive applied bias, $V < V_{o.c.}$, the magnitude of the photocurrent due to the internal electric field flowing in the direction opposite the applied voltage is greater than the current due to applied bias. Thus the total current through the device flows in the

direction opposite of the applied bias, and the product of the current and voltage across the device is negative, i.e. the device generates power rather than consuming it. This is the regime in which solar cells are operated, and analysis of the current-voltage characteristics of a device in this regime can give important insight in to the nature of the device.

5.2.2 Experimental

Fiber diodes were constructed as described in chapter 4. $Se_{97}S_3$ was synthesized from high purity elements using standard melt quenching technique. Elements in the correct proportion were inserted into a quartz ampoule under inert atmosphere and then transferred to a vacuum line for additional purification by sublimation of volatile oxides (~2 hours at 190°C). The ampoule was then sealed and inserted into a custom rocking furnace where it was slowly heated to 500°C and mechanically rocked over night to ensure homogenization. The ampoule was then quenched in water, and the glassy compound was removed.

The preform was fabricated by first milling semicircular slots into the outer diameter of 11.1 mm (7/16") polyethersulfone (PSU) polymer tube (inner diameter = 5.0mm) with a Bridgeport endmill. Slot spacing and orientation was kept constant with a digital indexer set to rotate the PSU tube at 24° increments. High purity wires of eutectic $Sn_{74}Pb_{26}$ and $Sn_{85}Zn_{15}$ at% ($Sn_{63}Pb_{37}$ and $Sn_{91}Zn_9$ wt%) from the Indium Corporation of Utica, NY were cut in half lengthwise and tightly fitted into the milled slots. A thick film (~30μm) of $Se_{97}S_3$ was thermally evaporated onto a PSU substrate and then wrapped around the preform core so that the semiconductor and metal electrodes were touching. Additional layers of PSU were then wrapped around the devices to impart mechanical

toughness. The resulting preform was fused into a single solid structure by heating under vacuum at 230°C for 1 hour and then slowly cooled to room temperature. The completed preform (having dimensions ~26mm in diameter, 150mm in length) was then taken to an optical draw tower where it was thermally drawn into tens of meters of fiber (nominal diameter ~1mm) at 260°C.

5.2.3 Results and Discussion

The current-voltage characteristics per unit fiber length as a function of voltage both in the dark and under illumination from a simulated solar source (AM1.5G) for a typical fiber diode is given in figure 5.2. The $Sn_{74}Pb_{26}$ electrode is biased positive with respect to the $Sn_{85}Zn_{15}$ electrode in the forward direction (inset). Rectifying behavior is clearly evident in the dark, the magnitude of which is limited by the device series resistance arising from the lateral photodiode geometry. A short-circuit current and open-circuit voltage (0.5V) develops under illumination, demonstrating the existence of an internal electric field and suggesting future application as a distributed photovoltaic device.

The capacitance as a function of voltage for several frequencies is given in figure 5.3, and the inverse square capacitance at 20 Hz is shown in figure 5.4. A large dispersion in the C-V measurements at different frequencies is indicative of a large density of long-lived trap states exist. Indeed the capacitance drops by more than two orders of magnitude as the frequency of the AC signal increases, indicating that the number of carriers that can move faster than 1 kHz is two orders of magnitude less than those that can move at 20 Hz (because $C=qN/V$).

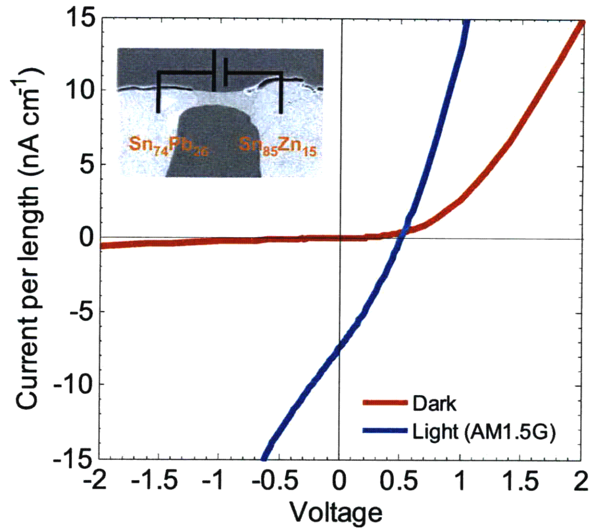

Fig. 5.2. Current-voltage characteristics as a function of fiber length for a typical fiber diode device in the dark (red) and under illumination (blue). The $Sn_{74}Pb_{26}$ electrode is biased positive with respect to the $Sn_{85}Zn_{15}$ electrode in the forward direction (inset).

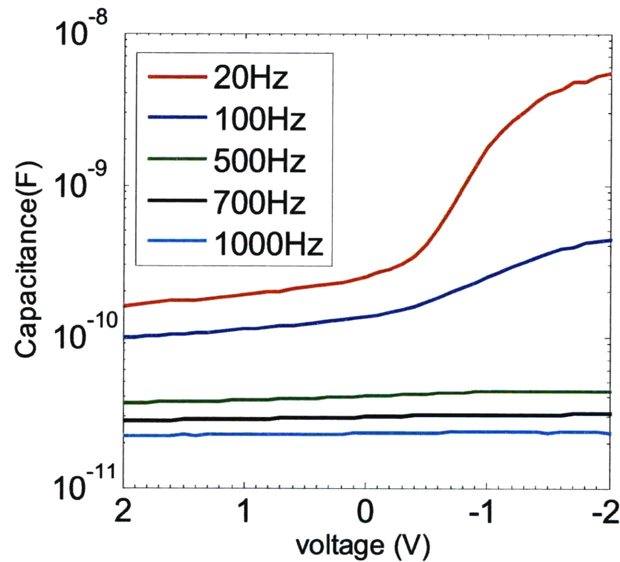

Fig. 5.3. Capacitance as a function of frequency for a typical fiber diode device. The dispersion between measured capacitances indicates a large density of states that trap carriers for hundreds of milliseconds.

Extrapolating the data in figure 5.4 to the *x*-axis yields a built-in voltage of about 0.8 V. The change in slope indicates a spatial variation in the carrier density, consistent with the

existence of interface states at the metallurgical junction. These hypothesized states would also a possible source of the long-lived trap states causing the dispersion in capacitance observed in figure 5.2 and are often invoked to explain capacitance dispersion in metal-oxide-semiconductor structures.[1,2]

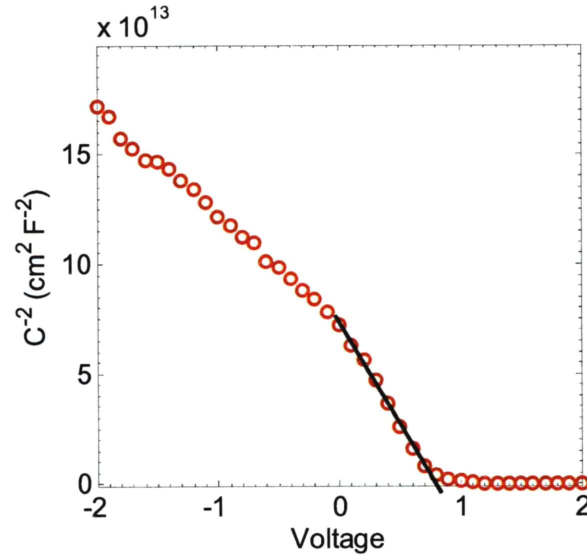

Fig. 5.4. Inverse square capacitance as a function of voltage for fiber diode device when AC signal is 20 Hz.

Non-idealities and loss mechanisms can negatively affect the performance of diode devices. Real devices have finite series resistances, exhibit loss-mechanisms such as traps, carrier recombination, etc., and low-resistance or leaky pathways, termed shunts, through the device that reduce the effective diode barrier. Including these factors, the diode equation may be written as:[3]

$$I = I_o\left(\exp\left\{\frac{qV - IR_{series}}{nkT}\right\} - 1\right) - I_{s.c.} - \frac{V + IR_{series}}{R_{shunt}} \quad , (5.15)$$

where n is an additional factor to account for non-idealities such as generation, recombination, traps, etc, R_{series} is the series resistance of the semiconductor, and R_{shunt} is

the shunt resistance. The ideal maximum power that may be generated by a photovoltaic device is equal to the product $I_{s.c.}V_{o.c.}$ but is typically less. The fill factor is the ratio of the actual maximum power of a real solar cell and the ideal case:

$$FF = \frac{I_{max}V_{max}}{I_{s.c.}V_{o.c.}} = \frac{P_{max}}{P_{ideal}}. \quad (5.16)$$

The power conversion efficiency of the solar cell may be written as

$$\eta = \frac{I_{s.c.}V_{o.c.}FF}{P_{optical}}. \quad (5.17)$$

To illustrate the effects of the series and shunt resistances on a diode under illumination, figure 5.5 shows the current-voltage characteristics of a real diode under AM1.5G simulated solar illumination in the power-generation regime.

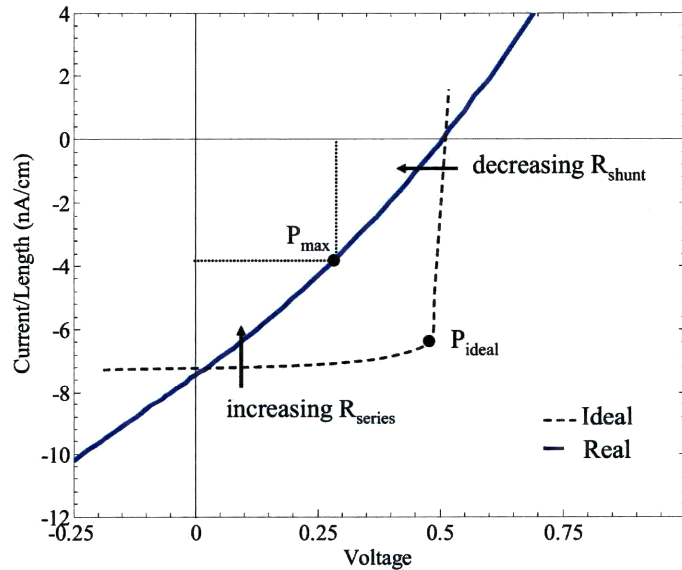

Fig. 5.5. Current-voltage characteristic of ideal diode and real diode device under illumination. The effects of series and shunt resistances are shown to decrease the fill-factor and the total attainable power output as a solar cell.

In this fiber, the short-circuit current is 7.4 nA/cm and $V_{o.c.}$ = 0.51 V. The maximum power point occurs at V_{max} = 0.27, I_{max} = -4.02 nA/cm where P_{max} = 1.08 nW/cm. The fill factor for this fiber device is thus 29%. The current, and maximum power output, that develops under illumination can be substantially limited by the series resistance of the device. But the magnitude of the limitation depends on the initial photocurrent. To illustrate this, figure 5.6 shows the relative efficiency of a hypothetical diode (having built-in voltage of 1 V, I_0 = 2 nA, $R_{shunt} = \infty$) as a function of series resistance for different levels of photogenerated current. The magnitude of this current may be due to either the surface area of the diode, different quantum efficiencies, photon intensity, etc.

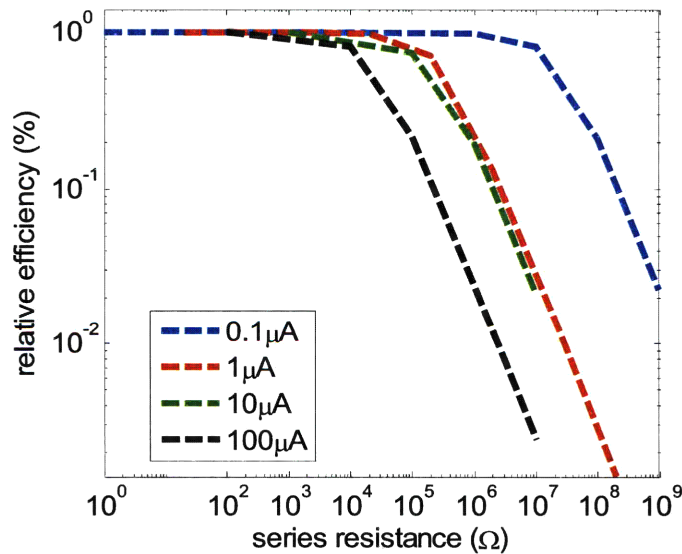

Fig. 5.6. Relative efficiency for a hypothetical diode as a function of series resistance for 4 different short-circuit currents. The efficiency can be seen to drop off precipitately when $R_{series} > V_{bi} / I_{s.c.}$.

Given the dramatic decrease in efficiency observed for large series resistances seen in figure 5.6 and the suggestion of some effect of the series resistance in the fill

factor of the fiber diode (figure 5.5), it makes sense to estimate the maximum photocurrent created by the device structure and compare with the fiber series resistance. Over the fabrication of many fibers having different electrode spacings, the series resistance of the fiber device under illumination has varied from 100kΩ to >10 MΩ. The short-circuit current in of these devices is typically between 5 and 10 nA/cm, essentially independent of series resistance. This suggests that the observed short-circuit current is determined by the device geometry and not limited by the series resistance. Indeed, the lateral device geometry limits the active area of the diode to one diffusion length from the junction depletion region rather than the entire distance between the electrodes. As the diffusion length in typical polycrystalline selenium device is on the order of one micron or less[4,5] the power conversion efficiency is estimated to be around 0.01% because the optical power in the AM1.5G simulated solar is 100mW/cm^2 or 10μA/cm (for a 1μm width).

Although the built-in voltage, determined by capacitance-voltage measurements, is equal to approximately 0.8 V, the open-circuit voltage that develops under illumination is typically only ~0.5 V (the maximum observed $V_{o.c.}$ = 0.57 V). There are many loss mechanisms that can reduce the open circuit voltage. Dark current shunting is one of them. Consider the case where the semiconductor absorption length is less than the total film thickness as depicted schematically in figure 5.7. An intrinsic attribute of the lateral device design such as in the fiber diode is that the distance between electrodes may be much larger than the diffusion length of photogenerated carriers. Thus despite complete illumination of the device, the actual width (*x*-direction) of the absorption area that contributes to the photocurrent is limited by the carrier diffusion length. Furthermore,

significant dark current flows opposite the photocurrent when the film thickness (y-direction) is greater than the distance photons travel in the semiconductor, i.e. the absorption length.

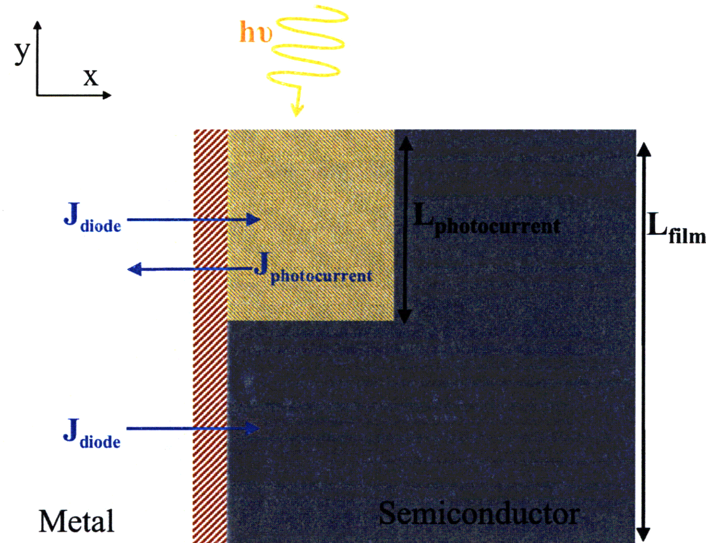

Fig. 5.7. Schematic diagram of metal semiconductor junction. Although the device may be uniformly illuminated, the photocurrent generating area (yellow hatched area) is defined by the absorption length of photons in the semiconductor (y-direction) and the diffusion length carriers may travel before recombination (x-direction). The red-hatched area represents the active junction area.

We can describe this situation mathematically (neglecting the shunt resistance):

$$I_{total} = JL_{film} = J_o L_{film} \exp\left\{\frac{qV - JL_{film}R_{series}}{nkT}\right\} - J_{s.c.}L_{photocurrent}, \quad (5.18)$$

where J represents a linear current density, and L is the particular length scale of interest. Typical film thicknesss, L_{film}, are 3-5 μm. The absorption depth of light into selenium can be estimated from the Beer-Lambert law and the complex component of the semiconductor's index of refraction,

$$I = I_o \exp\left(\frac{-4\pi k}{\lambda} y\right). \quad (5.19)$$

Crystalline selenium has a hexagonal structure and is optically birefringent. For λ=532 nm the refractive index is 4.28-1.21i and 2.93-0.61i, for the two principle axes.[6] Assuming no preferred orientation to the fiber device polycrystalline selenium, we can estimate the *effective* complex component of the refractive index to be an average of the two axes, so $k = 0.91$. Thus the length of semiconductor necessary to absorb 95% of the incident light is approximately 150nm. Using this value for $L_{photocurrent}$, in equation 5.18, the change in open-circuit voltage for different film thicknesses can be calculated and is shown in figure 5.8, assuming an arbitrary built-in voltage of 0.9 V. The figure clearly shows that the V_{oc} can be markedly reduced by the flow of dark current through the device. Given that the semiconductor film in fiber is typically 3-5 μm at the metal-semiconductor interface, this shunting could explain a substantial proportion of the discrepancy between the C-V measured built-in voltage and the I-V measured open-circuit voltage.

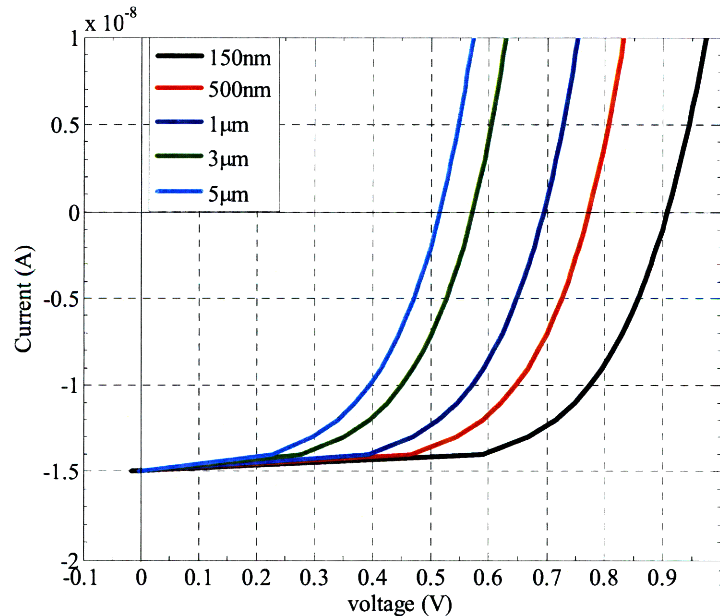

Fig. 5.8. Current-voltage characteristics for device having different film thicknesses less than or equal to the absorption length of photons incident on semiconductor.

The fact that the I-V and C-V characteristics suggest a one-sided device, i.e. a device composed of one ohmic and one blocking barrier, may seem counterintuitive because of the large work function difference between the semiconductor and metals. Selenium is known to be a p-type semiconductor with a work function of between 5.3 (found in chapter 3) and 5.9 eV.[6,7] While other elemental semiconductors such as silicon and germanium have surface states that lead to a weak relationship between metal semiconductor work function difference and barrier height, selenium shows a rather large dependence.[7,8] The work function of the $Sn_{85}Zn_{15}$ and $Sn_{74}Pb_{26}$ were measured to be 3.9 eV and 4.2 and 4.2 and 4.5 by ultraviolet photoemission spectroscopy (UPS) and scanning Kelvin probe in chapter 2.[9] Given the 1 to 2 eV difference in work functions between both metals and the semiconductor, it seems especially surprising that each metal-semiconductor junction behave differently. Because selenium is a p-type semiconductor the polarity of the I-V and C-V measurements imply that the $Sn_{74}Pb_{26}$ / $Se_{97}S_3$ junction behaves ohmically while the $Se_{97}S_3$ / $Sn_{85}Zn_{15}$ interface forms the blocking barrier. Furthermore, similar devices were fabricated with several other metal electrodes, but only fibers containing $Sn_{85}Zn_{15}$ showed rectification (see chapter 4). Greater understanding into the origin of the electronic behavior of these junctions may be gained by direct examination of the composition and potential variation across the metal-semiconductor interfaces.

5.3 Band-diagram construction

5.3.1 Background

The spatial variation in surface potential may be directly measured by Kelvin probe force microscopy (KPFM) and compared with compositional measurements performed by energy dispersive spectroscopy (EDS). KPFM is a non-contact atomic force microscope (AFM) based technique that enables the simultaneous measurement of both topography and surface potential. Non-contact AFM, as in all AFM techniques monitors the change in force between tip and sample based on Hooke's law of spring force, $\Delta f = k\Delta z$, where Δz is the tip displacement, and k is the spring constant of the cantilever. The AFM tip is oscillated above the sample surface at a specific frequency close to the resonance. Forces induced by changes in topography cause shifts in the oscillating frequency. Software adjusts the tip to sample spacing to return the oscillation to the original frequency and constructs maps of the surface based on the magnitude of the tip change. KPFM takes the addition step of applying an oscillating voltage between a conductive cantilever and the sample. As the conductive AFM tip vibrates above the sample surface, a force is generated by the variable capacitance arising from the work function difference between tip and sample (the contact potential difference, CPD) and the oscillating tip-to-sample spacing. An electronic circuit monitors this force on the tip and applies a bias to minimize it. The voltage at which the force is minimized is equal to the CPD.

More rigorously, the electrostatic force between the AFM cantilever and the sample can be written as

$$F_{es} = -\frac{1}{2}\frac{\partial C}{\partial Z}U^2, (5.20)$$

where U is the potential between the tip and sample. This potential intrinsically contains the contact potential and may also include additional, externally applied dc and ac potentials, U_{dc} and U_{ac}, respectively. Thus U can be written as

$$U = U_{dc} + U_{ac}\sin(\omega_2 t) - \frac{\Delta\Phi_{cpd}}{q} \quad (5.21)$$

where ω_2 is the frequency of the voltage oscillation. Substituting (5.21) into (5.20) and using the double angle identity

$$\cos(2u) = 1 - 2\sin^2(u) \quad (5.22)$$

the total force between tip and sample is the sum of three components

$$F_{es}(dc) = -\frac{\partial C}{\partial Z}\left\{\frac{1}{2}\left(U_{DC} - \frac{\Delta\Phi}{q}\right)^2 + \frac{U_{AC}{}^2}{4}\right\} \quad (5.23)$$

$$F_{es}(\omega_2) = -\frac{\partial C}{\partial Z}\left\{\left(U_{DC} - \frac{\Delta\Phi}{q}\right)U_{AC}\sin(\omega_2 t)\right\} \quad (5.24)$$

$$F_{es}(2\omega_2) = +\frac{\partial C}{\partial Z}\frac{U_{AC}{}^2}{4}\cos(2\omega_2 t) \quad (5.25)$$

Equation 5.23 shows that the force is minimized when the applied U_{DC} equals the difference in tip and sample work function, $\Delta\Phi$. Another AFM technique called scanning capacitance microscopy makes use of equation 5.25. Using this equation it is seen that the force at $2\omega_2$ is proportional to the local capacitance gradient.

KPFM may be run in the so-called amplitude-modulation (AM) and force-modulation modes (FM). The force gradient, $\partial F / \partial Z$, is detected in FM-KPFM modes. The FM-KPFM modulation frequency is typically run a few kHz above the cantilever resonance frequency, the frequency at which topography data is collected, to avoid cross-talk between measurements as they both utilize the gradient in force to collect

information. Typical modulation amplitudes, U_{AC}, are on the order of 1-2 V peak-to-peak. This method is highly sensitive to spatial variations in the contact potential because the force gradient is being measured. However, the large modulation amplitude can induce band-bending in semiconductors and other materials with low carrier concentrations. The actual force between tip and sample is detected and minimized by an external regulator in AM-KPFM. The frequency the KP modulation is typically performed at the first overtone of the cantilever's natural resonance ($\omega_2 \sim 6.27\ \omega_{resonance}$) in order to maximize the signal to noise ratio. The typical amplitude is on the order of 100-200 mV peak-to-peak. Because the modulation amplitude is much smaller and the frequency of modulation is much higher than in FM-KPFM, amplitude-modulation mode is significantly less likely to cause local changes in the electronic structure of the sample being measured and spurious results.[10,11,12]

Kelvin probe techniques are very sensitive to minor environmental changes, and sufficient precautions must be made to ensure that the sample surface is prepared properly. For best results, these measurements should be done in ultrahigh vacuum (UHV) conditions on clean surfaces, as the work function is a surface property and highly sensitive to such as oxides and adsorbates. Surfaces may be prepared by in-situ cleaving or ion-sputtering. The researcher must be aware of how the surface is affected by both these techniques. Ion sputtering generates fresh surface but also induces roughness, anisotropic surfaces, and dangling bonds, each of which may also cause changes in the local work function. The existence of dangling or unsaturated bonds is especially important for semiconductors as the density of surface states can shift the Fermi level and apparent work function considerably. Often the surface is cleaned by undertaking several

"sputter-anneal" cycles in which the surface is sputtered and then thermally annealed to remove as much ion-induced damage as possible. Care must be taken that the annealing temperature does not cause sublimation of the sample or melting. In fact, it is not prudent to anneal the fiber samples under high vacuum because the sublimation temperatures of selenium, zinc, and lead are low. Sample cleaving may be performed when possible. This method ensures that fresh surface is generated and is free of defects induced by sputtering. It must be noted, however, that dangling bonds will nearly always exist at a material surface.

Because the technique is so sensitive to only the topmost surface, quantitative KPFM measurements can only be performed in ultra high vacuum conditions. Even though fresh surface may be prepared for measurement, gas molecules will quickly begin to adsorb to the surface and alter the contact potential. The time it takes for a complete monolayer to form can be estimated, and this is often used as a measure of how low the system pressure must be in order to maintain a clean surface throughout an experiment. The flux of gas particles (molecules per cm^2 per second) incident on a surface is given by[13]

$$f = \frac{p}{\sqrt{2\pi mkT}} \quad (5.26)$$

where p is the pressure, k is the Boltzmann constant, and m is the mass of the molecule. The number of adsorbed particles per unit area, N, as a function of time, t, can be written as

$$N = ftS \quad (5.27)$$

where S is the sticking coefficient, or the probability that a molecule will stick to the surface and not bounce off during a collision. Assuming an average lattice constant of

about 5 Å, there are about 10^{15} atoms/cm^2 and a gas particle can adsorb or react at each lattice, the number of monolayers that form as function of time is

$$N_{mono} = 10^{-6} ptS \quad (5.28)$$

where pressure is in torr and time is in seconds. Thus for a sticking coefficient equal to one, a single monolayer will form in one second at a pressure of 10^{-6}. In practice, of course, an experiment takes much longer than a second to complete and any measurements done at this pressure would reflect the contact potential difference between the tip and adsorbed layers. However, the time to form a monolayer increases to tens or hundreds of minutes when the pressure is reduced to between 10^{-9} and 10^{-10} torr, and measurements on the actual sample surface can be performed.

One must also note that Kelvin probe techniques only measure the difference in tip and sample work functions. In order to determine the actual work function of the sample, the tip work function must be determined by calibration to a known work function surface (such as clean gold). The AFM tip must be cleaned of adsorbates and contamination by heating under vacuum if the tip work function is to be truly known.

KPFM can be combined with other techniques to create an even deeper understanding of sample surfaces. Energy dispersive spectroscopy (EDS) is a semi-quantitative technique for mapping the composition of specimens with scanning electron microscopy. In electron microscopy, high energy electrons (typically 4-10 keV) are focused into a small beam and rastered across the specimen to be imaged. The interaction between the electron beam and the sample generates a variety emitted radiation, and suitable detectors collect the intensity of each type of radiation. Most commonly, images of the surface exhibiting both compositional and topographical

contrast are created by collecting electrons nearly elastically scattered (so called back-scattered) or sample electrons excited and ejected by the incident beam (secondary electrons). One type of inelastic scattering event that also occurs is the excitation of core electrons within the sample and their subsequent relaxation and emission of x-rays. The energy of the emitted photons is characteristic to the atom and even the atomic transition between energy levels and thus can be used to identify the atom. EDS systems with x-ray detectors and analysis software are readily available and can be easily integrated into standard SEMs. With this technique qualitative, if not quantitative, chemical composition maps can be created at the same time samples are imaged.

5.3.2 Experimental

Short sections of device fiber were mounted in epoxy and then cut into 1 mm thick slices with a diamond wire saw. The final surface was prepared by ion polishing with a JEOL cross-section polisher. EDS measurements were performed with a Thermoelectron Corp. Noran system SIX attached to a JEOL 6700 Field Emission SEM. KPFM measurements were performed with Omicron VT-AFM equipped with a Kevin Probe control unit using a nanosensors Pt-Ir coated conductive tip (nominal resonance ~75 kHz). Kelvin signal was run at the first overtone of cantilever resonance with an applied peak-to-peak voltage of 200mV. The tip work function was calculated by determining the CPD between the tip and a clean polycrystalline gold surface, and the sample work function was calculated by the relation, $\Phi_{tip} - \Phi_{sample} = CPD$. Samples were cleaned in-situ by argon-ion sputtering. Image analysis was performed with SPIP and Gwyddion.

5.3.3 Results and Discussion

Figure 5.9 presents the results of KPFM measurements (a-c) along with EDS linescans of a similar junctions (d) for the $Sn_{74}Pb_{26}$ / $Se_{97}S_3$ junction. Topography (a) and work function maps (b) are shown as well as representative line scans (c). A sharp change in both topography and work function can be seen at the $Sn_{74}Pb_{26}$ / $Se_{97}S_3$ metallurgical interface. The change in topography is due to relative difference in sputter rates of the metal and semiconductor. The KPFM map and line scan shows the entire potential change occurs over a 400 nm region at the interface. Simultaneously a small increase in concentration of lead at the interface is revealed by EDS.

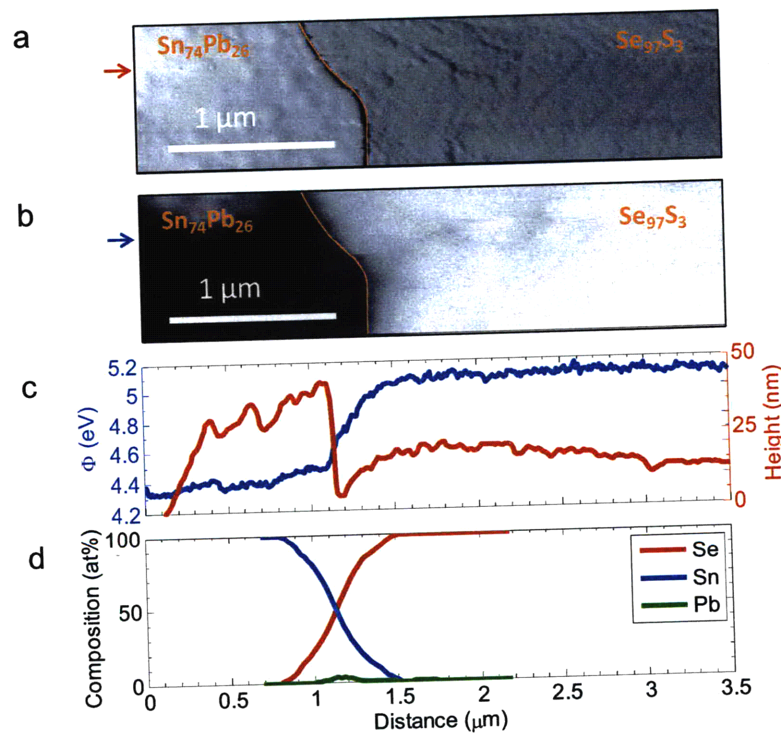

Fig. 5.9. Surface potential and chemical composition of $Sn_{74}Pb_{26}$ / $Se_{97}S_3$ junction. KPFM-measured topography and work function maps are shown in (a) and (b), respectively (scale bars equal 1 µm). Orange lines highlight metallurgical interface between metal and semiconductor. Blue and red arrows correspond to location of linescans in (c). EDS line scans show variation in composition across the metallurgical junction in (d).

Figure 5.10 shows the results of KPFM and EDS measurements on the $Se_{97}S_3$ / $Sn_{85}Zn_{15}$ interface. The spatial variation in work function can be seen to extend over 1.5 μm beginning with an abrupt change in contact potential at the 2.5 μm mark and then a more gradual change into the semiconductor. The topography map, however, reveals the metallurgical $Se_{97}S_3$ / $Sn_{85}Zn_{15}$ junction occurs roughly at the 1.1 μm mark. EDS line scans show a large increase in zinc concentration at the metallurgical interface.

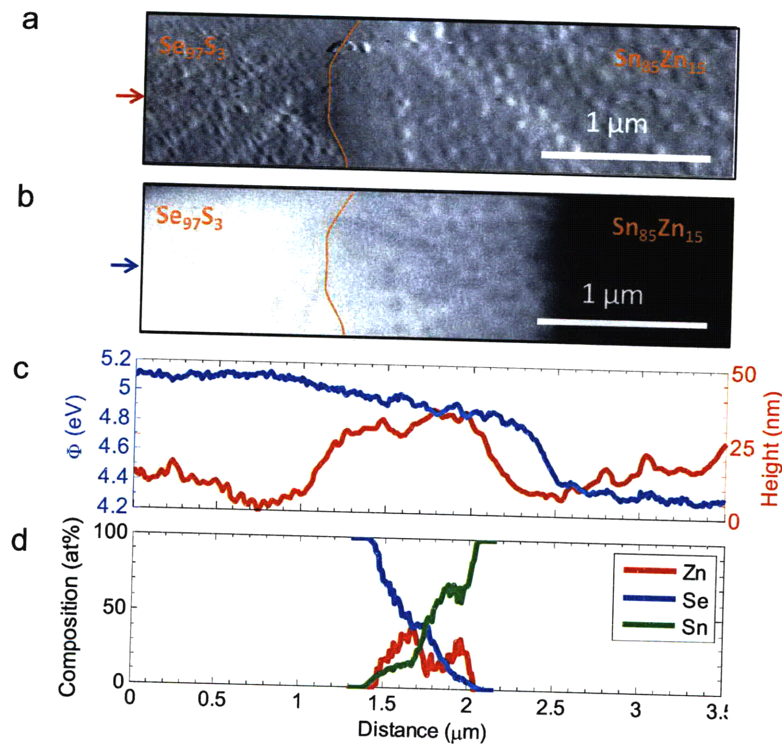

Fig. 5.10. Surface potential and chemical composition of $Se_{97}S_3$ / $Sn_{85}Zn_{15}$ junction. KPFM-measured topography and work function maps are shown in (a) and (b), respectively (scale bars equal 1 μm). Orange lines highlight metallurgical interface between metal and semiconductor. Blue and red arrows correspond to location of linescans in (c). EDS line scans show variation in composition across the metallurgical junction in (d).

The combination of the EDS and KPFM data suggest that electronic behavior of the interfaces is guided by mixing and/or compound formation of the metal and semiconductor. The $Sn_{74}Pb_{26}$ / $Se_{97}S_3$ junction behaves ohmically despite the large

potential drop observed by KPFM. EDS demonstrates that this interface is not sharp, and the presence of lead may also be a contributing factor. By itself, lead would be expected to act as a p-type donor in selenium, increasing the carrier density at the interface, possibly enough to create an ohmic tunnel junction. But the formation of small amounts of PbSe, a small bandgap degenerate semiconductor, may also occur. Indeed, ohmic contacts to large bandgap semiconductors are often made by introducing a small bandgap material between the metal and semiconductor.[1] The $Se_{97}S_3$ / $Sn_{85}Zn_{15}$ interface is more interesting. Even though the region in figure 2 between 1.1 and 2.5 μm appears as though it has the same topography as the metal, it must be composed of semiconductor because the band bending clearly visible in the KPFM map cannot occur in high carrier density metals. There are also two distinct regions of potential variation at the interface, as seen in the KPFM linescan. There exists an abrupt change in work function at the 2.5 μm mark followed by a more gradual change. This abrupt change may signify the existence of a large number of interface states that could be expected from the non-lattice matched interface. These states may also account for the observed capacitance dispersion as well as the difference between the capacitance-measured built-in voltage and one that may be expected by difference in semiconductor and metal work function. The EDS measurements reveal the large change in zinc composition at the interface, suggesting that this compound may be zinc selenide based. Indeed, although $SnSe_2$ is another semiconductor that may form in the presence of a liquid mixture of Se, Sn, and Zn. The material's small bandgap (E_g = 1.0 eV) and similar ionization potential (I.P. = 6.2 eV)[14] to selenium (5.9-6.1 eV)[7,15] means that magnitude of the observed open-circuit voltage and built-in potential could not be explained by the presence of $SnSe_2$. Furthermore, there

was no indication of compound formation at the $Sn_{74}Pb_{26}$ / $Se_{97}S_3$ even though $SnSe_2$ would be just as likely to form at either interface. A large bandgap semiconductor such as zinc selenide (Eg = 2.7 eV, I.P. = 6.8 eV)[16] would however form a barrier to hole conduction and explain the rectifying behavior. The formation of such a compound in the fiber is notable because it means that many more materials can be built into fibers than previously thought. Zinc selenide, for example, is finding more use in optical and electronic devices[17] but melts at 1530 °C and thus would never have been considered as a suitable material for thermal drawing at low temperatures. Expanding the number and types of materials that may be incorporated into multimaterial fibers will lead to even more types of junctions and device functions. One must simply identify compounds that may be fluid processed together that could be converted to others.

A preliminary band diagram of the $Se_{97}S_3$ / ZnSe / $Sn_{85}Zn_{15}$ structure can be constructed by combining knowledge of the semiconductors' bandgap and electron affinities with the observed change in contact potential. The discontinuity in valence and conduction bands is determined from the standard equations for heterostructures based on Anderson's model[1,18]

$$\Delta E_c = q\Delta\chi \quad (5.29)$$

$$\Delta E_c + \Delta E_v = \Delta E_g \quad (5.30)$$

and the band bending can be inferred from the spatial variation in contact potential. The proposed band diagram is given in figure 5.11 and clearly indicates how the large discontinuity in the valence band at the $Se_{97}S_3$ / ZnSe interface would create a barrier to hole flow. A large density of interface states is expected (dashed lines) at both interfaces due to the large differences in lattice constant (a_{Sn} = 5.83 Å, c_{Sn} = 3.19 Å a_{Se}= 4.36 Å, c_{Se}

= 4.95 Å, a_{ZnSe} = 5.67 Å)[6] between the materials and the observed dispersion in capacitance measurements at different frequencies.

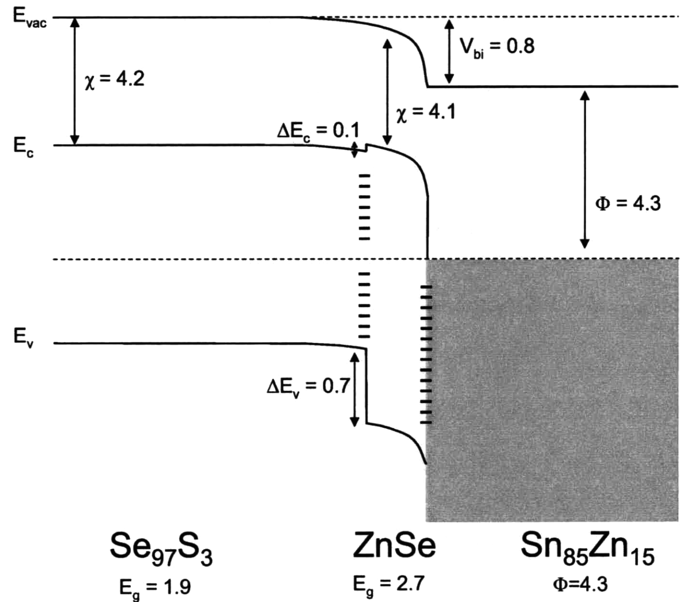

Fig. 5.11. Band diagram constructed with from KPFM and EDS measurements. ZnSe forms a barrier to hole injection from the semiconductor to the metal.

5.4 Photodiode Characterization

One of the largest uses of semiconductor devices is for their ability to convert optical signals into electronic ones. It thus makes sense to characterize the performance of these new fiber integrated diodes as photodetectors. In this section the most common methods of measuring photodiode performance will be defined and then these metrics will be measured for the newly developed fiber integrated diodes.

5.4.1 Background

Perhaps the simplest metric for characterizing a photodetector's performance is the external quantum efficiency (or simply the quantum efficiency). This is defined as the number of electrons collected at the electrodes for every photon incident on the device.

$$\eta_{EQE} = \frac{I_{ph}}{q\Phi} = \frac{I_{ph}}{q}\left(\frac{h\nu}{P_{opt}}\right). \quad (5.31)$$

The efficiency may be further broken into other efficiencies, such as the absorption efficiency, carrier excitation, and carrier collection efficiencies. The internal quantum efficiency is defined as the number electrons collected per photon that is actually absorbed by the device and is related to the external quantum efficiency by the amount of light reflected off the device structure (R is the reflectivity coefficient), assuming complete absorption by the semiconductor.

$$\eta_{EQE} = (1 - R)\eta_{IQE}. \quad (5.32)$$

The responsivity, $\Re$, defined as the number of amperes of current per incident watt of optical power is another common metric

$$\Re = \frac{I_{ph}}{P_{opt}} = \frac{\eta_{EQE}q}{h\nu}. \quad (5.33)$$

Generally researchers are interested increasing the sensitivity of the detectors so that the smallest possible optical signal is detected. One important metric is the noise-equivalent-power (NEP, expressed in W-Hz$^{0.5}$), or how much optical power is necessary to create a signal that is above the noise level of the detector at a 1 Hz bandwidth. Noise can be due to a number of sources.[19] Two common sources are due to scattering and generation and recombination events. Noise due to random scattering arising from thermal fluctuations,

$$i^2_{thermal} = \frac{4kT\,\Delta\upsilon}{\Omega} \quad (5.34)$$

where T is the temperature, $\Delta\upsilon$ is the bandwidth (typically taken to be 1), and Ω is the resistance. Random changes in the number of carriers due to generation and recombination processes will also cause current fluctuations[19]

$$i_{G-R}^2 = 2qI\Delta\upsilon = 2qI_{sat}\left(1+\exp\left(\frac{qV}{kT}\right)\right)\Delta\upsilon . \quad (5.35)$$

The current flowing through the device can be written simply as I or in the case of a photodiode can be substituted with the reverse saturation current, I_{sat}, multiplied by an additional factor corresponding to the applied voltage. It can be seen from equation 5.35 that a reversed biased diode ($V < 0$) is desired for reducing the current and total noise in the system. This is because recombination fluctuations are reduced as randomly generated carriers are immediately swept out of the junction by the bias. Assuming that the total noise is limited by the generation-recombination noise, and normalizing by a bandwidth of 1 Hz, the NEP (W-Hz$^{1/2}$) can be written as

$$NEP = \frac{\sqrt{2qI}}{\Re} . \quad (5.36)$$

The detectivity of the diode (D*, expressed in units of cmHz$^{0.5}$W^{-1}) is another measure of sensitivity in which the NEP is normalized by the bandwidth and device area so that this metric is entirely independent of testing conditions

$$D^* = \frac{\sqrt{A\Delta\nu}}{NEP} . \quad (5.37)$$

5.4.2 Experimental

The performance of the fiber devices fabricated in chapter four was measured in the following ways. The responsivity of the fiber device at 530 nm was measured when under -2 V reverse bias by measuring the change in photocurrent as the optical power is

varied. The responsivity as a function of wavelength was determined by measuring the photocurrent at each wavelength of light from a broadband lamp passing through a monochromator and chopped at 40 Hz. This photocurrent was then normalized by the response of a known silicon photodetector in the same regime as well as the calculated responsivity at 530 nm. The frequency response at 530 nm was measured by modulating the amplitude of a LED light source with a square wave and measuring the difference in photocurrent between the high and low states with an oscilloscope.

5.4.3 Results and Discussion

As might be expected, the responsivity of the fiber device was found to increase with applied bias (in both the forward and reverse directions) due to increased electric field within the device. For an applied 2 V reverse bias, the responsivity and external quantum efficiency were found to be 8.6 mA/W and 2%, respectively. The NEP was calculated from the responsivity and the measured dark current and found to be 4.7 pW $Hz^{-1/2}$. The responsivity as a function of wavelength is shown in figure 5.12. A maximum in the responsivity is seen at 450 nm. The observed decrease in responsivity at shorter wavelengths is due to the shorter penetration depth of higher energy photons and an increase in density of trap states and recombination centers at the polymer semiconductor interface.[20] The low energy (high wavelength) cut-off occurs at a wavelength of about 650 nm, corresponding to the bandgap of selenium of ~ 1.9 eV.

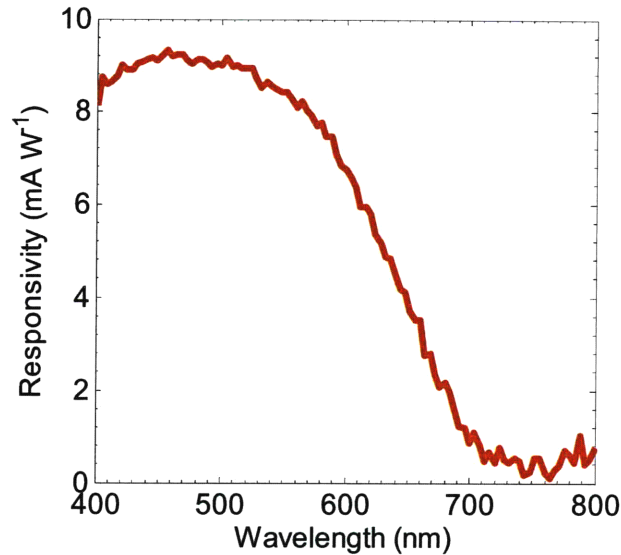

Fig. 5.12. Responsivity variation with wavelength for fiber diode biased at -2 V.

The frequency response of the fiber diode under -2 V bias is given in figure 5.13. An abrupt decrease in photoresponse occurs at 1 kHz. This is the so-called 3 dB frequency where the photoresponse will decrease by a factor of two from the initial value and begins to roll off at a rate of 20 dB per decade, i.e. for an increase in frequency by a factor of 10, the amplitude of the signal decreases by a factor of 10. This sets a practical limit on how fast the device can be modulated. Taking the device area into account and setting the bandwidth to 1 kHz, the detectivity is found to be 5.6×10^{11} , better than the best amorphous thin-film photodetectors even though the dark current is much higher in the diode device.

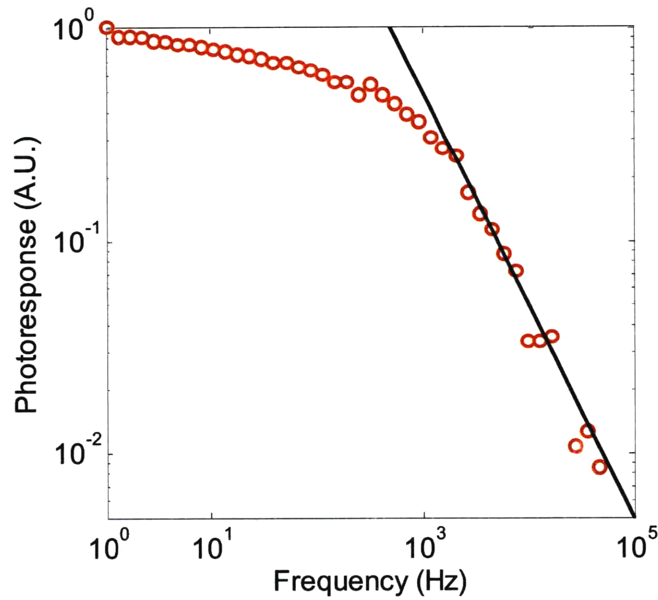

Fig. 5.13. Frequency response of fiber diode at 530 nm and under reverse bias.

5.5 Conclusions

In this chapter, the electrical properties of the new multimaterial rectifying device fibers were measured. Using a combination of standard electrical characterization techniques (including I-V and C-V measurements) as well as EDS compositional analysis and Kelvin probe force microscopy, an electronic band diagram was constructed that clearly shows how the formation of a ZnSe based compound at the $Se_{97}S_3$ / $Sn_{85}Zn_{15}$ interface can act as a barrier to carrier flow and form the basis of the rectifying behavior. Identification and characterization of this compound formation is a major achievement of this thesis and in multimaterial fiber processing in general because it shows that many more materials can be incorporated into the fibers than previously thought and should lead to the ability to create significantly more complex devices and structures in the future.

The diode fiber was also characterized as a photodetector. The external quantum efficiency was found to be about 2%, and the responsivity was found to be acceptable. The noise equivalent power, detectivity, and frequency response were also measured at 530 nm and show that the performance of this new rectifying device fiber is at least as good as all other previous fiber devices even though the series resistance is significantly lower (and hence the dark noise is much larger).

5.6 References

1. Sze, S. & Ng, K. *Physics of Semiconductor Devices*. 3rd edn, (Wiley-Interscience, 2006).

2. Ramanathan, S., McIntyre, P. C., Guha, S. & Gusev, E. Charge trapping studies on ultrathin ZrO_2 and HfO_2 high-k dielectrics grown by room temperature ultraviolet ozone oxidation. *Applied Physics Letters* **84**, 389-391 (2004).

3. Nelson, J. *The Physics of Solar Cells*. (Imperial College Press, 2004).

4. Champness, C. H., Shukri, Z. A. & Chan, C. H. Minority-Carrier Diffusion Length Determination from Capacitance Measurements in Se-CdO Photovoltaic Cells. *Canadian Journal of Physics* **69**, 538-542 (1991).

5. Champness, C. H. & Chan, C. H. Photocurrent Capacitance Method of Diffusion Length Measurement. *Solar Energy Materials and Solar Cells* **30**, 65-75 (1993).

6. Lide, D. R. *CRC Handbook of Chemistry and Physics*. Vol. 89 (CRC Press, 2008).

7. Champness, C. H. & Chan, A. Relation Between Barrier Height And Work Function in Contacts to Selenium. *Journal of Applied Physics* **57**, 4823-4825 (1985).

8. Bube, R. *Photoconductivity of Solids*. (Wiley, 1960).

9. Orf, N., Baikie, I., Shapira, O. & Fink, Y. Work Function Engineering in Low Temperature Alloys. *Applied Physics Letters* (2009).

10. Sadewasser, S., Glatzel, T., Shikler, R., Rosenwaks, Y. & Lux-Steiner, M. C. Resolution of Kelvin probe force microscopy in ultrahigh vacuum: comparison of experiment and simulation. *Applied Surface Science* **210,** 32-36 (2003).

[11] Sadewasser, S., Glatzel, T., Rusu, M., Jager-Waldau, A. & Lux-Steiner, M. C. high-resolution work function imaging of single grains of semiconductor surfaces. *Applied Physics Letters* **80**, 2979-2981 (2002).

[12] Glatzel, T., Sadewasser, S. & Lux-Steiner, M. C. Amplitude or frequency modulation-detection in Kelvin probe force microscopy. *Applied Surface Science* **210,** 84-89 (2003).

[13] Kolansinski, K. *Surface Science: Foundations of catalysis and Nanoscience*. (John Wiley & Sons, 2002).

[14] Schlaf, R., Pettenkofer, C. & Jaegermann, W. Band lineup of a $SnS_2/SnSe_2/SnS_2$ semiconductor quantum well structure prepared by van der Waals epitaxy. *Journal of Applied Physics* **85**, 6550-6556 (1999).

[15] Williams, R. H. & Polanco, J. I. Electronic-Structure of Chalcogenide Solids - Photoemission Study of Ordered and Disordered Selenium and Tellurium. *Journal of Physics C-Solid State Physics* **7**, 2745-2759 (1974).

[16] Chiang, T. C. & Himpsel, F. J. in *Electronic Structure of Solids: Photoemission Spectra and Related Data* Vol. 23a *Landolt-Bornstein Group III* eds A Goldmann & E.E Koch) Ch. 2.1, 81-84 (Springer Verlang, 2006).

[17] Kale, R. B. & Lokhande, C. D. Room temperature deposition of ZnSe thin films by successive ionic layer adsorption and reaction (SILAR) method. *Materials Research Bulletin* **39**, 1829-1839 (2004).

[18] Milnes, A. G. & Feucht, D. L. *Heterojunctions and Metal-Semiconductor Junctions*. (Academic Press, 1972).

[19] Rosencher, E. & Vinter, B. *Optoelectronics*. (Cambridge University Press, 2002).

[20] Sorin, F. *et al.* Multimaterial photodetecting fibers: a geometric and structural study. *Advanced Materials* **19**, 3872 (2007).

Chapter 6. Suggested Future Work and Conclusions

6.1 Introduction

It is expected that the work described in this thesis will form a strong foundation for future development of optoelectronic device fibers. This chapter will suggest areas of future work to improve the performance of the diode fiber and device fibers in general by both improving on the materials currently used as well as introducing new materials into the fibers. On the device level, examples of how the diodes can be combined into simple circuits will be given to motivate both the development of increasingly complex circuits and how the fabrication techniques developed in this work are making it possible to incorporate new types of devices into the fiber. Finally, the principle results of this work will be summarized.

6.2 Materials considerations

Significant effort should be expended in better understanding the origin of the trap states that control the capacitance behavior and how they can be reduced. Some of these states are expected to be inherent to the structure due to the large difference in lattice constant between the $Se_{97}S_3$ and ZnSe semiconductors and $Sn_{85}Zn_{15}$ metal, but others may be due to the trap states within the semiconductors themselves due to inadvertent dopants or grain boundaries. Simple C-V profiling as described in chapter 5 can give some idea into the density of carriers but the presence of trap states within the bulk semiconductor as well as at the interface can severely complicate interpretation of the results. Several capacitance techniques have been developed over time to study the nature of these defect states including admittance spectroscopy,[1] drive-level capacitance profiling (DLCP),[2] and deep-level transient spectroscopy (DLTS)[3]. In

admittance spectroscopy the capacitance of a junction is measured at various temperatures and frequencies. At low temperatures or high frequencies trap states become "frozen" and either there is not enough thermal energy or time for carriers to be emitted from traps. DLCP is a powerful and straightforward measurement technique that is sensitive to only bulk states within the semiconductor, allowing one to begin to separate the effects of interface and bulk states. DLTS measures transients in capacitance as a junction is modulated in and out of equilibrium. The method gives a wealth of information but is more difficult to implement in practice. Work should be undertaken through a series of these techniques to understand the location and origin of the defect states in the fiber device and whether or not they can be reduced.

Another potential source of reduced device performance could be related to discontinuities in the selenium film. In practice, there are a large number of open circuits in the $Sn_{74}Pb_{26}$ / $Se_{97}S_3$ / $Sn_{85}Zn_{15}$ devices, and the yield of functioning fiber diodes is quite low. This is believed to be substantially due to the low material viscosity during drawing, which allows the semiconductor film to "dewet" and pull away from metal interfaces. It is believed that even the fiber sections demonstrating electrical continuity between electrodes do not have uniform semiconductor films along their length. Thus the series resistance of the devices may be noticeably improved by increasing the semiconductor viscosity during drawing such that there is greater continuity between electrodes. Decreasing the molecular mobility of atoms in the semiconductor during drawing necessarily reduces their mobility during the lower temperature annealing step, and the post-drawing crystallization time will be expected to increase. An extreme example of this is seen in the original devitrification experiments with $As_{40}Se_{52}Te_8$, which required more than a week of annealing to induce the phase change. Identifying a semiconductor composition that exhibits some increased viscosity during drawing but still

retains the ability to be easily devitrified may be found without much effort. Germanium and arsenic function as cross-linkers within a selenium network and therefore increase the melt viscosity. The addition of germanium has been found to reduce the photocurrent efficiency, and thus is not recommended for inclusion. By testing a series of As-Se compositions, it is thought that a compromise composition may be found that increases melt viscosity enough to improve the yield and series resistance of fiber devices without sacrificing too much in terms of annealing time or any other electronic properties.

A large change in density during crystallization is a related consequence of the semiconductor's viscosity and phase changing nature. Indeed the density of selenium changes from 4.28 g cm^{-3} in the amorphous state to 4.79 g cm^{-3} when crystalline, suggesting the material undergoes a dramatic change in volume of more than 10% during phase transitions.[4] Such changes can introduce substantial stress in the system depending on the adhesion of the semiconductor to its boundaries. For example, simple calculation using COMSOL ® Multiphysics suggest that the induced stresses can reach 1 GPa if the boundary between metal and semiconductor is fixed. This value of stress is much larger than experimentally measured yield stress in amorphous selenium (~40 MPa)[5], and large-scale mechanical failure in the semiconductor might be expected. After extensive surveys of fiber cross-sections, this fracture is not observed. While mechanical failure after crystallization is not observed, the formation of large voids is. These voids are expected relieve the crystallization-induced stress by reducing the total volume of semiconductor and are expected to form easily because devitrification occurs at high temperatures compared to the glass transition, meaning that the atoms are able to easily rearrange into lower energy configurations. The formation of these voids is expected to have a similar impact on the device's electronic properties as the low drawing viscosity, whereby

reductions in electrical continuity increase series performance and voids at the $Se_{97}S_3$ / $Sn_{85}Zn_{15}$ interface especially impact performance by substantially reducing the active device area (i.e. the area less than a diffusion length away from the $Se_{97}S_3$ / $Sn_{85}Zn_{15}$ junction). Electronic defects due to changes in lattice and density are well known in the field of phase changing semiconductors and are the subject of much work. The most common method of reducing the stress or failure is to use adhesion layers already under stress, such as Ti.[6,7] Park et al have tried to limit the stress by controlling oxygen diffusion into the structure, as well.[8] These techniques may be useful in reducing the stress in the fiber devices. Changes in the typically annealing program should also be considered, as one may be able to identify a method of controlled void formation at locations away from the junction.

New materials may be incorporated into the fibers to either improve current diode performance or create new devices. The method of ZnSe compound formation in the fiber is not unlike the formation of silicides at silicon and metal interfaces that have revolutionized microelectronics[9] and suggests that many more materials can be built into these composite fibers than previously thought. Zinc selenide has many interesting optical and electronic properties[10] but melts at 1530 °C and thus would never have been considered as a suitable material for thermal drawing at low temperatures where only materials that melt in a narrow range of 200-300 °C have been previously considered. It is likely that other technologically relevant compound semiconductors such as CdSe, CdTe or In_2Se_3 may be incorporated into fibers with a similar method. These semiconductors in particular are used in photovoltaic cells because of their ideal absorption characteristics and electronic properties. One must only identify compounds that may be fluid processed together that could be converted to others. For example, the CdSe semiconductor may form when drawing the same $Se_{97}S_3$ semiconductor with a

cadmium-containing electrode such as the eutectic $Sn_{67.8}Cd_{32.2}$ (in wt%, T_m = 177 °C). The ionization potential (i.e. valence band maximum) and bandgap of CdSe are 6.62 and 1.75 eV, respectively.[11] Because $I.P._{CdSe} > I.P._{Se}$, this combination of materials may also form an interesting diode structure. Furthermore, because the bandgap of CdSe is almost 1 eV smaller than that of ZnSe, there may be a noticeable improvement in carrier conductivity as well as increased absorption area within the device. InSe may form when metallic indium is drawn with selenium, as well. It was found in chapter 4 that the combination of indium and selenium did not form a rectifying barrier like the $Se_{97}S_3$ / $Sn_{85}Zn_{15}$ pair, but this does not exclude the possibility of compound formation because the semiconductor bandgap and ionization potential must also be considered. The electron affinity and band gap of InSe is approximately 4.55 eV and 1.25, respectively,[12] and the difference in conduction and valence bands between InSe and Se would not be expected to form a barrier to carrier conduction in the same way as the $Se_{97}S_3$ / ZnSe heterojunction does.

In addition to identifying new compounds that may be formed by the semiconductor/ metal reaction, future work should focus on addressing other material needs in the fiber devices. Among the most needed of materials is a transparent, conductive polymer that can be used as a transparent electrode in photodetector fibers. The development of such a material would make it possible to create large area sandwich structures of semiconductor between the transparent polymer and the recently developed (and optically black) carbon-loaded polycarbonate. Such a structure would reduce dimensions between electrodes and significantly reduce the device series resistance. If this new material would be combined with a photodiode structure, it would enable the power output of the device to be substantially increased (by both reducing the series resistance and increasing the absorption area) perhaps enough to bring the fiber performance of

commercial viability. Conducting polymers are in fact used extensively in many organic optoelectronic devices. However little is known about their thermo-mechanical properties as they are generally processed only in the solution state. Just loading small graphitic particles into polycarbonate has been found to dramatically increase the composite conductivity without harming the polymer's thermal processing characteristics, it may be feasible to introduce transparent conductive particles into a polymer matrix. Semiconductors such as indium oxide, indium tin oxide, and zinc oxide have electronic bandgaps greater than 3 or 4 eV, so they are effectively transparent at visible wavelengths and made conductive by adjusting their composition or doping. Identifying a suitable solvent that both disperses nanoparticles of these oxides and dissolves the polymer should make it possible to cast a transparent conducting polymer with the thermal properties of the host polymer.

The incorporation of high aspect ratio carbon nanotubes into polymer matrices has also been found to result in composites with both transmissivity in the visible and high conductivity.[13,14] This is typically achieved by dispersing the nanotubes in a polymer solution through sonication, and care must be taken to identify the solvents that result in the greatest dispersion. This process may also be improved by treating the nanotubes with acids or bases to reduce aggregation.[15] It just so happens that the polymer matrix in these works were selected to be amorphous thermoplastics like polycarbonate and PMMA (polymethyl methyacrylate) that have already been drawn in multimaterial fibers. Thus it is expected that the incorporation into fibers should be relatively straightforward. One potential difficulty that may arise may be due to the fact that the drawing process is naturally orienting and may cause the randomly distributed nanotubes to align along the fiber length and lose electronic continuity in the radial direction.

6.3 Building new devices and circuits in multimaterial fibers

As part of the vision of developing optoelectronic device fibers is the ability to build complex circuits into fibers it makes sense to evaluate the potential use of these diode device fibers as circuit elements. The fiber design allows many diode devices to be built into a single cross-section, and these may be combined into different types of circuits. For example, by combining to diodes in parallel, the total short-circuit photocurrent of the system is then the sum of the individual photocurrents. This is clearly visible in figure 6.1 which displays the I-V characteristics of two separate diodes and when the two are strung in parallel under illumination. The short-circuit current is clearly increased by placing them in parallel, while the open-circuit voltage does not change. This effectively increases the total power output of the fiber and increases its utility as a solar cell. Note that the open-circuit voltage did not change in this case. This occurs when the diodes have the same $V_{o.c.}$ and are said to be matched. This is important because the open-circuit voltage of string of photodiodes in parallel will be equal to the lowest $V_{o.c.}$ of the system. When the diodes are strung in series it is the $V_{o.c.}$ that adds, and the current is limited by the highest resistance diode.

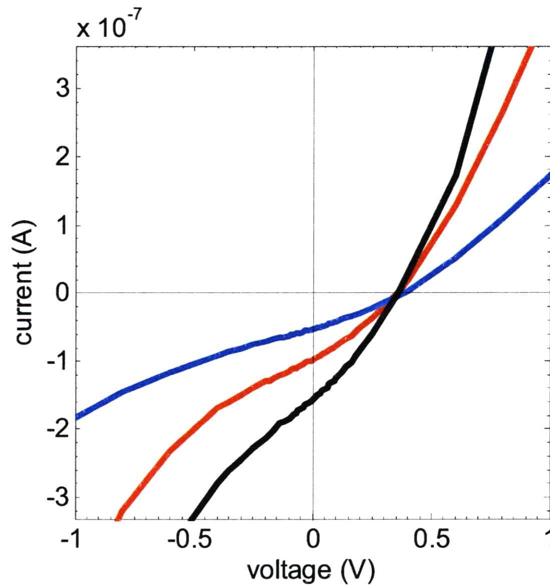

Fig. 6.1. Current-voltage characteristics under illumination for two separate diodes (red and blue) and then when the diodes are placed in parallel (black)

Diodes may also be placed back-to-back from each other in a configuration that is similar to a bipolar junction transistor (BJT). When in this configuration, they act as a constant current regulator over a small voltage range, as can be seen in figure 6.2. This design is not the same as a BJT because transistor amplification occurs when carriers from the emitter diffuse into the base and are swept into the collector junction. In this way the collector current is amplified by the application of voltage to the base (which biases the base-emitter junction). This does not occur in the back-to-back diode configuration because the 'base' in this configuration is the metal contact in which all carriers immediately recombine and do not diffuse to the other junction.

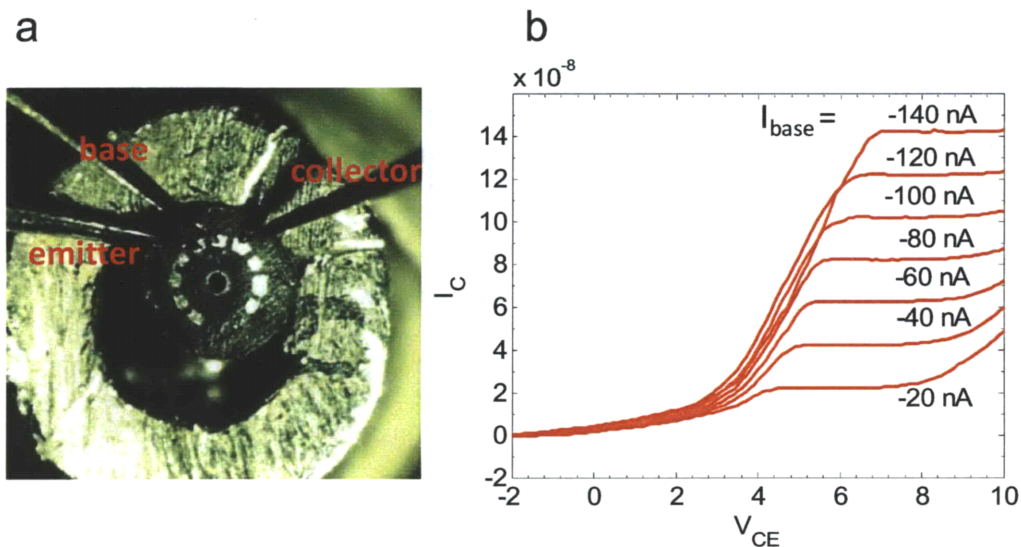

Fig. 6.2. Fiber diodes connected back-to-back demonstrating current regulating capabilities.

One common use of a diode is to rectify A/C oscillations. When a sinusoidal voltage (centered on zero) is applied, the current through a diode is expected to vary from large (forward biased) to small (reverse bias regime). The ability to rectify oscillations decreases with frequency as carrier's ability to respond to changes in voltage decrease with speed. Figure 6.3 shows the rectified signal (red) of an input sine wave (blue) at several frequencies. While the diode clearly functions as a rectifier at very low frequencies, the effect is clearly minimal for frequencies as low as 100 Hz. The figure is further confirmation of the long-lived trap discussed in chapter 5, and emphasizes how future work on the topic should focus on understanding the origin of these states and how their concentration can be reduced.

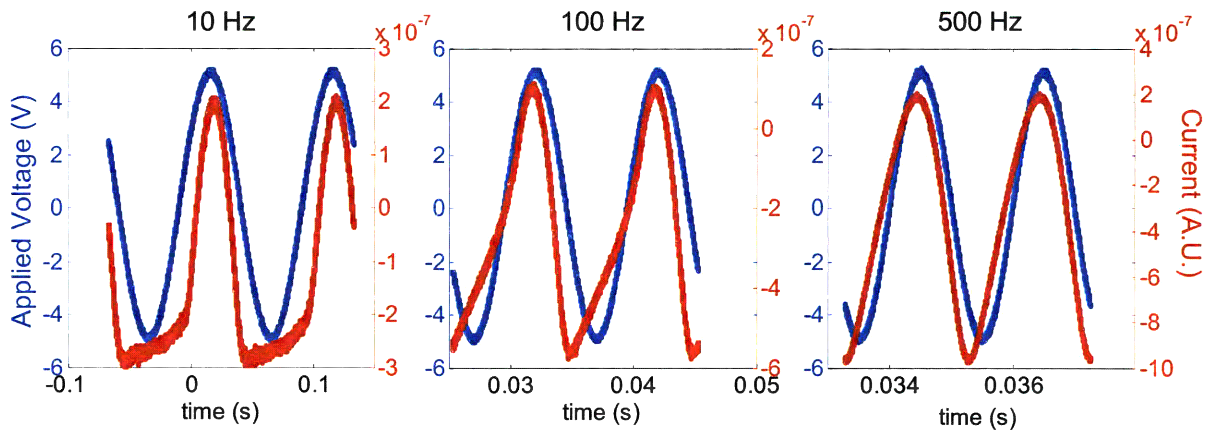

Fig. 6.3. Modulated current as a function of applied voltage for multimaterial diode fiber. In a normal diode the resistance in the forward and reverse directions are small and large, respectively, so that current essentially flows only when the voltage is applied in a specific direction.

In addition to combining devices into circuit, further work should focus on introducing new types of devices into the fiber. Metal-semiconductor-metal devices that function as simple resistors have already been developed. The two most common elements that are still missing are capacitors and inductors. It is thought that incorporating capacitors into fiber should be relatively straightforward as metals and insulators have been easily built into the fiber for quite some time. Creating fiber-integrated inductors may be less straightforward as it requires the longitudinal symmetry be broken to create a helical metal structure. Some initial work in this direction has been done. By building a motor-controlled rotating preform holder, the preform orientation may be changed during thermal drawing, breaking the z-axis symmetry of the fiber. Figure 6.4 shows a photograph of such a preform holder and photographs of several fibers having tin electrodes twisting around the core at different pitches. Not only may this new type of fiber fabrication lead to development of simple inductors, it creates the possibility of inducing magnetic fields inside of fibers for either particle guidance or modifying the optical properties of materials within the fiber. As_2Se_3, for example has a large Verdet coefficient, meaning that the

polarization of photons passing through the glass is highly susceptible to being rotated by the application of a magnetic field.

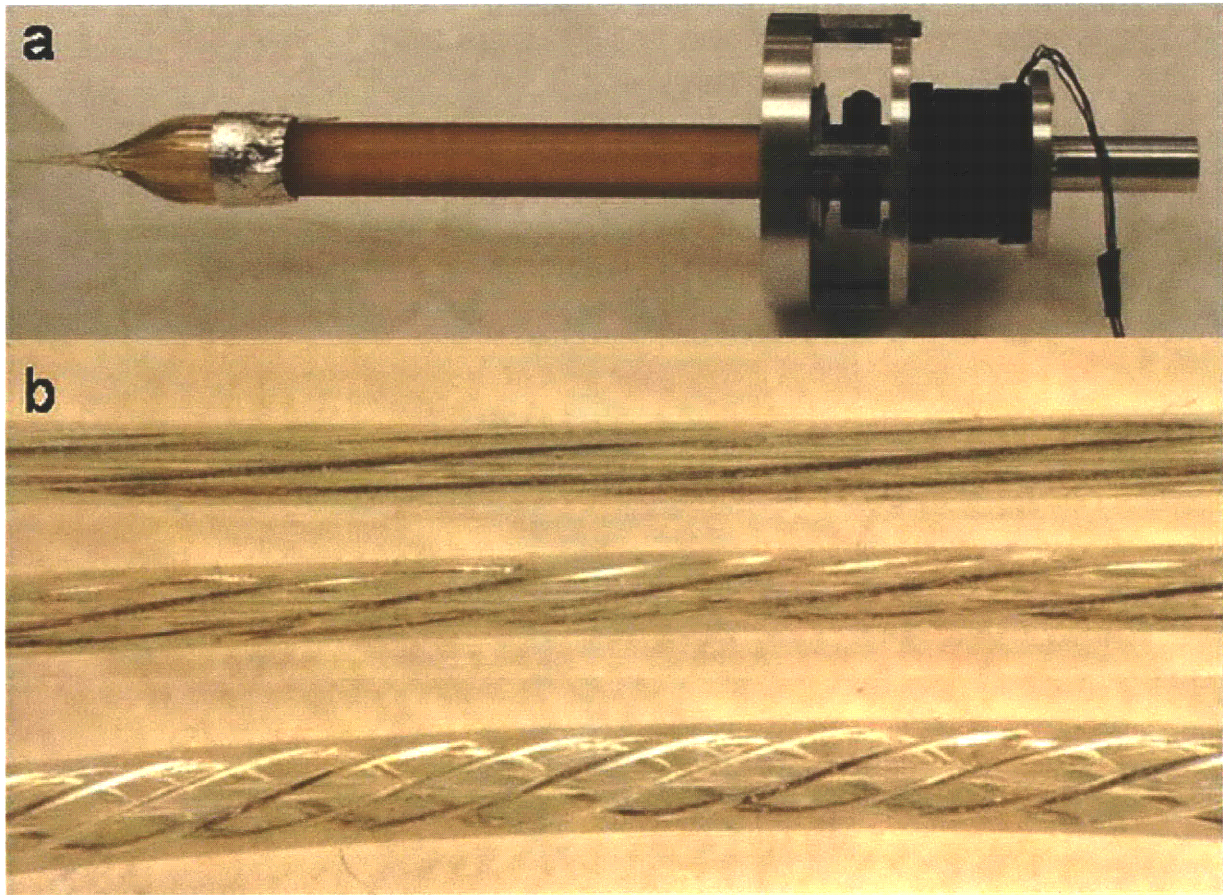

Fig. 6.4. (a) Photograph of rotating preform holder. A computer-controlled stepper motor rotates the preform during fiber drawing breaking the longitudinal symmetry in the resulting fiber. (b) Photographs of fibers with different pitches of tin wires created by rotating the preform holder at different rates.

Having developed resistors, inductors, capacitors, and diodes, the single remaining major circuit element is the transistor, which forms the basis of all modern electronics. The ability to incorporate transistors into multimaterial fibers and connect them together to create logic elements would be a boon to the development of fiber-integrated circuits and "computers". In fact, transistors were built into the fibers after initial development of the post-drawing annealing

process which reduced the semiconductor defect density to a level that an observable accumulation of charges and increase in conductivity could be observed when an electric field was applied through a gate structure. Figure 6.5 shows the initial field-effect transistor (FET) design and the field-induced change in conductance that can created after annealing. While this initial work is very exciting, the large spatial dimensions of the structure results in very large turn-on voltages (300 V) and non-ideal behaviors.

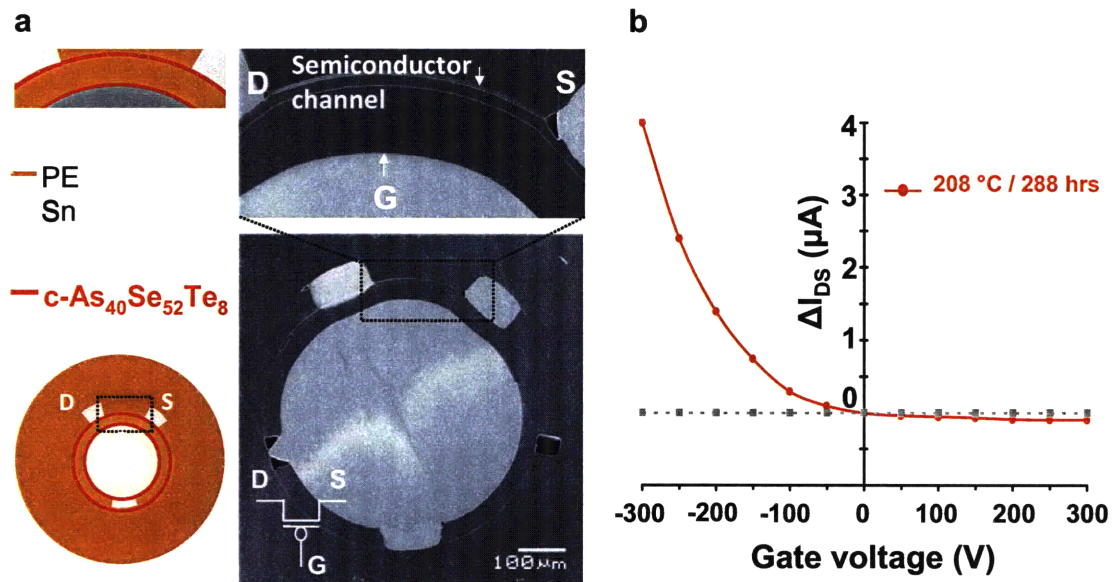

Fig. 6.5. (a) Schematic design and SEM of FET fiber transistor. (b) Change in drain-source current with 300 volts applied to gate compared to zero volts for both the as-drawn fiber (gray) and the annealed fiber (red). The annealing increases order and crystallinity in the fiber, reducing the density of defects and enabling carrier accumulation to occur (figure courtesy S. Danto and F. Sorin).

The performance of the FET fiber is expected to be substantially improved by decreasing the device dimensions through some of the fabrication techniques developed in this thesis as well as using semiconductors that can be crystallized for shorter times. An example of new structures and their electronic properties is given in figure 6.6. In this structure, a field effect is observed

when just 20 volts are applied to the gate. Further refinements in the device structure are ongoing.

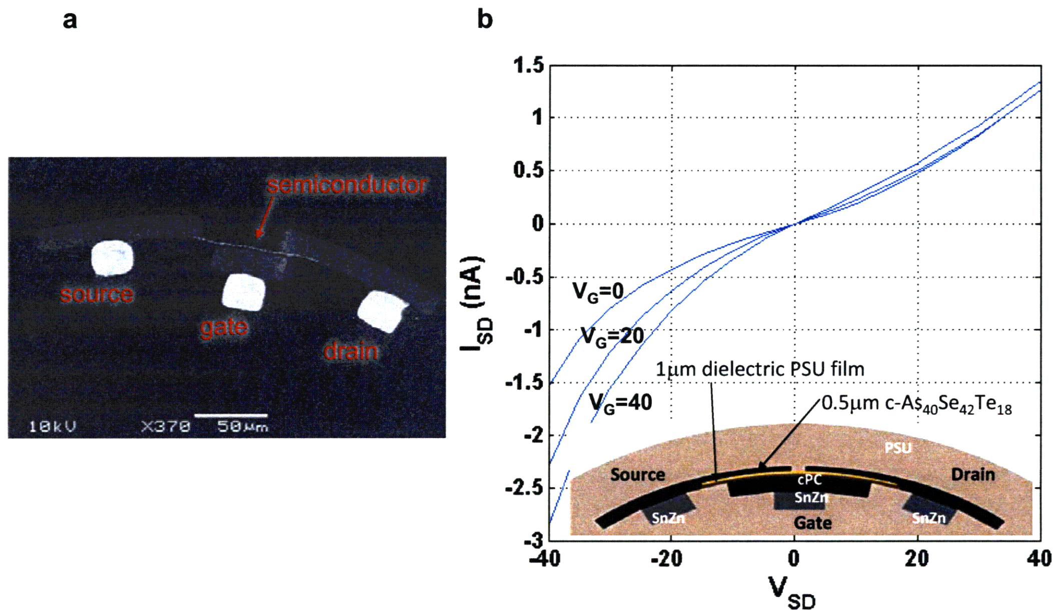

Fig. 6.6. (a) SEM micrograph of thin FET structure. (b) Change in drain-source current with applied gate voltage. Carrier accumulation and the concomitant increase in conductivity is observed for gate biases as low as 20 V. (inset) Schematic diagram of new FET structure utilizing fabrication techniques developed in this thesis (figure courtesy O. Shapira).

6.4 Conclusions

During the course of this thesis the first fiber-integrated rectifying junctions and diodes have been fabricated. This achievement required substantial effort in materials selection and characterization beyond the original thermal compatibility considerations of previous device fibers. For example, in addition to using the metallic electrodes for current extraction, their electronic properties such as work function must be considered. The work function of several alloys compatible with the multimaterial fiber drawing process was measured by two methods and found to vary over 600 meV. New methods of incorporating crystalline semiconductors were developed by creating a post-drawing annealing process that enables one to harness both

the ideal thermal properties of the amorphous state and the enhanced electronic properties of the equilibrium crystalline state. A set of metals and semiconductors were identified that exhibited both rectifying and ohmic properties when connected in a fiber geometry. New techniques in fiber fabrication were developed that led to a decrease in device dimensions by an order of magnitude from early fiber device designs enabling the fabrication of fiber diodes exhibiting clear rectification and a photovoltaic effect. The fiber diode's electronic properties were characterized by a series of electrical and photodectector measurements. EDS and KPFM were utilized to determine that a reaction between the $Se_{97}S_3$ semiconductor and $Sn_{85}Zn_{15}$ metal resulted in a ZnSe interfacial barrier whose large bandgap and large ionization potential forms a barrier to hole injection from the semiconductor to the metal resulting in the rectifying behavior. Future work is suggested that may lead to improved performance of this new diode as well as ideas on how to incorporate new materials and new device structures into multimaterial fibers to further the vision of intelligent fibers and fabrics for large area signal processing and detection.

6.5 References

1. Hanna, G., Jasenek, A., Rau, U. & Schock, H. W. Influence of the Ga-content on the bulk defect densities of $Cu(In,Ga)Se_2$. *Thin Solid Films* **387**, 71-73 (2001).

2. Michelson, C. E., Gelatos, A. V. & Cohen, J. D. Drive-level capacitance profiling: Its application to determining gap state densities in hydrogenated amorphous silicon films. *Applied Physics Letters* **47**, 412-414 (1985).

3. Kitagawa, H., Kimerling, L. C. & Tanaka, S. Iron-related levels in normal-type silicon studied by hall-effect and DLTS measurements. *Journal of Electronic Materials* **21**, 863-865 (1992).

4. Lide, D. R. *CRC Handbook of Chemistry and Physics*. Vol. 89 (CRC Press, 2008).

5. Daudi, A. R. & Subramanian, K. N. Strength and fracture of amorphous and partially crystallized selenium. *Journal of Materials Science* **18**, 2393-2400 (1983).

[6] Cabral, C., Chen, K. N., Krusin-Elbaum, L. & Deline, V. Irreversible modification of $Ge_2Sb_2Te_5$ phase change material by nanometer-thin Ti adhesion layers in a device-compatible stack. *Applied Physics Letters* **90**, 051908 (2007).

[7] Krusin-Elbaum, L. *et al.* Evidence for segregation of Te in $Ge_2Sb_2Te_5$ films: Effect on the "phase-change" stress. *Applied Physics Letters* **90**, 141902 (2007).

[8] Park, Y. S. *et al.* Stress Reduction of Ge2Sb2Te5 by Inhibiting Oxygen Diffusion. *Materials Transactions* **49**, 2107-2111 (2008).

[9] Zhang, S.-L. & Ostling, M. Metal Silicides in CMOS Technology: Past, Present, and Future Trends. *Critical Reviews in Solid State and Materials Sciences* **28**, 1-129 (2003).

[10] Qian, Q. D. *et al.* Low interface state density at an epitaxial ZnSe GaAs interface. *Applied Physics Letters* **54**, 1359-1361 (1989).

[11] Chiang, T. C. & Himpsel, F. J. in *Electronic Structure of Solids: Photoemission Spectra and Related Data* Vol. 23a *Landolt-Bornstein Group III* eds A Goldmann & E.E Koch) Ch. 2.1, 81-84 (Springer Verlang, 2006).

[12] Lang, O., Klein, A., Pettenkofer, C., Jaegermann, W. & Chevy, A. Band lineup of lattice mismatched InSe/GaSe quantum well structures prepared by van der Waals epitaxy: Absence of interfacial dipoles. *Journal of Applied Physics* **80**, 3817-3821 (1996).

[13] Grossiord, N. *et al.* On the influence of the processing conditions on the performance of electrically conductive carbon nanotube/polymer nanocomposites. *Polymer* **49**, 2866-2872 (2008).

[14] Kim, D. O. *et al.* Transparent flexible conductor of poly(methyl methacrylate) containing highly-dispersed multiwalled carbon nanotube. *Organic Electronics* **9**, 1-13 (2008).

[15] Sung, Y. T. *et al.* Rheological and electrical properties of polycarbonate/multi-walled carbon nanotube composites. *Polymer* **47**, 4434-4439 (2006).